University of New Hampshire
University of New Hampshire Scholars' Repository

Doctoral Dissertations | Student Scholarship

Winter 1969

THE ENERGY SPECTRUM AND FLUX OF FAST NEUTRONS IN THE ATMOSPHERE

RICHARD NORBERT ST. ONGE

Follow this and additional works at: https://scholars.unh.edu/dissertation

Recommended Citation
ST. ONGE, RICHARD NORBERT, "THE ENERGY SPECTRUM AND FLUX OF FAST NEUTRONS IN THE ATMOSPHERE" (1969). *Doctoral Dissertations*. 895.
https://scholars.unh.edu/dissertation/895

This Dissertation is brought to you for free and open access by the Student Scholarship at University of New Hampshire Scholars' Repository. It has been accepted for inclusion in Doctoral Dissertations by an authorized administrator of University of New Hampshire Scholars' Repository. For more information, please contact nicole.hentz@unh.edu.

This dissertation has been
microfilmed exactly as received

69-17,724

ST. ONGE, Richard Norbert, 1936-

THE ENERGY SPECTRUM AND FLUX OF FAST NEUTRONS IN THE ATMOSPHERE.

University of New Hampshire, Ph.D., 1969
Physics, radiation

University Microfilms, Inc., Ann Arbor, Michigan

THE ENERGY SPECTRUM AND FLUX OF FAST NEUTRONS IN THE ATMOSPHERE

by

RICHARD NORBERT ST. ONGE

B.S., Worcester Polytechnic Institute, 1963

M.S., University of New Hampshire 1965

A THESIS

Submitted to the University of New Hampshire
In Partial Fulfillment of
The Requirements for the Degree of
Doctor of Philosophy

Graduate School

Department of Physics
December, 1968

This thesis has been examined and approved.

Thesis director, John A. Lockwood

Roger L. Arnoldy

Harry H. Hall

Robert H. Lambert

George H. Mullen

Date January 7, 1962

PLEASE NOTE:

Not original copy. Blurred and faint type on several pages. Filmed as received.

UNIVERSITY MICROFILMS.

ACKNOWLEDGEMENTS

I wish to express my deepest gratitude to Professor John A. Lockwood for providing both the inspiration and the active collaboration which made this research possible. I also wish to thank Professor Lockwood for his critical aid in the preparation of this manuscript.

I would like to acknowledge the understanding aid and encouragement given by my wife, Penny. The assistance of Messrs. L. Friling, D. Huntley, and D. Schow of the Physics Department with the electronics design and construction is greatly appreciated. I also wish to thank Mr. K. Pratt for many hours of data reduction.

The unselfish use of a commercial two-parameter pulse height analyzer at the Worcester Polytechnic Institute by Professor B. Wooten and another at the Cambridge NASA-Electronics Research Center by Dr. Victor Scherrer is most appreciated.

Many crucial discussions with various researchers at the Oak Ridge National Laboratory is gratefully acknowledged. In particular, I wish to thank Dr. W. Burrus and Dr. V. V. Verbinski of O.R.N.L.

Finally, I most sincerely appreciated the many years of time-consuming discussions and suggestions by the faculty of the Physics Department.

This research was supported by the National Aeronautics and Space Administration under Contract NASr-164.

TABLE OF CONTENTS

ABSTRACT

The energy spectrum of fast neutrons (3-20 Mev) in the atmosphere at Pfotzer maximum (~100 gm/cm^2) was measured with a balloon launched from Palestine, Texas (~42° geomagnetic latitude). The neutron-gamma ray detecting system was a 2" x 2" diameter cell of organic liquid (NE 213) coupled to a high-resolution two-parameter multiple-particle (e,p,α) pulse-shape discriminator (PSD) and a two-parameter (64 x 64) logarithmic pulse height analyzer. The n-γ detector was completely enclosed by an anticoincidence charged-particle shield. The PSD resolved Compton-electrons, recoil-protons, and secondary alpha particles.

We found the slope $\beta(E)$ of the differential neutron energy spectrum ($dN_n/dE = B(E)\ E^{-\beta(E)}$) to smoothly decrease (harden) with increasing energy ($\beta(E) \approx 4.1 \pm 0.5$ at 3 Mev to 1.2 ± 0.5 at 20 Mev). Since the neutron energy spectrum shows a continuous flattening with increasing energy, we believe that the theoretical extrapolations of the high-energy albedo-neutron leakage flux beyond the range of measurements is extremely unsound. Consequently, the fraction of high-energy neutrons decaying to produce protons in the magnetosphere may be larger than previously indicated by both theory and experiment.

CHAPTER I

INTRODUCTION

Singer (1958), Hess (1959), Freden and White (1959), Kellogg (1959), Shklovsky et al. (1959), and Vernov et al. (1959) independently suggested that the trapped radiation belts around the earth originated from the decay within the magnetosphere of neutrons produced by cosmic radiation interacting within the atmosphere. The high-energy knock-on neutrons, which are produced by cosmic-ray particles making grazing angle collisions with the outer extent of the atmosphere, can directly escape into space. Since the half-life of the neutron is about 10^3 sec, the leakage neutrons can decay ($n \rightarrow p + e + \bar{\nu}_e$) to produce charged particles in the vacuum within the geomagnetic field above the atmosphere. These decay-produced protons and electrons may be trapped by the geomagnetic field causing them to mirror between the magnetic poles. Such gyrating charged particles may account for a fraction of the higher energy charged particles trapped by the geomagnetic field, referred to as the Van Allen radiation belt. Thus, although the theory of cosmic-ray secondary neutron production to populate the belts is an a priori theory, it requires knowledge of the probabilities for neutron production by cosmic rays in the atmosphere, the subsequent diffusion of neutrons from the atmosphere, and the beta decay with subsequent capture of the resultant charged particles by the geo-

magnetic field.

Experimental evidence, as well as detailed calculations made about 1960, suggest that the high-energy fraction of the radiation may originate from this source. The detailed evaluation of the cosmic-ray neutron albedo as a source mechanism for the trapped radiation depends upon knowledge of the fast neutron source strength, the effectiveness of trapping of these beta-decayed, high-energy charged particles within the magnetosphere, and, finally, the atmospheric loss mechanisms for such particles.

In this thesis we have measured the fast neutron flux and energy spectrum in the atmosphere to improve the calculations of the source strength for this mechanism of populating the radiation belts. By way of introduction, we will briefly survey some theories proposed to account for the radiation belts which surround the earth; and, specifically, to evaluate the cosmic-ray neutron albedo mechanism as a source. The experiment, recently carried on a balloon flight to about 5 gm cm^{-2} altitude will be discussed in detail. The energy spectrum and fast neutron flux value obtained from these flights will be compared with other measurements and with the theoretical calculations of Lingenfelter (1963), Dragt, Austin and White (1966), and Hess and Killeen (1966) to determine whether this is an adequate source mechanism for the energetic trapped protons.

CHAPTER II

SOURCE MECHANISMS FOR THE RADIATION BELTS

1. Introduction

The radiation belts enveloping the earth discovered by Van Allen (1958) and Vernov (1958) independently have certain remarkable characteristics. Firstly, the inner energetic particle belt is characterized by very little change with time and is almost entirely composed of energetic protons and electrons (Hess, 1965). Figure 1 gives some indication of the fluxes, energy spectra, and location of the charged particles within the belt (Naugle and Kniffen, 1961; Hess, 1968). Secondly, the ratio of alpha particles to protons within the inner regions is considerably less than that within the solar plasma or in cosmic rays. This is a difficulty for source mechanisms depending upon the acceleration of particles from the solar plasma in the magnetosphere (Fenton, 1967; Krimigis and Van Allen, 1967).

In considering the origin of the trapped radiation, we may ask if it can be of solar origin. If so, then how do the particles get in the "forbidden" regions of the geomagnetic field? By what mechanisms can these particles be accelerated near and inside the magnetosphere? What is the relative importance of these mechanisms to the cosmic-ray neutron albedo source? In further discussions of the source mechanisms we

will arbitrarily divide them into two classes: the electromagnetic source mechanisms and nuclear mechanisms.

2. Electromagnetic Source Mechanisms

The electromagnetic source mechanisms involve the acceleration and scattering of low-energy particles already within the magnetosphere. In order for an irreversible acceleration of trapped particles to occur, it is necessary that one or more of the three adiabatic invariants of the motion be violated.

If the magnetic field can be uniformly increased at a slow rate sufficient to conserve the magnetic moment, then a trapped particle can receive a net energy gain through the betatron effect (Northrop, 1963). A possible method of producing the effective change in the magnetic field can be the convective motion of particles from the boundary of the magnetosphere into regions of higher field strength (Axford and Hines, 1961; Kaufmann, 1963). Other electromagnetic source mechanisms include the Fermi acceleration process in which a charged particle in motion collides with a moving magnetic mirror point (Fermi, 1949).

Hydromagnetic waves may play an important role in the acceleration and scattering of particles. The existence of such hydromagnetic waves propagating in the geomagnetic field was predicted a number of years ago and has been recently confirmed experimentally. They are, apparently, generated at the boundary of the magnetosphere (Patel, 1964).

Another electromagnetic source mechanism is the injection of energetic particles from the interplanetary plasma directly into the magnetosphere either by diffusion across the boundary or by the intrusion of the plasma into the magnetosphere. In general, all these mechanisms are difficult to evaluate quantitatively, but most certainly they play a role in the populating of the radiation belts.

3. Nuclear Source Mechanisms

In the early studies of the Van Allen radiation belts, it was proposed by Singer (1958), Hess (1959), Freden and White (1959), Kellogg (1959), Shklovsky et al. (1959), and Vernov et al. (1959) that the neutron leakage or albedo was an important source function. Protons would be injected into the trapped regions by neutron decay. Of course, the simplest source would be to trap protons directly out of the cosmic-ray flux, but as Hess (1965) has clearly indicated, all calculated fluxes are too small by a factor of at least 10^4.

Solar neutrons which beta decayed within the magnetosphere would also contribute to the trapped particles, but all estimates of this resultant proton source are likewise far too low because the solar neutron flux is so small.

Singer (1958) showed that the albedo neutron leakage injection mechanism would give intensities which were in reasonable agreement with the observations. Assuming that only the atmospheric density determines the lifetime of trapping, he calculated the expected intensity distribution with

respect to altitude and the energy spectrum of the trapped high-energy protons resulting from the decay of the high-energy neutrons (Singer, 1959). Independently, Vernov et al. (1959) suggested the same source and pointed out that magnetic scattering would provide a limit on the lifetime at high altitudes. Recent theoretical calculations and revaluation of this source by Lingenfelter (1963), Dragt, Austin and White (1966), and Hess and Killeen (1966) indicate that albedo neutron decay may play a significant role only at high neutron energies (E > 30 Mev). For lower energies, the contribution to the trapped proton flux from the albedo neutron flux is probably insignificant.

Although there are current indications that the low energy trapped radiation does not originate from cosmic-ray neutron leakage, no other mechanism of injection and/or acceleration which is amenable to complete quantitative calculation has been proposed. Thus, it is specifically upon this neutron "albedo" source that this study will concentrate. In the following section we will briefly summarize the discussion of Dragt, Austin and White (1966), and Hess and Killeen (1966) on such a mechanism.

4. Discussion

Independently, both groups have concluded solar protons and solar neutrons make an insignificant contribution to the protons trapped in the Van Allen belts. Also, they agree that for protons of energy less than 10 Mev the galactic cosmic-ray secondary neutron decay injection is inadequate to produce

the large proton flux observed, as shown in Figure 1. Of particular relevence to this thesis are their conclusions that for proton energies greater than 20 Mev the neutron decay model may be adequate, but with differing modifications. First, Dragt et al. (1966) conclude that the ratios of the albedo neutron fluxes to mean atmospheric denisties encountered by trapped protons are low by a factor of 50 or larger. On the other hand, Hess and Killeen (1966) conclude that the slight disagreement at low altitudes may be attributed to additional contributions from other unknown mechanisms. However, at high altitudes, the flux calculated is close enough to the measured flux to say that the trapped protons in the middle of the inner belt may well come from galactic cosmic-ray neutrons.

In conclusion, more experimental data are required to clarify the theoretical situation. As Dragt et al. (1966) pointed out the differential neutron energy spectrum flattens out or perhaps even goes through a minimum at about 15 Mev, and then rises again rapidly with decreasing energy. This suggestion will be fully considered later in this thesis because the present system can determine such changes in the spectrum shape. We believe that the theoretical problem has been adequately developed by numerous workers. On the other hand, the experimental techniques used to acquire the necessary data on the neutron flux, energy spectrum, and atmospheric density need extensive revision at this time. The reason is the difficult conflicting experimental constraints imposed upon such a system. In order to understand these ex-

perimental conflicts, the following sections will introduce the specific experimental and theoretical difficulties which have prompted experimenters to assault this problem with an ever greater array of detecting systems.

CHAPTER III

GENERAL CONCEPTS

1. Introduction

Since the secondary energetic particle radiation in the atmosphere is produced by cosmic rays, we will describe the general properties of this radiation. This high energy source produces many different secondary particles, including neutrons. The majority of the neutrons diffuse within the atmosphere, degenerate in energy, and are finally captured by N^{14} to produce C^{14}. This diffusion theory model is well established and accurate within the atmosphere. However, since the neutrons near the top of the atmosphere are exposed to no distinct boundary conditions, the diffusion approximation fails. Various theoretical approaches to overcome this have been carried out. Thus, the energy and angular distribution above the atmosphere can be theoretically calculated if the neutron spectrum within the atmosphere is measured. From this calculated "albedo" neutron spectrum above the atmosphere, one calculates the resultant charged-particle spectra from the beta decay of the neutrons into protons, electrons, and anti-neutrinos. In particular, the energy and angular distribution of the resultant protons can be calculated. With this calculated proton distribution and the surrounding geomagnetic field, one can further calculate the flux of protons that will be geomagnetically trapped.

Since some of these trapped particles will also be continually lost in later collisions with the atmosphere upon mirroring, a simple "leaky bucket model" is used to obtain the final equilibrium spectrum of trapped protons in the Van Allen radiation belt.

2. Primary Radiation

The primary cosmic-ray fluxes of the galactic, and possibly intergalactic, cosmic rays are approximately 0.20 protons $(cm^2\text{-ster-sec})^{-1}$ and 0.03 He nuclei $(cm^2\text{-ster-sec})^{-1}$ with a very small component (~0.003) $(cm^2\text{-ster-sec})^{-1}$ of nuclei with $Z > 2$, roughly following the universal abundance of atoms. Thus, the proton/alpha particle ratio is ~7. Although free neutrons are found in equilibrium in the atmosphere, they cannot be present in any significant number in the primary cosmic-ray flux because of their relatively short half-life. There is also an extremely small component of electrons and X-rays. The energy per nucleon ranges between 10^8 ev and 10^{20} ev and exhibits a smooth differential energy spectrum.

Another important characteristic of this cosmic-ray flux is its history. The flux, as determined by studies of deep sea cores, has varied no more than 20% over the last 30,000 years. This long-term average appears to be relatively constant, but transient cosmic-ray time variations have been detected. These transient variations are placed into two broad categories after applying local meteorological corrections to the records: (a) variations of solar origin (solar flares, Forbush decreases associated with magnetic storms,

solar daily variations and 11-year variation), and (b) variations of galactic origin (possible sidereal diurnal variation of the high energy component).

We must bear in mind that, aside from an extremely small solar neutron flux, all neutrons are secondaries produced locally by the primary cosmic-ray collisions within the atmosphere. Although these primary energies are very great, the earth's magnetic field can be used as a momentum analyzer to select a portion of the spectrum. A threshold rigidity can be defined for cosmic rays at a particular zenith and azimuth angle so that particles would be excluded below this rigidity. For a simple dipole field, which is a first-order representation for the geomagnetic field, the variation of the vertical cutoff rigidity (P_c) is given by:

$$P_c = 14.9 \text{ (Gv)} \ \text{Cos}^4(\lambda)$$

where rigidity P(Gv) = 300 B (gauss-cm). Thus, the earth acts as a magnetic rigidity analyzer for the primary cosmic rays in the momentum range 1-15 Gv.

3. Secondary Radiation

These primary particles collide with the nuclei of the atmosphere to produce all the known fundamental particles. Although the details of the resulting cascade of secondaries are complicated, the general development of the cascade can readily be viewed in three ways: (1) component particles, (2) atmospheric depth, and (3) time.

a. Component Particles. The first mode of observation of component particles can be segregated into three types: nucleonic, mesonic, and electromagnetic, since there is little energy transfer among these components. The neutrons are produced predominantly by the nucleonic component since the cross sections for (e,n), (γ,n), and (μ,n) reactions are small while the (p,n) and (n,n) reactions have much higher cross sections. Since the muon interaction is slight, muons lose energy predominantly by ionization until they decay or bury themselves into the earth. The electrons and photons are mostly products of the cascade initiated by gamma rays from π^o decays and by electrons from the μ decays.

b. Atmospheric Depth. The components can also be seen with depth in the atmosphere by showing how the relative absorption lengths differ for the three components. The relative intensities within these three components rapidly change as the cascade propagates deeper into the atmosphere. That is, at the top of the atmosphere the cosmic rays will predominate, but as these primaries collide with the first 100 gm cm^{-2} of upper atmosphere, the flux of secondaries rapidly increase by several orders of magnitude. Deeper into the atmosphere at the Pfotzer maximum (approximately 100 gm cm^{-2}), photon and electron fluxes greatly exceed all other particles. These photons and electrons are the products of the cascade shower initiated by high-energy gamma rays resulting from the fast decay of π^o's and by relativistic electrons resulting from μ decays. The photon-electron

ratio is approximately two at 200 gm cm^{-2} and decreases to about one at sea level. The slight nuclear cross section, along with the higher mass of the μ allowing less radiation loss relative to electrons and the relativistic time dilation, allow the μ to penetrate deeper into the atmosphere. Thus, μ mesons become relatively more and more abundant deeper in the atmosphere, and at sea level they account for more than half of the secondary charged particles. π^{o} and $\pi^{\pm}$ meson fluxes are very low everywhere in the atmosphere because of their very short half-lives ($\sim 10^{-15}$, $\sim 10^{-8}$ sec).

On the other hand, the protons are lost faster because of the final rapid energy loss by ionization. Neutrons are rapidly reduced in energy by N and O collisions, whereby more slow neutrons are created which will finally lead to C^{14} production because of high neutron absorption cross sections which exist. Thus, neutrons are the least abundant species relative to γ's, e's, μ's, and p's at any depth below 50 gm cm^{-2}. The estimated component fluxes are shown at all depths in Figure 2.

c. Time Development. This cascade can also be viewed in time. If a high-energy proton collides with a nucleus of either nitrogen or oxygen at the top of the atmosphere, a complex reaction occurs. If the target nucleus is treated as a degenerate Fermi gas of neutrons and protons, in approximately 10^{-23} sec (~time for a pion to traverse nuclei at velocity c) some of the peripheral nucleons and pions are directly emitted in the direction of the incident particle. The

large majority of collisions are peripheral and, therefore, the incident nucleon retains a large fraction (~0.55) of its kinetic energy. The bulk of the recoil nucleons are ejected with energies less than 500 Mev regardless of increasing incident particle energy above ~5 Gev. π^o mesons emitted from the original interaction are decaying at a rate, $\tau_{\frac{1}{2}} \sim 10^{-16}$ sec. The energy imparted to some peripheral nucleons is then distributed to the whole nucleus. This excess excitation energy is finally released by proton, neutron, and alpha cluster emission over a period of 10^{-15} sec. These are emitted isotropically in the c.m. system, which is essentially the lab system also. Evaporation theory also predicts the emitted nucleonic energy distribution to be:

$$N_{(E)}\, dE = KE\, \sigma(E)\, \exp(-E/\theta)\, dE$$

where $\theta \approx 2$ Mev is the nuclear temperature after particle emission, N(E) is the number of nucleons produced per second from (E) to (E + dE). Such a distribution is Maxwellian. The neutrons and protons emitted in the evaporation stage will range from 1-10 Mev and are isotropic in both the center of mass and laboratory systems. $\pi^{\pm}$ mesons are now also decaying at about 10^{-8} sec to generate muons and neutrinos.

The cascade also develops by secondary interactions. Initial high energy nucleons continue to produce more nucleons and pions by interacting with another nucleus every 70-80 gm cm^{-2} of atmosphere traversed. Pion production ceases when the incident particle energy is reduced to less than 350 Mev, the pion threshold. For example, a 10^{11} ev primary will directly

interact, on the average, nine times, each of these interactions producing both direct knock-on and evaporation particles to form the cascade.

Most muons will survive their decay mode long enough to reach the bottom of the atmosphere. These very penetrating particles were originally called the "hard" component of the cascade. The π^{o} will quickly (10^{-16} sec) decay to produce two gamma rays, which in turn are converted into electron-positron pairs, developing an electromagnetic cascade. The high energy electrons produce X-rays by bremsstrahlung, also contributing to the electromagnetic cascade. Deeper in the atmosphere, and therefore, at lower energies, the gamma rays will produce Compton electrons.

Thus, from experimental measurements, the three components of nucleons, muons, and electrons will reach a maximum intensity at 100 gm cm^{-2} and from there decrease exponentially with increasing depth of the atmosphere, but with different absorption lengths for the components.

On the other hand, the exact theoretical method to treat the entire atmospheric cascade, which was physically described above and which is simple in concept, has only been solved for special cases. It never has been solved in a closed, general form (Olbert et al., 1957).

From this discussion we see that the neutrons produced by the cosmic-ray flux are of two types: direct knock-on and evaporation neutrons. The energy range of knock-ons is 10-100 Mev while the more intense (Gol'damskic, 1958) evaporation neutrons range from 1-10 Mev. Since the knock-on neutrons fol-

low the direction of the incident primary, the angular distribution of these secondary, high energy neutrons should have an angular distribution over the entire lower hemisphere, being predominately downward. Conversely, the more intense, lower energy evaporation neutrons are emitted isotropically everywhere throughout the atmosphere.

Now, let us consider the transport of these secondary neutrons within the atmosphere.

4. Transport of Cosmic-Ray Secondary Neutrons in the Atmosphere

The theoretical problems involved in calculating the flux, spectrum and angular distribution of secondary neutrons leaking out of the atmosphere are as difficult as the experimental problems in measuring them. These difficulties arise for three reasons. First, there are two different sources of secondary neutron production within the atmosphere: evaporation neutrons (1-10 Mev) and knock-on neutrons (10-100 Mev). The energy spectra of these two sources are quite different. Second, the secondary neutrons in the atmosphere are scattered by two different, energy-dependent modes: elastic scattering (E_n < 10 Mev) and inelastic scattering (E_n > 10 Mev). Third, the transport of neutrons differs with depth inside the atmosphere. For depths greater than 100 gm cm^{-2}, the diffusion approximation used in the Boltzmann equation is valid. Near the top of the atmosphere, at depths less than 100 gm cm^{-2}, the diffusion approximation is not valid. This imposes theoretical difficulties.

Although the Boltzmann transport equation is a valid theoretical approach, it is usually untractable because there is a large number of independent parameters, such as energy, time, position, and directional cosines. Hence, some simplifying assumptions must be made. The simplest approach is to neglect the time and angular dependence, thereby reducing the Boltzmann equation to the simpler scalar diffusion equation. Now, although the equation is solvable, the results will, of course, only be valid under the initial diffusion approximation. This is a low energy ($E < 10$ Mev) approximation and is not applicable within the first few mean free paths from the atmospheric boundary. The first attempt to solve this problem for atmospheric neutrons was made by Bethe et al. (1940). The calculation was correct within its assumptions and served to initiate the experimental measurements and the more refined theoretical calculations made in the next twenty years.

The next significant advances were really only improvements to the diffusion calculations which could be made by using computer techniques. More exact experimental measurements of the source spectrum within the atmosphere helped to better define the source function. Hess et al. (1960) pioneered in both the experimental and theoretical work. Later the calculations of Hess et al. (1961) were refined by Lingenfelter (1963a) using more accurate neutron source spectra within the atmosphere. Lingenfelter (1963b) also included the solar-cycle variations in the cosmic-ray neutron

production rate and the latitude dependence of the source function. But again, since the intrinsic diffusion approximation was used, the results are inaccurate near the most important region of the atmosphere, $x < 100$ gm cm^{-2}, and are also limited to the less important energy region, $E_n < 10$ Mev. Newkirk (1963) tried a different theoretical approach: the S_n numerical solution to the transport equation. The S_n method, as developed by Carlson and Bell (1958), is based on difference equation techniques which can be solved for this type of problem only on large computers. Newkirk's S_4 approach used an angular source distribution derived from the nitrogen cloud chamber experiments of Miyake et al. (1957). Although the diffusion approximation was not used in this S_n method, Newkirk did not extend the calculations to above the "top" of the atmosphere so that the neutron leakage could be determined. The neutron energy was limited to $E_n < 20$ Mev. There is, however, some evidence (Haymes, 1964) that it is the most accurate calculation available throughout the entire atmosphere (see Figure 3).

Actually, theory and experiment have "boot-strapped" each other in solving this problem of the source for the particles in the belts. Hence, the current theoretical status is now limited by a lack of reliable, high-energy experimental measurements within the atmosphere. In particular, the experimental values for $E_n > 10$ Mev are not reliable and no conclusive directional measurements within and above the atmosphere have been made. More high energy data are also

needed for neutron cross-sections for nitrogen, oxygen, and carbon as inputs to the theoretical calculations. And the calculations must be extended to E_n > 100 Mev, both within and above the atmosphere.

The computations to calculate the flux and spectrum of the geomagnetically trapped protons resulting from the decay of this neutron spectrum are much more straight forward and reliable (Hess, 1959; Dragt et al., 1966; Hess et al., 1966). The main difficulty arrises from a lack of accurate knowledge of the atmospheric mass density ($\rho(x)$) as a function of altitude at high altitudes (Dragt et al., 1966).

5. "Leaky Bucket" Model

Let us now review current efforts to derive the steady-state radiation belt assuming that a proton source distribution has been calculated from the extrapolated neutron spectrum. In order to build up a steady-state radiation belt, we must have loss processes or sinks in addition to particle sources. There are three loss mechanisms for inner trapped protons: inelastic nuclear collisions (E_p > 300 Mev), scattering from oxygen upon mirroring (E_p < 100 Mev), and charge exchange with hydrogen (E_p < 100 kev). Thus, the spectrum of the inner belt protons produced by neutron β-decay can now be calculated from the conservation of particles, using the continuity equation in energy space (Singer, 1958; Hess, 1962). We can write

$$dN(\varepsilon)/dt = \partial N(\varepsilon)/\partial t + \partial(N(\varepsilon)\, d\varepsilon/dt)/\partial \varepsilon$$

$$= (S(\varepsilon) - L(\varepsilon) + \partial(N(\varepsilon)\, d\varepsilon/dt)/\partial \varepsilon$$

$$dN(E)/dt = 0$$

where N(E) = equilibrium proton density energy spectrum, S(E) = source spectrum for protons, and L(E) = loss term for protons by all mechanisms. For equilibrium, dN(E)/dt = 0. This equation can be solved for N(E) to give the proton flux. The proton flux $\phi(E)$ is related to N(E) by

$$\phi(E) = v\ N(E).$$

This use of the continuity equation has been referred to as the "leaky bucket" model because the input rate must equal the output (or leak) rate for equilibrium. Van Allen et al. (1959) have suggested that this "leaky bucket" model may be carried one step further to calculate the average lifetime of a particle in the belts, τ_p. Since the input rate equals the output rate, which equals the contents divided by τ_p (where the contents of the belt can be obtained both experimentally and theoretically), τ_p can be determined.

Using this simple model Hess (1962) derived the final trapped proton spectrum by assuming a neutron leakage and compared this to a measured proton spectrum. There is no arbitrary normalization involved and there are no adjustable parameters in the theory. Thus, the final comparison of experiment and theory is direct (Freden and White, 1962) as shown in Figure 4.

CHAPTER IV

THE DIFFICULTIES OF FAST NEUTRON DETECTION

1. Neutron Detection - General Methods

A major portion of the problem of making a definitive experimental measurement to determine the secondary neutron decay population rests strongly upon the problems of detecting a small flux of fast neutrons. Therefore, we review briefly the methods of fast-neutron detection.

The direct interaction of a neutron with matter can only occur by virtue of its two main physical parameters: either wavelength (momentum) or magnetic dipole moment.

The wavelength can only be efficiently used with oriented matter having a comparable lattice spacing. Thus, neutron diffraction is limited to energies of less than 1 ev and is, therefore, of no interest in fast-neutron detection.

The weak magnetic moment of the neutron ($\vec{M}$) can be used to generate Cerenkov radiation, although normally one considers this only for charged particles. It can be applied to neutron detection by considering $\vec{J} = \vec{\nabla} \times \vec{M}$ as the current density. The expression for Cerenkov radiation is $\cos \theta = (\beta n)^{-1}$, where θ = angle between $\vec{\beta}$ and the direction of radiation, βc = velocity of neutron, and n = refractive index of medium. Therefore, the minimum velocity is $(cn)^{+1}$. The minimum kinetic energy is $1/2\ m\ c^2\ n^2 \approx 325$ Mev. Although this

is outside the fast-neutron range, it is useful to note this method has the unique characteristic of an efficiency increasing with energy. Yet, the direct interaction of fast neutrons with matter has not been used for detectors.

Let us next consider the multitude of indirect methods, all of which depend upon nuclear interactions. In order to organize this vast array let us further classify them into two types: inelastic and elastic collisions.

Inelastic collisions may further be subdivided into negative Q and positive Q reactions, where the final particle must be charged to permit direct detection. The negative Q type of inelastic reaction will usually occur when the value of Q lies within the range of the incident fast-neutron spectrum because of the Coulomb barrier for the emitted charged particle. Since this can at best serve only as a threshold detector and not effectively as a full range energy resolver, we will neglect this class of reaction.

The positive Q type of inelastic detections are more useful because they do not possess the threshold limitation. Again, we need only consider the (n, charged particle) reactions. Some inelastic, positive Q reactions are the following:

(1) Li^6 (n,α) T + 4.78 Mev

(2) He^3 (n,p) T + 0.76 Mev

(3) B^{10} (n,α) Li^7 + 0.48 Mev γ + 2.30 Mev

(4) n + S^{32} → P^{32} + p - 0.93 Mev
→ Si^{29} + ∝ + 1.16 Mev

(5) n + K^{39} → A^{39} + p
→ Cl^{36} + ∝ + 1.36 Mev

Li^6 sandwich detectors, because of the final particles being of approximately equal mass, are severely limited by their poor energy resolution. He^3 and B^{10} detectors are gaseous and therefore very limited in efficiency by their low relative density. If He^3 or B^{10} detectors are moderated, they cannot extract the spectrum. Hence, they can serve only as counters. The "Hornyak Button", a detector including both proton recoil detection and the sulphur reaction, is a semi-transulcent molded mixture of silver activated zinc-sulphide and plastic. This detector is hampered by a non-smooth, very low efficiency function (< 0.2%). The potassium reaction, as used in the KI (Tl) scintillator, is limited by a low pulse height response resulting in poor energy resolution. Thus, all of these reaction-based detectors are inefficient for a fast neutron detecting system.

The disadvantages of the neutron induced inelastic collisions can be realized by considering the (v^{-1}) law (Evans, 1955) for cross sections and by comparing their cross sections to that of an elastic collision. For the elastic collision we will choose that reaction which will realize the greatest energy transfer from neutrons - the (n-p) elastic collision.

From Figure 5, two important factors are evident that subject all inelastic neutron detectors to a tremendous disadvantage with respect to the elastic reaction (n-p). First, the neutron cross section in the energy range 1-10 Mev is roughly ten times greater for the (n-p) elastic collision

than it is for any inelastic reactions. Second, the slope of the reaction cross section changes markedly over the neutron energy range 1-10^6 ev. The (v^{-1}) law for the reaction cross section will change the neutron efficiency by three orders of magnitude between thermal and fast-neutron energies. This sensitivity to thermal neutrons in the unmoderated, reaction detectors is troublesome when measuring fast neutrons in the presence of an appreciable background of lower energy neutrons. In contrast, the cross section of (n-p) is much more constant over the same energy range and larger at $E_n > 10^3$ ev.

There are other factors that must be considered which again favor the (n-p) detector. In any detecting system the determining factor is the macroscopic cross section ($n \sigma$) as a function of neutron energy, where n = number of effective nuclei per cubic centimeter. Hence, the density of compounds of the various nuclei that can be produced must be considered. One finds that Li^6, He^3, B^{10} atoms cannot technically be introduced into a scintillating medium to greater than a few percent of the host scintillating atoms, whereas H^1 atoms have been introduced into the organic scintillators to greater than 50%. Therefore, the (n-p) detector is better by at least a factor of 10 as far as the nuclei density is concerned. Then, this factor is to be multiplied by σ, which is also larger by a factor of 10 in the energy range > 10^3 ev. Thus ($n \sigma$) is larger by a factor of 100 for a hydrogenous organic detector.

So far in this comparison we have only considered scintillators. What about other techniques? Gaseous detection schemes are always less efficient because the density of nuclei is less than in solids by at least 100. Neutron detectors using reactions based on Li^6, He^3, B^{10}, and H^1 with detection of the associated charged particle by means of a semi-conductor have been developed. Since the semi-conductor detector is actually only effective within its depletion thickness ($< 10^{-3}$ cm), this method is inefficient unless the detector has a large area, which then becomes costly.

Thus, we realize that out of the myriad of possible detection schemes the (n-p) elastic collision stands out as being far superior on the basis of efficiency alone. In addition, the scintillating detection method for the associated charged particle is also efficient. In summary, the selection of a hydrogenous scintillator as a fast-neutron detector was based upon the following reasons. First, the (n-p) cross section is essential constant over the fast neutron energy range. Second, the (n-p) cross section is ten times greater than any other nuclear cross section in the fast neutron energy region. Third, the percent of H^1 nuclei which can be introduced is about ten times greater. Finally, the effective volume of the scintillating detector can be greater.

2. Neutron Detection - Specific Methods

Although the organic scintillator has a rather con-

stant efficiency, there are some difficulties. Intrinsically the organic scintillators have three specific difficulties, any one of which could make them ineffective for measurements of the cosmic-ray secondary neutrons: high charged-particle efficiency, high gamma-ray sensitivity, and a complex convolution process to extract the neutron spectrum. Each of these problems will be briefly discussed in light of the measurements to be discussed and the associated environment for the detector. More details are presented in the appendices.

The high charged-particle efficiency is an immediate problem for this application since the charged-particle flux in space is much higher than the neutron flux. This can be seen in Figure 2. Here the electron and proton fluxes are approximately a factor of 100 higher than the neutron flux within the atmosphere. This charged-particle sensitivity cannot be directly suppressed without eliminating the neutron efficiency.

An anticoincidence shield system which completely encloses the central neutron and gamma-ray detector is used to identify incident particles as either charged or neutral. Thus, the measured neutron spectrum should closely represent the true neutron flux in the atmosphere or in space. Extreme precaution must be taken to reject charged particles which produce neutrons or gamma rays in the sensor system. The contributions from locally produced neutrons or gamma rays can make appreciable contributions to the total counting rate.

Ordinarily, a large 4π shield is not used because many photomultipliers are required to detect a minimum ionizing particle interacting anywhere in the system. It is also difficult if the photomultipliers are within the 4π shield because the shield size becomes large enough to be count-rate limited. The large number of photomultipliers is required because flat-faced tubes are attached to the surface of the scintillating shield. Under such conditions there is a rapid loss in signal strength for events at large distances from the photomultiplier. This attenuation can be seen in Figure 6 where the photomultiplier signal is plotted as a function of the distance along the light path from the tube to the light source. If the phototube design is changed to place a photocathode in the direct light path rather than being so located that light must be diffuse-scattered into the tube, the loss in signal strength for distant events is reduced considerably. Consequently, we chose a hemispherically-faced photomultiplier which could be inserted directly into the light path as shown in Figure 7.

The 4π shield system can be considered as a large light pipe which emphasizes the importance of total internal reflection and adiabatic curvatures. The simplest practical system is two mating hemispheres with only one hemispherical photomultiplier inserted into each scintillating dome. These two sections are connected by a short cylindrical section. It is required that minimum ionizing charged particles that pass through any part of the shield be detected. Since, for minimum

ionizing events, the energy loss in traversing the shield is directly proportional to the shield thickness at the point of entry, we can make the thickness variable to compensate for light losses between the scintillation event and the photomultiplier. In this design the shield thickness is appropriately greater at larger distances from the phototubes. Hence, the particle generates a greater light signal at larger distances from the photomultipliers to properly compensate for the light attenuation. Since this would require a surface too complicated to be fabricated easily, a simple workable solution is to offset slightly the centers of curvature of the inside and outside surfaces of the hemisphere (Figure 7).

To use such a 4π shield system to the fullest advantage, the associated electronics should include parallel summing and coincidence circuits as shown in Figure 8. This unusual precaution eliminates the important case where a high-energy charged particle enters the system, interacts within, but does not exit.

Further, this totally enclosing charged particle shield has very fast time response ($< 10^{-8}$ sec). We can then use this shield in coincidence (as well as anticoincidence) with the inner detector. This will permit the separate measurement of both the neutral particle spectrum and the charged particle spectrum within certain prescribed energy limits. Therefore, this simple scintillating shield completely eliminates the charged-particle sensitivity and yet does not produce any detectable local secondary particles to disturb the

sensitive measurements. The detailed design for this shield (St. Onge and Lockwood, 1968) is shown in Appendix A.

The high gamma-ray sensitivity of the organic scintillators can be used advantageously if a pulse-shape discriminator (PSD) (St. Onge and Lockwood, 1967) is incorporated into the system which will separate neutrons from gamma-ray events. Since the gamma-ray count rate is much greater than the neutron count rate, the PSD must be very effective and reliable. If such discrimination is possible, the gamma-ray spectrum can also be extracted simultaneously. However, organic scintillators also contain carbon, and the C^{12} (n,α) Be^{9} (threshold 6.17 Mev) and C^{12} (n,n') 3α (threshold 7.98 Mev) reactions will produce secondary internal alpha particles (Graves and Davis, 1955; Howerton, 1958; Mössner, Schmidt, and Schintlmeister, 1966; Al-Kital and Peck, 1963; Chatterjee and Sen, 1964; Kopsch and Cierjacks, 1967; Huck and Walter, 1968). This must also be considered in deducing the neutron energy spectrum.

The PSD must be effective to separate alphas from recoil protons and Compton scattered electrons produced by gamma-ray interactions. The number of internally produced alphas can be as large as 10% of the number of recoil protons in the fast neutron energy range. For fast-neutron detectors the system must separate all three types of secondary particles. Since no such system was available, a multiparticle PSD system was designed (St. Onge and Lockwood, 1968).

The PSD developed has the following characteristics:

high multi-particle resolution (M~3)*, wide dynamic range ($1 < E_n < 30$ Mev), simplicity, passiveness, stability, high count rate capacity (> 50 kHz), minimum weight (< 20 grams) and low power consumption. This system simultaneously extracts the separate gamma-ray, neutron, and alpha-particle pulse-height spectra. There is some evidence that muons are also separated as shown in Figures 9 and 10. The detailed description of the PSD is presented in Appendix B.

A complex convolution process is necessary to obtain the incident neutron or gamma-ray particle spectrum. In general, a mono-energetic input flux does not produce a simple line-spectrum response from the detector. This occurs for many interdependent reasons. The most prominent reason is the basic elastic collision process of the incident neutron with a proton of the organic scintillator. It is equally probable for the neutron to transfer to the proton any energy from 0 to E_n. This is exact only if the differential scattering cross section is independent of the scattering angle (i.e., isotropic) in the center of mass frame. Such an approximation is good (< 2% error) for $E_n <$ 10 Mev and fair (< 10% error) for $10 < E_n < 30$ Mev (Fowler and Brolley, 1956; Hess, 1958; Marion and Fowler, 1960). Therefore, such pure elastic scattering produces a recoil proton spectrum that is a simple rectangular distribution.

* M is defined as the separation of the two peaks (e,p) divided by the sum of the full-widths at half maximum (St. Onge and Lockwood, 1968).

However, in any actual proton recoil pulse spectrum this simple rectangular response is distorted by several second-order effects: statistical fluctuations in the scintillation process and photomultiplier, deviations from isotropic n-p scattering cross section, multiple scattering by carbon and non-elastic processes in the scintillator, edge effects, nonlinearity of scintillator light output vs energy for heavy charged particles and directional asymmetry of scintillator output (Schwarz and Zefterström, 1966).

The problem of spectrum unfolding with this complex response has been treated in the literature in many ways. We believe that this can be logically organized in two ways. The first, an historical approach, is a simple theoretical unfolding assuming only single scattering and pure elastic collisions. The second, and more recent method, assumes that the actual physical processes are very complex and avoids the direct assault of this difficult problem. Instead, the detector system is "calibrated" with a range of monoenergetic neutron sources to obtain the response of the system. In retrospect, this separation of the development of the two methods of "unfolding" or understanding are familiar to many areas of physics. Initially, microscopic tools have been used to treat one or more aspects of a given problem; but as the inter-relationship of these aspects increased, the macroscopic view was found more fruitful. In particular, the description of the response of a given atomic or nuclear system to an external stimulus has proved to be both a practical

as well as theoretically elegant formulation. Both methods will be discussed in this thesis.

3. Microscopic Unfolding Methods

a. First Order Approximation. The first order relationship between the resultant experimental recoil proton spectrum and the incident neutron spectrum is straight forward. This is valid if the scintillator size is such that the probability of a second n-p scattering is small and that few recoil protons leave the scintillator. Since these assumptions depend upon both energy and scintillator size, the size must be carefully chosen for the particular neutron energy range. Assuming this criterion to be realistic, Staub (1938) has derived the recoil proton spectrum, which is the starting point for all microscopic unfolding methods.

$$dN_p/dE_p = \int_{E_p}^{\infty} n_H \sigma_H(E_n) V f(E_n, L) E_n^{-1} (dN_n/dE_n) dE_n$$

where E_n is the neutron energy and E_p is the proton energy. dN_p/dE_p is the number of recoil protons per unit proton energy interval per second and dN_n/dE_n is the number of neutrons per unit neutron energy interval per cm^2-second incident upon the scintillator. $f(E_n,L)$ is a factor to compen-

sate for the attenuation of the neutron flux in the scintillator, n_H is the number of hydrogen atoms per cm^3, and σ_H is the n-p scattering cross section. V_i is the volume of the scintillator, L is the thickness of the scintillator, and $\Sigma_T(E_n)$ is $n_H\sigma_H(E_n) + n_c\,\sigma_c(E_n)$.

Now solving for dN_n/dE_n by differentiating with respect to E_p, and recalling that

$$d/dx\,(dN/dx) = d/dx\left(\int_x^d F(y)\,dy\right) = -F(y)\Big|_{y=x},$$

we have

$$d^2N_p/dE_p^2 = -(n_H\sigma_H(E_p)\,V\,E_p^{-1})F(E_p,L)(dN_n/dE)$$

$$F(E_p,L) = [1-\exp(-\Sigma_T(E_p)L)]/[\Sigma_T(E_p)L].$$

Rearranging and solving for dN_n/dE_n,

$$dN_n(E_p)/dE = -[\Sigma_T(E_p)L]/[1-\exp(-\Sigma_T(E_p)L)](d^2N_p/dE_p^2)\cdot$$
$$\cdot(n_H\sigma_H(E_p)\,V\,E_p^{-1})^{-1}.$$

If we correct for the non-linear light function, $L(E_p)$,

$$dN_n/dE = -(E_p/n_H\sigma_H(E_p)V)(dL/dE)\cdot$$
$$\cdot[\Sigma_T(E_p)L]/[1-\exp(-\Sigma_T(E_p)L)][d/dL\,(dN_p/dL\cdot$$
$$\cdot\,dL/dE)].$$

b. Second Order Corrections. There are six important corrections (> 3%) to the first order unfolding model as outlined.

1. Statistical Fluctuations. The correction necessary because of the limited resolution of the detector to a delta function input is serious only in the case of a line spectrum. However, since the unfolding processes discussed here are assumed to be applied to a continuous distribution, this correction is unnecessary.

2. Deviations from Isotropic n-p Cross Sections. This approximation as indicated previously is less than 2% for E_n < 10 Mev, and less than 10% for 10 < E_n < 30 Mev. As a simple correction for this error, we will use the average center of mass cross-section at each energy interval to reduce the error to < 5%.

3. Scattering from Carbon Nuclei. The corrections due to neutron-carbon interactions depend upon the energy region. For neutron energies below the threshold energy of about 7 Mev the only effect is the elastic scattering of neutrons from carbon. The maximum energy transfer possible in this process is $\alpha\ 4A(A+1)^{-2} \simeq 28\%$. More importantly, the light output from such carbon nuclei recoils is extremely small. Therefore, we will neglect this correction. At high energies (E_n > 7 Mev) several charged-particle reactions become important. The most probable reactions are alpha particle emitters (i.e., $C^{12}(n,\alpha)Be^{9}$ and $C^{12}(n,n')3\alpha$). This effect can be large. In fact, in this experiment the alpha

contribution would require approximately a 10-20% correction. But since the PSD effectively separated these alpha particles from the protons, no correction is required. We feel this is a most important aspect of the multi-particle PSD system used in this experiment.

4. Second Scattering and Wall Effects. As a correction for second scattering and escape effects in cylindrical scintillators, Broek and Anderson (1960) derived the following correction factor:

$$F = 1 - 0.78\, R_p(max, E_n)\, L^{-1} + 0.090\, N_H\, L\, V^{-1}\, \sigma(E_n) +$$

$$+ 0.077\, N_H\, r\, V^{-1}\, \sigma(0.068 E_n)$$

where L is the scintillator thickness, r is the scintillator radius, $R_p(max,E_n)$ is the maximum range of a proton at E_n, and N_H is the number of hydrogen atoms in the scintillator. The second term is a correction for wall effects, and the last two terms are corrections for second scattering. Dividing the derived neutron spectrum by this correction factor eliminates most of the error from second scattering and wall effects. This correction is a minimum when the scintillator thickness is

$$L^2 = \frac{0.78\, R_p(max, E_n)\, N_H^{-1}}{0.09\, \sigma(E_n) + (0.077/2)\, \sigma(0.068 E_n)}$$

for the case where the diameter equals the thickness.

Since this second-order correction can only be zero for a given scintillator size at only one energy, we must cor-

rect neutron spectra extending over a wide energy range.

5. Nonlinearity of Scintillator Light Output. The correction for nonlinearity of light output is a serious correction for which an exact expression is available as shown in Figure 11 (Verbinski et al., 1968).

6. Directional Asymmetry of Scintillator Output. The correction necessary because of a non-isotropic scintillator, as in the case of stilbene, can be as much as 15%. In this experiment we chose a liquid scintillator to reduce this correction to a negligible amount. The directional asymmetry of a NE213 organic scintillator is less than 2%.

4. Macroscopic Unfolding Methods

A neutron spectrum dN_n/dE_n (neutrons/cm^2-sec-Mev) will induce a pulse height distribution of dN_L/dL (number of pulses/unit pulse height-sec). These two distributions are related as indicated in the previous section. That is,

$$dN_L/dL = \int_{E_n=L}^{E_n(max)} \epsilon(E_n) K(E_n, L) (dN_n/dE_n) dE_n$$

where $\epsilon(E_n)$ is the efficiency of detector at E_n, and $K(E_n,L)$ is the response kernal of the detector. The difference now is that the response function is not the simple function assumed previously in the unfolding techniques by microscopic methods with pure elastic collisions. Recall that in the microscopic method derived by Staub (1953) we had

taken $K(E_n) = E_n^{-1}$. This was, in reality, both the advantage and difficulty of the microscopic method. The asset was that the simple function (E_n^{-1}) is not also a function of E_p or L. This allowed a simple derivative to be obtained with respect to E_p.

Although this simple function provides a solution, it is limited by the assumption of pure elastic scattering. The (E_n^{-1}) form derived by Staub assumed a flat differential cross section in the center of mass system. This is not exactly true for $E_n \gtrsim 10$ Mev and is the reason for the many necessary corrections in the earlier simple, pure elastic mode. The macroscopic method avoids this difficulty and determines $K(E_n, L)$ by an accurate calibration procedure. First, let us return to the macroscopic formulation (Brunfelter, Kockum and Zetterström, 1966),

$$dN_L/dL = \int_{E_n=L}^{E_{n(max)}} \epsilon(E_n) K(E_n, L)(dN_n/dE_n)\, dE_n .$$

This can be transformed into the equivalent matrix formulation by incorporating the entire response or kernal into one matrix, (R):

$$(dN_L/dL) = (R)(dN_n/dE_n)$$

where

$$(dN_L/dL)_j = \int_{\Delta L_j} (dN_L/dL)\, dL$$

$$(dN/dE_n)_i = (dN_n/dE_n)(E_{n_i} - \Theta \Delta E_{n_i})$$
$$0 \leq \Theta \leq 1$$

$$R_{ji} = \int_{\Delta L_j} dL \int_{\Delta E_{n_i}} K(E_n, L)\, \epsilon(E_n)\, dE_n$$

To reemphasize the situation, we have a direct but vague formulation of the neutron distribution (dN_n/dE_n) producing a light pulse distribution (dN_L/dL),

$$(dN_L/dL) = (R)(dN_n/dE_n)$$

To obtain the neutron spectrum (dN_n/dE_n) from this matrix equation, many routes have been developed in the current literature. Most methods involve a computer-obtained inverse of the response, $(R)^{-1}$. This allows the direct extraction of (dN_n/dE_n):

$$(R)^{-1}(dN_L/dL) = (R)^{-1}(R)(dN_n/dE_n) = (dN_n/dE_n)$$

Although this appears simple, the real difficulty is the propagation of the statistical errors or noise which are present in every element of both (dN_L/dL) and (R). These normally small errors (< 5%) are vastly amplified in the matrix inversion and are really the crux of the problem in this method. For example, to emphasize the importance of the error amplification, Bock and Lanahan (1966) find that:

$$\bar{\epsilon}/\bar{s} = n^a/\sqrt{N}$$

where $\bar{\varepsilon}$ is the average error in elements of the unknown neutron spectrum and $\bar{s}$ is the average error in elements of the known pulse distribution. N is the total number of counts in the pulse distribution and n^o is the maximum number of resolvable energy lines. In the case of 64 energy channels used, from which we could allow $n^o \sim 30$ and assume $N = 10^3$, we obtain a 470% error from a 5% error in $(\bar{s})$. Thus, this inversion method can only be used where the special conditions allow the experimentalist to place very small errors on the elements of the matrices. Since the experimental results of this thesis have errors of the size shown in the above error analysis, we feel another route must be devised that avoids the matrix inversion.

A macroscopic method which avoids the error amplification introduced because of the matrix inversion will now be discussed. We will examine the problem of unfolding a matrix equation of the form: $L(\ell_i) = R(E_n, \ell_i)\ \Phi(E_n)$, where $L(\ell_i)$ is the resultant measured output light pulse spectrum, $R(E_n, \ell_i)$ is the measured detector response operator, and $\Phi(E_n)$ is the input neutron spectrum. The operator $R(E_n, \ell_i)$ can be related to the differential efficiency $\varepsilon(E_n)$ of the detector,

$$\sum_{\ell_i} R(E_n, \ell_i) = \epsilon(E_n).$$

We must, in general, assume that each element of both (L) and (R) have an associated error. Because of this error,

any involved analytical operations used to unfold the equation in solving for Φ will introduce an error amplification. In this regard, the error amplification introduced with the multiplication operation is greater than with the addition operation. Thus, we must always minimize the number of operations, especially the multiplication operations. We feel that for the albedo neutron spectrum this unfolding can be very simply carried out by an iterative method in which the first iteration is simply derived from the microscopic method discussed earlier or a physical argument of the spectral form. This macroscopic method can be used for any type of input spectrum which is a superposition of discrete and continuous spectra. Since in this application the macroscopic method has not disclosed any discrete spectra, we will limit further discussions to continuous spectra, although both could be handled with the same technique.

Haymes (1964), Mendell and Korff (1963), Holt, Mendell and Korff (1966), and Baird and Wilson (1965) have found the atmospheric neutron distribution to be of the form $\Phi(E_n) = AE^{-x}$. The measured range of x was ($1.05 \leq x \leq 1.42$). There is some indications that the spectrum $\Phi(E_n)$ may be the sum of two such terms.

$$\Phi(E_n) = \sum_i A_i E_n^{-x_i}$$

With the use of the measured response function R, we can directly compare the light pulse spectrum vector L without involving any unnecessary analytical manipulations

which would introduce error multiplications. This can be accomplished as follows:

$$-\varepsilon < (L - L_0)/L_0 = (R\vec{\Phi} - R\vec{\Phi}_0)/R\vec{\Phi}_0 < \varepsilon$$

where ε is the minimum fractional deviation and Φ_0 is a trial spectrum. Successive iterations with different Φ_0's will expose a best fit to the measured light pulse vector; thus producing the desired neutron spectrum from a bounded, best fit scheme.

CHAPTER V

THE EXPERIMENTAL SYSTEM

The experimental system necessary to measure the neutron energy spectrum in the atmosphere was developed from the two basic sub-systems previously discussed: the two-parameter pulse shape discriminator (PSD) and the anti-coincidence charged-particle shield. Many additional sub-systems were devised to compliment these without degrading each other. This was necessary because the separation of the different particles (electrons, protons, and alphas) by the PSD could be obliterated by any unstable intermediate electronic system. Therefore, the overall stability of the preamplifiers, amplifiers, linear gates, delays, pulse height analyzers (PHA), and high voltage supplies integrated in the system had to be better than 2% over the temperature, pressure, and voltage excursions anticipated in the balloon flight. The preflight thermal radiation calculations used to design and predict the behavior of the detector in flight are given in Appendix C.

Of prime consideration in the system was local secondary neutron production from the apparatus which could be detected by the neutron sensor. The effects of local production were reduced in two ways. First, the system was physically separated into two pieces; the nearly bare detector was located 2.75 m above all additional apparatus. Second,

the detector was surrounded with the minimum mass of material necessary to provide thermal insulation (0.7 gm cm^{-2} of urethane foam). As a result of these precautions, contamination from local neutron production was calculated to be much less than one percent. These production calculations are in Appendix D.

1. The Neutron Detector System

The neutron detector is comprised of two subsystems: the surrounding charged-particle shield and the inner n-γ detector. The shield design is calculated and discussed in the appendix. Nuclear Enterprises Ltd. fabricated the shield to our design specifications. Since the design was unconventional, we first had a prototype hemispherical section manufactured to test the material for warping and surface crazing. This prototype distorted approximately 1 to 2 mm from a true circle in a diameter of 30 cm. More importantly, regions of surface crazing were noted in the thinner sections. After consulting with Nuclear Enterprises Ltd., it was decided that the manufacturing (lathe-turning) sequence should be interrupted before the final dimensions were obtained. At this time the shield should be annealed to release the strains induced because a large mass of NE 102 was removed from the plastic casting. As a result of these precautions the full-size shield was found free of these undesirable effects.

The two photomultipliers (RCA-C70132A) were potted into shallow, accurately-contoured depressions in the shield

with Sylgard 184 silicone compound. To insure a bubble-free interface, the shield and photomultiplier were immediately inserted into a vacuum chamber. A ten-minute sequence of evacuations to 1 mm Hg pressure followed by exposure to atmospheric pressure removed all observable bubbles. Finally, a thick aluminum foil was loosely applied to all surfaces to improve the light collection.

The n-γ detector is a 4.60 cm x 4.65 cm diameter clear pyrex cell containing deoxygenated NE 213 organic liquid scintillator. A small expansion chamber was connected to one end of the cell by a thin capillary tube to allow for thermal expansion of the fluid. Although a small bubble in the chamber allowed for this expansion, it also presented other difficulties. The bubble had to be confined to the expansion chamber since it could seriously change the light collection efficiency if it should move into the main cell. In order to avoid the bubble migrating to the lower main cell a small capillary tube was used to connect both chambers. In addition, we had to eliminate any effects varying the light collection because of the expansion chamber content changing with temperature or position. However, since these undesirable scintillations which occur in the expansion reservoir are optically coupled to the photomultiplier through the glass walls of the capillary, we eliminated them by painting the reservoir with flat black absorbing paint. Since this eliminated the optical coupling of the reservoir scintillations, it also improved the energy resolution. The lower main cell was loosely

covered with aluminum foil for better light collection and improved resolution.

A small crystal (3 mm x 3 mm dia) of NaI (Tl + Am^{241}) was optically coupled to the top of the cell with a bubble-free film of clear silicone compound. The characteristic light pulse from the decay of the NaI (Tl) scintillator irradiated with alpha particles from the doped radioactive Am^{241} was pulse shape discriminated. This was used to form a simple, but accurate, in-flight calibration (IFC) which was easily resolved from all other impinging radiation. By manipulating both the exact location and the effective crystal size, the Am^{241} peak could be relegated to a vacant region of the two-parameter particle display as shown in Figure 12 (St. Onge and Lockwood, 1968).

Both the NE 213 cell and the IFC were viewed by one photomultiplier (RCA 8575, 5 cm diameter). The interface of the cell and photomultiplier (PM) was a thin film of bubble-free silicone compound. The fast PM-base circuitry followed the concepts of Gibson (1966). The PSD was mounted on a small 5 cm diameter printed circuit board located on the PM base. The PM cathode was operated at a negative high voltage for two reasons. First, the noise of the dc high-voltage supply would not be directly applied to the signal output on the anode. Second, the 50Ω, high-frequency output of the PM would not be degraded by the addition of a high-voltage connection. This allowed the PM anode to be properly matched for output impedence thereby resulting in a signal rise time

of approximately 2 x 10^{-9} sec. This high-fidelity, high-frequency capability was important in maximizing PSD particle resolution. Although this optimized the PSD operation, it also presented a difficulty. The entire outer part of the glass PM assemble was at a high voltage. Consequently, a grounded, thin aluminum can surrounded and isolated the n-γ detector. This can containing the PM was vacuum evacuated and then pressurized to two atmospheres with pure, dry SH_6 gas to insure a safe corona-free environment in flight.

In addition, this high-density gas proved to be a good thermal conductor to remove heat generated in the PM bleeder chain. Such an insulating gas system is better than silicone potting for high voltage protection. Previously, the large coefficient of thermal expansion of the silicone potting compounds combined with their very low thermal conductivity broke several PM tubes. This was caused by the force exerted between the delicate PM pins from the expansion of the potting compound. This, in turn, was caused by its low thermal conductivity and the heat generated in the enclosed bleeder chain. Such an insulating gas technique could be applied to both high voltage (dc-dc) converters and PM tubes for the charged particle shield. The elimination of the potting compound also reduces unnecessary masses of moderating material very close to the n-γ detector.

Since the detector was located 2.75 m above the rest of the equipment it was necessary to include voltage preamplifiers within the charged particle shield to drive the

voltage pulse down the associated long shielded coax cables to the main electronics system. A temperature monitor and voltage monitor were located within the charged-particle shield.

2. The Electronics System

Figure 13a shows the complete electronics system. The two parameter ($\int$Ldt x dL/dt) pulse height analyzer was developed from the one parameter system of Ewald and Sarkardy (1966). The only important change was to convert it to a logarithmic, two-parameter (64 x 64) analyzer. Logarithmic analysis was chosen because it was statistically desirable to have near equal counting probabilities in each neutron ($\int$Ldt) channel bin. It also maximized the PSD particle identification realized from the limited number of channel bins (4096) since the resolution falls off approximately as E^{-1}. Since the particle track trajectory was nearly a straight line on the log-log output plot, it allowed simple particle identification as shown in Figure 12. A large number of the analog and logic sub-systems required were obtained by modifying standard nuclear modulars (AEC-NIM). Although very bulky and power consuming, they provided adequate operation and avoided the time consuming engineering and testing. The electronics system contained both temperature and voltage sensors.

3. The Telemetry System

Although the transmitter was a conventional FM-FM type with 12 sub-carrier modulators, a special transmission

logic scheme was developed especially for the system. This was necessary because high data reliability had to be incorporated into the transmission coding and logic. Since the high energy neutron data rate is very low, normal atmospheric and man-made broad-band electrical noise rates can at times be much greater (i.e., lightening storms and arc welders). This noise could add extra bits to words being transmitted and generate "new words". Thus, some error-rejection methods were necessary to assure reliability of the data. This was accomplished with three interrelated error detecting and rejecting concepts: parity bits, redundant out-of-phase double transmission, and triple-delayed coincidence bits. A trigger bit preceded all valid transmission words. Since the information to be transmitted was composed of two words from the bipolar binary output of the logarithmic two-parameter pulse height analyzer (dL/dt, $\int$Ldt), each word of the pair contained 6 binary bits (64 x 64) as shown in Figure 13b. Two identical pulse trains were transmitted on different sub-carrier frequencies; one transmission was delayed in time by the width of one logic bit (200 μ sec). Therefore, during the vulnerable atmospheric flight time, the two logic transmissions were out of step with respect to corresponding bits. Consequently, a noise bit introduced during data transmission would not produce the same word in each transmission. After receiving the data the undelayed, prompt transmissions were also delayed by 200 μ sec in order to realign both transmissions. The data was then electronically checked for consistency in both transmissions

by a simple coincidence demand between corresponding bits. Each data word was also checked for parity as an extra precaution. Data not meeting all reliability demands was rejected.

This unconventional error detecting and rejecting scheme proved to be necessary, reliable, and very simple. In addition, six low-frequency subcarriers transmitted the following information: temperatures, voltages, scaled charged-particle counts, scaled n-γ counts, and scaled n, γ, p, e counts.

4. The Ground Station Decoding System

The ground system was completely designed and built at the University of New Hampshire by Friling and Schow (1968). This system was designed to check all transmitted data for the three redundant reliability tests: proper parity, consistent double transmission, and triple-delayed coincidence. Data which passed these tests were sent to either of two read-and-display systems: the modified core memory of a pulse height analyzer (Nuclear Data, 512) or an incremental tape recorder (Digi-Data Corp.). The single-parameter 512 channel PHA was modified so as to store and read two-parameter (64 x 64) data. Data recorded on the incremental tape recorder was transferred to an IBM 360 computer. Both systems proved to be consistent and reliable. As an example of the ground station operation, we show in Figure 12 the raw data from the balloon flight at the altitude of the Pfotzer maximum. This is displayed on an

IBM print-out sheet. Since the pulse height analyzer clock could really produce more than 64 channels for the larger pulses, this display shows the extension of both the neutron and gamma-ray tracks folded over onto the upper left side of the display. The $\int Ldt$ amplifier begins to saturate in channel 67. Therefore, the integral counts above this pulse height are recorded in these saturated higher channels. We believe that this unconventional method of folding a 128 channel (7 bit x 7 bit), two-parameter pulse height analyzer is a very useful technique. However, it is only unambiguous if the different particle tracks are parallel to each other and at an acute, constant angle to the ordinate. Consequently, the entire data tracks were "folded" into this much smaller region. This technique conveniently reduces the number of bits which are transmitted, decoded, and displayed while retaining the resolution of a system of four times the analyzing area.

5. Environmental System Behavior

The detector with all electronics systems was subjected to both vacuum and temperature tests. The entire system was exercised while subjected to temperature excursions from -20°C to +50°C and pressure excursions from 1010 mb to 2 mb. No significant operating variations were observed during these tests. Any variation was determined by three independent techniques. First, a precision pulser was used at the four preamplifier inputs. Second, the internal NaI (Tl, Am^{241})

IFC was used. Third, the Compton edge and peak of Na^{22} and Th^{228} were observed. All three tests showed a variation of less than 2% over the combined environmental excursions of vacuum within the temperature range of -20° to +30°C.

6. The Detector Calibrations

The system required four types of calibration. First, the n-γ detector had to be calibrated for energy. Second, the two-parameter PHA response had to be measured for known pulse heights. Third, the rejection efficiency of the charged particle system had to be determined. Fourth, the IFC had to be calibrated for counting rate and light yield.

The n-γ detector was calibrated for energy with both neutrons and gamma rays. Recoil proton pulse spectra from both the (D,D) and the (D,T) neutron reactions were recorded. Compton electron pulse spectra from Na^{22}, Th^{228}, and Am Be gamma-ray sources were recorded. All data were recorded on both a linear, 400-channel PHA and the two-parameter PHA for flight use. The raw data for the neutron and gamma-ray calibrations are shown in Figures 14a, 14b, 15a, and 15b.

For gamma rays the 3/4 peak-height channel (Keszthelyi et al., 1961) was used as the Compton edge, the energy of which was calculated from the relation (Birks, 1964) $E(\text{Compton}) = E_\gamma \, (2a/1 + 2a)$, where $a = (E_\gamma/m_e \, c^2)$. For neutrons, the 1/2 peak-height channel was proportional to the maximum neutron energy. In order to determine any PM non-linearities and make the necessary corrections, the theoretical relation due

to Birks (1951) was applied:

$$dL/dX = (S\ dE/dX)/[1 + (kB)(dE/dX)]$$

where for electrons (1-10 Mev) dE/dX is small and kB is much less than one. This simplifies the relation, $L = S \cdot E$ (Compton). However, in order to obtain this simple linear relation between the Compton energy (E) and the pulse height (L) for the PM used in our flight experiment, we had to correct for PM non-linearities. We corrected for this slight non-linearity by using four well known discrete energies--Na^{22}, Th^{228}, Am Be, and (D,T) (Figures 14 and 15). The resulting correction for non-linearity is shown in Figure 16. After correcting for this non-linearity the results agreed with those of the Oak Ridge National Laboratory report of V. V. Verbinski et al. (1968) for a similar cell of NE 213 (Figure 11).

The two-parameter, logarithmic PHA built for the balloon flight had to be calibrated. An RC-shaped, precision pulse generator was fed in parallel to both the $\int Ldt$ and the dL/dt inputs of the PHA as well as to a linear, 400-channel PHA. The measured logarithmic relation between the flight PHA and the linear PHA is shown in Figure 17.

The effectiveness of the charged particle shield was tested with cosmic-ray secondary muons in the laboratory. The shield was mounted between the two components of a muon telescope. Each component of the telescope consisted of a 2.5 cm thick by 7.6 cm diameter NE 102 scintillator. Both the proper pulse-height range and coincident time difference

(1×10^{-6} sec) were demanded upon events counted as mesons in the telescope. Under these conditions the relativistic muons produced a Landau pulse distribution in both components of the telescope. Any coincident event in the shield which was larger than the sum-coincidence voltage discriminator was regarded as due to a relativistic muon passing through the shield. During a continuous 80 hour test of the flight shield 1051 events were recorded in the muon telescope and 1050 were recorded in the charged particle shield. Thus, the effectiveness of the shield is estimated to be ~99.9%. To obtain a more accurate measure of this rejection with cosmic-ray muons was considered to be both unnecessary and very time consuming. Such a test would require a three component, triple coincidence telescope to reduce the random chance coincidence rate ($2N_1 N_2 \tau$). This would improve the reliability by a factor of 10 so that a rejection ratio of $1/10^4$ could be measured.

The possible leakage of charged particles through the shield was also estimated from the flight data. The n-γ detector recorded counts from two types of logic requirement: (n,γ,p,e) counts and (n-γ) counts. At Pfotzer maximum during the flight (Figure 18) the following rates were obtained (n,γ,p,e) $\simeq$ 53.3 counts sec^{-1}, (n,γ) $\simeq$ 14.8 counts sec^{-1}, and charged particles $2.52\ 10^3 \simeq$ counts sec^{-1}. The ratio of the total area of the inner n-γ detector to the outer charged-particle shield was 2.32 percent. Since the measured charged-particle count rate at the Pfotzer maximum

was 2.52 10^3 sec^{-1}, we would expect the inner detector to be subjected to maximum charged-particle count rate of (2.32 10^{-2} x 2.52 10^3 sec^{-1}) 58.5 sec^{-1}. The bulk of these would be electrons for two reasons. First, there are approximately ten times more electrons than protons in the atmosphere (Figure 2). Second, at equal energies, the range of the electron is greater than that of the proton. Therefore, more electrons penetrate through the shield and the associated internal mass into the inner detector. During the balloon experiment the inner detector recorded (53.3 - 14.8) charged particles sec^{-1} or 38.5 charged particles sec^{-1} at the Pfotzer maximum. This rate is to be compared to the previously calculated maximum charged-particle count rate on the inner detector of 58.5 charged particles sec^{-1}. The difference or loss of particles is the result of absorption by the mass of the shield and inner components. The counting rate from the possible ineffectiveness of the charged-particle shield can also be estimated.

Taking the measured shield leakage of $1/10^3$, the inner detector will receive (10^{-3} x 38.5) charged particles sec^{-1} or 4 x 10^{-2} charged particles sec^{-1}. However, since the n-γ count rate was 14.8 sec^{-1}, the overall contamination is only 0.04/14.8 or .27 percent, the majority of which is due to electrons. We feel this error is acceptable relative to other errors in the experiment.

The two-parameter ($\int$Ldt x dL/dt) IFC pulse spectrum is shown in Figure 19 along with the background of neutrons

and gamma rays detected at Pfotzer maximum. The corresponding one-parameter $\int Ldt$ pulse spectrum of the IFC is seen from Figure 20 to be composed of two peaks. The location of these peaks on the two-parameter PHA output constitutes a simple but accurate monitor of the stability of the system. A peak shift of one logarithmic PHA channel would constitute a gain change of 3.7 percent along the ($\int Ldt$) axis and 3.7 percent along the (dL/dt) axis. The IFC measured count rate was 3.4 sec^{-1}. Any significant change of this measured radioactive-decay rate serves as an indicator of system difficulties such as dead time limitations.

CHAPTER VI

MEASUREMENTS AND RESULTS

1. Introduction

The system was flown on a 5×10^6 ft^3 balloon launched from Palestine, Texas (geomagnetic coordinates 41°52' N, 49°39' W) at 5:18 C.D.T. September 7, 1968. The gondola was composed of two packages: the first contained the detector (47 lbs), and the second, all other electronics and battery supplies (315 lbs). The detector package was about nine feet above all other packages to reduce local secondary production effects from degrading the results. The flight trajectory is shown in Figure 21. A graph of the altitude pressure profile as a function of time is shown in Figure 22. Data was collected for approximately 11 hours, after which the flight was terminated and the package recovered in good operating condition.

From a detailed examination of all recorded data, it was discovered that the twisting of the balloon during the flight had caused a break in one signal lead running from the detector to the electronics box. This may have caused the failure of the anticoincidence logic associated with the charged-particle shield. Fortunately, the system operated satisfactorily through the Pfotzer maximum, which provided sufficient data on the first balloon flight to evaluate the neutron detecting system.

The uncorrected (∫Ldt, dL/dt) data obtained from 16.4 K ft to above the Pfotzer maximum is shown in Figure 12. It can be seen that the PSD system separated, in addition to IFC pulses, three different pulse shapes corresponding to electrons, protons, and alpha particles. All three types of charged particles are the result of neutral particles interacting with the organic scintillator. The Compton electrons arise from gamma-ray interactions with atomic electrons, the recoil protons are produced by H (n,p)n' and C^{12}(n,p)B^{12} reactions, and the alpha particles by C^{12}(n,α) Be^{9} and C^{12} (n,n')3α reactions. Each of these secondary charged particles will be considered in deriving the neutron spectrum at the Pfotzer maximum.

From the raw data obtained from 16.4 K ft to 40 K ft and from 40 K ft to 63 K ft, shown in Figures 23 and 19, we wish to extract only the recoil-proton counts per channel. However, because the statistics involved are poor, we combine these two figures by adding the corresponding counts in each ∫Ldt x dL/dt bin, the combined data being shown in Figure 12. We are now able to separate more reliably the proton data or "track" from the other data (e, α, IFC). After determining the proton distribution in Figure 12, we return to Figures 23 and 19 and separately extract from the same regions of (∫Ldt, dL/dt) as determined from Figure 12 the respective proton-count spectra. These are shown in Figures 24a and 24b. Although these two spectra differ in intensity by a factor of 2.54, they are similar in spectral shape within

statistical uncertainties. This can be ascertained by comparing Figures 23 and 19. Therefore, we have added them together to obtain the better statistics shown in Figure 24c. These are the data from which we will subsequently determine the neutron energy spectrum.

Since the data is now an average over a large altitude change, we need to scale this average counting rate to the counting rate at a specific altitude. The most relevant altitude within the range is that corresponding to the Pfotzer maximum (53.2 K ft, or ~100 mb). In order to determine the appropriate scale factor between the average count rate measured from 16.4 K ft (541 mb) to 63.0 K ft (62 mb) and the count rate at the Pfotzer maximum, we used the average (n,γ) scaled count rate at 100 mb obtained from the number 14 subcarrier (Figure 13a) minus 3.4 IFC counts per second. This was compared with the average (n,γ) count rate obtained from the recoil-proton, Compton-electron, and alpha-particle total counts in Figure 12 divided by the integration time for Figure 12 of 49 minutes.

$$R = \frac{C' - C_{IFC}}{\langle C \rangle}$$

where C' is the n, γ, α, IFC count rate measured from subcarrier 14 (Figure 13a) and C_{IFC} is the measured IFC count rate of 3.4 counts/sec. <C> is the average count rate derived from Figure 12. <C> is the total of all counts minus the total number of IFC counts in Figure 12 divided by the total accumulation time in Figure 12 of 49 minutes.

Since this is an involved procedure, we will show more details. The total number of counts in Figure 12 is 41,221. This is made up of 10,068 IFC counts, 28,468 γ counts, 2,001 n counts, 202 α counts, and the remainder (482) represents counts in the saturation channels ($\int$Ldt > 63) and noise. Therefore, the average count rate <C> between 16.4 K ft to 63.0 K ft not including the IFC counts is: (41,221 - 10,068)/49 x 60 or 10.6 counts/sec. This will be compared with the count rate at Pfotzer maximum measured with the on-board n,γ scaled (÷20) count-rate scalars C_i, 18.6 counts/sec. However, since 3.4 counts/sec of this rate is due to the IFC (C_{IFC}), we first must subtract 3.4 counts/sec from the 18.6 counts/sec or ($C' - C_{IFC}$) is 15.2 n-γ counts/sec.

Thus, the ratio R of these two n-γ count rates is [$R = (C' - C_{IFC})/\langle C \rangle$] (15.2/10.6) or 1.42. Therefore, if we assume the ratio of gamma rays to neutrons remains constant between 16.4 K ft to 63.0 K ft, we can use a scale factor of 1.42 to shift the averaged data derived from Figure 12 to that expected at the Pfotzer maximum.

With data in Figure 12, the measured average ratio of Compton-electron events to recoil-proton events was (28,468/2001) 14.2. The corresponding ratio of secondary alpha-particle events to recoil-proton events was (202/2001) 0.10.

2. Measurements

The IFC ($\int$Ldt pulse) spectra extracted from Figures 23 and 19 are shown in Figure 27 for two consecutive ~24

minute time intervals from 16.4 K ft to above the Pfotzer maximum. Two important types of information are obtained from these IFC data: two-parameter gain stability and counting rate stability. There are two small interdependent corrections required before these two stabilities can be used. These are the changes in the analyzer dead-time due to the external counting rate changes, and the shifts in the spectrum from the Compton electrons produced by atmospheric gamma rays incident upon the small NaI (Tℓ, Am^{241}) IFC crystal. Since these effects are compensating and each amounts to less than 3%, they were neglected.

The recoil-proton ∫Ldt-pulse spectrum extracted from the flight data previously shown in Figure 12 is plotted in Figure 24. Since all recoil proton spectrums from 16.4 K ft to Pfotzer maximum were similar in shape as shown in Figure 28, we added them to improve statistics and scaled all final data rates to those measured at the Pfotzer maximum. The composite spectrum shown in Figure 24 included all the proton recoil data from 16.4 K ft (541 mb, 5:36 D.C.T.) to 63.0 K ft (62 mb, 6:25 C.D.T.). The different particle separations shown in Figure 12 readily allowed an unambiguous separation of electrons from protons. Closer examination of the upper right-hand side of Figure 12 showed that alpha particles could be separated from recoil protons.

The alpha particles produced in the scintillator for this same integrated period of 49 minutes were extracted from Figure 12 and are shown separately in Figure 25. Al-

though the alpha particle-proton interface of Figure 12 was not as distinct as the proton-electron interface, we believe that sufficient separation was realized in Figure 12 to justify the plot shown in Figure 25.

The Compton-electron ∫Ldt-pulse height spectrum for the same 49 minute period was also obtained from Figure 12 and is shown in Figure 26. This Compton-electron pulse spectrum was clearly separated in Figure 12 from the recoil-proton pulse spectrum.

An important overall consideration is the very different spectral shape and intensity of the pulse spectra for α-particles, protons, and electrons in Figures 24, 25, and 26. This difference is conspicuous between the Compton-electron and recoil-proton data. The significance of this difference and its relationship to the PSD resolution necessary will be discussed later.

3. Results

The IFC pulse spectrum was extracted from Figures 23 and 19 and is shown in Figure 27. The ∫Ldt gain change was calculated from Figure 27 to be less than 3 percent. This represents an upper limit to the minimum observable shift in the centroids of the two peaks.

The IFC was also used to check for any count-rate dead-time limitations. This was done by integrating the IFC pulse height spectra of Figure 27 and comparing it to the measured preflight IFC count rate of 3.4 $\pm$ 0.1 counts

sec^{-1}. The integrated flight count rate was also 3.4 $\pm$ 0.1, where the error reflects the inaccuracy of the total integration time for Figure 27 (i.e., 49 $\pm$ 1 minute). Therefore, we believe that any dead-time effects must be less than 3 percent.

The recoil-proton $\int Ldt$ pulse spectrum of Figure 24 was used to derive the neutron energy spectrum. The unfolding details are given in Appendix E. The recoil-proton energy spectrum scaled to the measured rate at Pfotzer maximum is given in Figure 28 and the unfolded incident neutron energy spectrum in Figure 29. The neutron spectrum could not be simply represented with the normal power law of $dN/dE = BE^{-\beta}$ with B and β remaining constant over the entire neutron energy range of 3 Mev to 20 Mev. However, for comparison with other research we have calculated the value of B and β as a function of neutron energy. These are summarized in Figure 32 for the flight data near the Pfotzer maximum.

The secondary alpha particle energy spectrum was unfolded from the data in Figure 25 and is given in Figure 30. The spectrum was scaled to the count rate measured at the Pfotzer maximum.

From the pulse height spectrum of Figure 26, we unfolded the Compton-electron energy spectrum in Figures 31a, 31b. This energy spectrum is uncorrected for the electron range. Since this is a serious correction which is not completely understood, we will not attempt to unfold the incident gamma-ray spectrum. However, the influence of the electron-

recoil spectrum on the proton-recoil spectrum is important and will be discussed later.

CHAPTER VII

CONCLUSIONS AND DISCUSSIONS

The energy spectrum of fast neutrons at the Pfotzer maximum is not a simple power law of the form: $dN_n/dE = B\ E^{-\beta}$ with B and β remaining constant over the entire neutron energy range of 3 to 20 Mev. In particular, the slope of the neutron energy spectrum is a function of energy, β (E). However, as an approximation to this power law spectrum we find that the range of the slope β (E) of the neutron energy spectrum is 4.1 ± 0.5 at 3 Mev and smoothly decreases to 1.2 ± 0.5 at 20 Mev. No statistically significant change in spectral shape with respect to atmospheric depth was measured from 541 mb to 62 mb.

The integrated neutron flux at Pfotzer maximum between 3.5 Mev and 10.0 Mev was calculated to be 0.36 neutrons/cm^2-sec.

Now, let us compare these results with other experimental values. Mendell (1963) determined the neutron energy spectrum at 90 K ft (17.7 gm/cm^2) to be $dN_n/dE = 2.6\ \bar{E}^{(1.16\pm0.2)} \exp - (0.0069X)$ neutrons/cm^2-sec-Mev, where X is the atmospheric depth in gm/cm^2. The Pfotzer maximum was observed at 75 gm/cm^2 and the attenuation length was determined to be 145 ± 6 gm/cm^2. This measurement was made at a geomagnetic latitude of 53^o on June 22, 1962. Although this observation was at a different geomagnetic latitude than ours (42^o), we can convert their measurement to 42^o by

the use of Figure 1 of Lingenfelter (1963) for the solar minimum, cosmic-ray neutron production. We find that the latitude conversion factor for the flux from 53° to 42° is ~0.56.

In addition, the correction due to the change in flux with solar cycle on the flight day must be included (Sept. 7, 1968). The relative Mt. Washington neutron monitor rate was 2102, whereas in the 1954 or 1965 solar minimum the rate was 2505 (Lockwood, 1968). Therefore, the related fractional decrease in the high-energy cosmic-ray flux as indicated by the Mt. Washington neutron monitor was about 16%. The fractional decrease in the neutron leakage flux due to the solar cycle change was estimated from Table 1 of Lingenfelter (1963) at 40° latitude for the energy range 1-10 Mev as 0.76. Thus, the overall solar cycle decrease for the fast neutron flux in the atmosphere was (0.76 x 0.16) ~12%.

These two effects of latitude and solar cycle can be applied to the neutron flux of Mendell. This will involve a change by a factor of (0.56) (1-0.12) = 0.49. Therefore, the spectrum of Mendell is $dN_n/dE = (0.49)\ (2.6)\ E^{-(1.16 \pm 0.2)}\ \exp - (0.0069X)$ neutrons/cm^2-sec-Mev after conversion to the solar cycle and latitude conditions of our flight. The original, uncorrected spectrum of Mendell at 1962 is shown in Figure 34 as the solid curve and the corrected curve is shown as the dotted curve.

In order to compare the results of this thesis to those of Mendell we have calculated the flux which we measured

in the overlapping energy region. The flux from 3.5 Mev to 10 Mev for Mendell's flight is (1.15) (0.49) = .56 neutrons/cm^2-sec after conversion to ~42^o latitude and to the effective solar cycle of Sept. 7, 1968. The corresponding neutron flux for our Sept. 7, 1968 measurement at 42^o latitude was 0.36 neutrons/cm^2-sec. The difference in these two flux measurements is about 50%, our measurement being about 60% of Mendell's value.

Consequently, there appear to be some definite disagreements with respect to both the spectral shape and flux. However, since the measurements of Mendell were made at an altitude of 90 K ft while our measurements were taken at less than 63 K ft, some difference may be attributed to a change in spectrum shape with altitude above the Pfotzer maximum or some experimental difficulties may be present in either experiment. In order to check for any change in spectrum shape with altitude below the Pfotzer maximum, we found that there was no statistically significant difference in shape between 15.4 K ft to 63.0Kft. However, we have no measurements above 63.0 K ft. We believe that some of the very difficult experimental problems to be overcome in atmospheric fast-neutron measurements are the main reason for the differences.

The first such problem involved in such experiments is that of a reliable, high-resolution pulse shape discriminator to separate gamma rays and neutrons. The count rate of gamma rays in our measurements was a factor of ~14.2 greater

than that of the neutrons in the energy range covered. More importantly, since the Compton-recoil pulse-spectrum (Figure 26c) is much harder and more intense than the recoil-proton pulse spectrum (Figure 24c) any difficulties in PSD particle identification will certainly result in a harder, more intense neutron energy spectrum. In particular, for the measurements of Mendell at 90 K ft the ratio of gamma-ray counts to neutron counts was 2/1, while the ratio at 63 K ft for our experiment was 14.2/1. Since the absorption lengths for gamma rays and neutrons are approximately equal, we would expect the ratio of gamma rays to neutrons to be approximately independent of atmospheric depth. Therefore, this vast difference in the ratio of gamma rays to neutrons may be an experimental effect.

Another experimental difficulty is the reliable anticoincidence shielding of the neutron detector from the primary and secondary cosmic-ray charged particles. We found the approximate ratio of charged particles to neutrons in the same light pulse region to be ~40/1 at the Pfotzer maximum. The pulse spectrum due to charged particles was measured to be very similar to the Compton-recoil pulse spectrum, i.e., a very hard, more intense spectrum compared to the recoil-proton pulse spectrum. Therefore, should a small fraction of the charged particles be allowed to pass through the anti-coincidence charged-particle shield without being gated-off, we would observe a more intense and harder pulse spectrum. In particular, the charged-particle

ahielding provided by the phoswich technique may seriously reduce the effectiveness of the PSD. Figure 35 was reproduced from Mendell (1963) as an example of the phoswiching method for charged-particle shielding. A small fraction of the combination of charged particles and gamma rays may "leak" into the neutron channels as shown in Figure 35a. Such an effect could produce a harder, more intense spectrum.

Another less serious experimental difficulty in such measurements is that of the neutron-produced secondary alpha particles. Since the single-parameter type of PSD (Mendell, 1963) systems cannot separate alpha particles from protons, a 10% excess from alpha particle contamination will be included in the recoil-proton spectrum again producing a more intense flux.

Although we believe there may be many possible ways in which measurements of neutron spectra may be seriously contaminated by"leakage" from gamma rays, charged particles and alpha particles, another difficulty may be that of recoil-proton spectrum unfolding. This difficulty is really introduced by the form in which others have approximated the neutron energy spectrum and/or the recoil-proton energy spectrum. We find that should we approximate either spectrum with a simple power law of the form $dN/dE = AE^{-\alpha}$, the other corresponding spectrum will not also be a simple power law, but will have a non-constant slope $\beta(E)$ with respect to energy. However, most investigators have

assumed the simple power law as applicable simultaneously to both the recoil-proton and the neutron energy spectrum (i.e., Holt et al., 1966). Thus, we believe that many interrelated difficulties, (i.e., gamma ray "leakage" of PSD, charged particle "leakage" of phoswich-PSD combination, alpha particle contamination, and spectrum unfolding procedures) all combine to produce a more intense and harder "neutron" energy spectrum.

We find the slope of neutron energy spectrum to vary with energy. Since the neutron energy spectrum shows a continuous flattening with increasing energy from 3 to 20 Mev, we believe that the theoretical extrapolations of the high-energy albedo-neutron leakage flux beyond the energy range of the measurements is extremely unsound. Consequently, since we have found that the neutron-leakage energy spectrum becomes harder with increasing energy, the fraction of high-energy neutrons decaying to produce protons in the magnetosphere may be larger than previously indicated by theory (Lingenfelter, 1963) and experiment (Mendell, 1963).

CHAPTER VIII

SUGGESTIONS FOR FUTURE WORK

Although there are many problems in making reliable high-energy albedo-neutron measurements, some simple suggestions are apparent.

1. Two-parameter PSD analysis allows more reliable particle separations ($M_{\gamma,n} \approx 3$) and multiple-particle separation (i.e., e, p, α).
2. Since the low count rate of the 2 inch x 2 inch neutron detectors in the fast neutron energy region yields poor statistics in the normal experiments, the scintillators should be increased to 3 inch x 3 inch to improve the count rate by a factor of ~ 2.25.
3. Two such 3" x 3" cells mounted on separate PM's and placed within a dome-type charged-particle shield could be used as a directional neutron detector. The system would also effectively work in the normal, uncorrelated spectral mode to measure the neutron energy spectrum. The directional coincident events need only be distinguished as gamma rays or neutrons and as either moving upward or downward. The necessary logic is easily accomplished. No difficult measurements of energy by means of time-of-flight need to be made.
4. A ballooning technique to maintain a sequential series of increasing equilibrium altitudes hsould be developed to allow more time at various intermediate altitudes.

This might be accomplished by beginning the balloon flight with a great excess of ballast and sequentially dropping some ballast to maintain a stepped series of new "float" altitudes. Such a novel ballooning technique coupled to a directional neutron detector would yield more accurate albedo-neutron leakage flux determinations with respect to altitude. Curves such as those obtained by Haymes (1964) and reproduced in Figure 3 would allow extrapolations of the albedo-neutron leakage flux to be more reliable. This would also boot-strap the theoretical approximations involved in using the Boltzmann transport theory beyond ~100 gm/cm^2 near the upper edge of the atmospheric boundary.

5. Should more accurate C^{12} (n,α) cross-sections become available, we believe the two-parameter PSD method of extracting the secondary alpha particle spectrum cuased by C^{12} (n,α) reactions could be effectively used to compliment the normal n,p mode and go to much higher neutron energies.
6. Combinations of alkali-halide and organic scintillations could be optically coupled to one PM and be two-parameter, pulse-shape discriminated simultaneously for different particles as well as for different scintillators. This might allow one to extract a high-resolution neutron spectrum and a low-resolution, Compton-recoil gamma-ray spectrum from the organic while at the same time to extract the correlating high-resolution gamma-ray spectrum

from the adjacent alkali-halide crystal, each with optimum resolution, yet each complimenting and confirming the other.

7. A small fast-neutron, two-parameter PSD system should be jettisoned or separated from a larger "mother" satellite or placed at the end of a boom to reliably measure the neutron leakage flux in orbit.
8. All neutron-gamma ray atmospheric PSD measurements should be pre-calibrated with the use of high-energy gamma rays (E_γ > 10 Mev) and high energy charged particles (atmospheric relativistic muons) to ascertain both the PSD identification and the reliability of the charged-particle shielding.

BIBLIOGRAPHY

Alexander, T. K. and F. S. Goulding, An amplitude-insensitive system that distinguished pulses of different shapes, Nucl. Inst. and Methods, 13, 244-247, 1961.

Al-Kital, R. A. and R. A. Peck, Jr., $C^{12}(n,\alpha)$ Be^{9} reaction induced by 14-Mev neutrons, Phys. Rev., 130, 1500-1503, 1963.

Axford, W. I. and C. O. Hines, A unifying theory of high-latitude geophysical phenomena and geomagnetic storms, Can. Journal of Phys., 39, 1433-1464, 1961.

Baird, G. A. and B. G. Wilson, Solar minimum measurements of fast neutrons at high altitude, Can. Journal of Physics, 44, 2131-2136, 1966.

Batchelor, R., W. B. Gilboy, A. D. Purnell, and J. H. Towle, Improvements in the fast neutron time of flight technique using pulse shape discrimination in an organic phosphor, Nucl. Instr. and Methods, 8, 146-148, 1960.

Bethe, H. A., S. A. Korff, and G. Placzek, On the interpretation of neutron measurements in the cosmic radiation, Phys. Rev., 57, 573-587, 1940.

Birks, J. B., Scintillations from organic crystals: specific fluorescence and relative response to different radiations, Proc. Phys. Soc., A-64, 10, 874-877, 1951.

Birks, J. B., The Theory and Practice of Scintillation Counting, p. 27, Macmillan Co., New York, 1964.

Bock, J. K. and J. V. Lanahan, A machine code for the unfolding of pulse height spectra, U.S. Army Ballistic Research Laboratory, Report BRL MR 1790, AD645283, 1966.

Boella, G, G. Degli Antoni, C. Dilworth, M. Panetti, and L. Scarsi, Measurement of the cosmic ray neutron flux at 4.6 billion volts geomagnetic cutoff rigidity, J. Geophys. Res., 70, 5-9, 1965.

Broek, H. W. and C. E. Anderson, The stilbene scintillation crystal as a spectrometer for continuous fast-neutron spectra, Rev. of Sc. Instr., 31, #10, 1063-1069, 1960.

Brooks, F. D., Organic scintillators, Prog. Nuc. Phys., 5, 252-313, 1956.

Brooks, F. D., A scintillator counter with neutron and gamma-ray discrimination, Nuc. Instr. and Meth., 4, 151-163, 1959.

Brunfelter, B., J. Kockum, and H. O. Zetterstrom, Unscrambling of proton recoil spectra, Nuc. Instr. and Meth., 40, 84-88, 1966.

Carlson, B. G. and G. I. Bell, Solution of the transport equation by the S_N method, Proc. Intern, Conf. Peaceful Uses of Atomic Energy, 2nd Geneva, 1958.

Chatterjee, M. L. and B. Sen, The (n,α) reaction on C^{12} at 14 Mev, Nucl. Phys., 51, 583-587, 1964.

Daehnick, W. and R. Sherr, Pulse shape discrimination in stilbene scintillators, Rev. Sci. Instr., 32, 666-670, 1964.

Dragt, A. J., M. M. Austin, and R. S. White, Cosmic ray and solar proton albedo neutron decay injection, J. Geophys. Res., 71, 1293-1304, 1966.

Evans, R. D., The Atomic Nucleus, p. 332, McGraw-Hill Book Co., New York, N.Y., 1955.

Ewald, R. and A. Sarkardy, A low cost-low power multichannel pulse-height analyzer for university balloon and rocket experiments, IEEE Transactions on Nuclear Science, 537-553, NS-13, 1966.

Fenton, K. B., A search for a particle trapped in the geomagnetic field, J. Geophys. Res., 72, 3889-3894, 1967.

Fermi, E., On the origin of cosmic radiation, Phys. Rev., 75, 1169-1174, 1949.

Forte, M., A. Konsta, and C. Maranzana, Electronic methods for discriminating scintillation shapes, European Atomic Energy Community, CCR, ISPRA Italy 1961, 277-286, 1961.

Fowler, J. L. and J. E. Brolley, Monoenergetic neutron techniques in the 10- to 30- Mev range, Rev. Mod. Phys., 28, 103-109, 1956.

Freden, S. C. and R. S. White, Protons in the earth's magnetic field, Phys. Rev. Letters, 3, 9-11, 1959.

Freden, S. C. and R. S. White, Trapped proton and cosmic-ray albedo neutron fluxes, J. Geophys. Res., 67, 25-29, 1962.

Friling, L. and D. Schow, U.N.H. Tech. Report, 1968.

Gibson, W. A., Design of photomultiplier socket assembly with high gain and clean output signals for tube viewing organic scintillator light pulses, Rev. Sci. Instr., 37, 631-635, 1966.

Gol'damskic, R., Emission of secondary neutrons from nuclei bombarded by high energy neutrons, Phys. Rev., 109, 1762-1769, 1958.

Graves, E. R. and R. W. Davis, Cross sections for nonelastic interactions of 14-Mev neutrons with various elements, Phys. Rev., 97, 1205-1210, 1955.

Halliday, D., Introductory Nuclear Physics, 2nd edition, p. 315, John Wiley & Sons, New York, 1955.

Hawshaw Chemical Corp., Cleveland, Ohio, Integral Light Pulser.

Haymes, R. C., Fast neutronsin the earth's atmosphere 1. Variation with depth, J. Geophys. Res., 69, 841-852, 1964.

Haymes, R. C., Fast neutrons in the earth's atmosphere 2. Time variations at high altitudes, J. Geophys. Res., 69, 853-859, 1964.

Hess, W. N., Summary of high-energy nucleon-neucleon cross-section data, Mod. Phys., 30, 369-372, 1958.

Hess, W. N., Van Allen belt protons from cosmic-ray neutron leakage, Phys. Rev. Letters, 3, 11-13, 1959.

Hess, W. N. and A. J. Starnes, Measurements of the neutron flux in space, Phys. Rev. Letters, 5, 48, 1960.

Hess, W. N., E. H. Canfield, and R. E. Lingenfelter, Cosmic-ray neutron demography, J. Geophys. Res., 66, 665-667, 1961.

Hess, W. N., Energetic particles in the inner Van Allen belt, Space Sci. Rev., 1, 278-312, 1962.

Hess, W. N., Introduction to Space Science, edited by W. N. Hess, 173, Gorden and Breach Science Publishers, New York, 1965.

Hess, W. N. and J. Killeen, Spatial distribution of protons from neutron decay trapped by the geomagnetic field, J. Geophys. Res., 71, 2799-2810, 1966.

Hess, W. N., Radiation Belt and Magnetosphere, edited by W. N. Hess, 120, Blaisdell Publishing Co., 1968.

Holt, S. S., R. B. Mendell, and S. A. Korff, Fast neutron latitude variations in the atmosphere at solar minimum, J. Geophys. Res., 71, 5109-5116, 1966.

Howerton, R. J., Semi-empirical neutron cross sections, 0.5-15 Mev, Univ. of Cal. Rad. Lab., U.C.R.L.-5351, TID 4500, 14th edition, UC34, Phys. and Math, 1958.

Huck, A. and G. Walter, Detection des neutrons rapides a l'aide d'un scintillateur organique: étude théorique et experimentale des distributions de protons de recul, Nucl. Instr. and Meth., 59, 157-162, 1968.

Kaufmann, R. L., Experimental tests for the acceleration of trapped particles, J. Geophys. Res., 68, 371-386, 1963.

Kellogg, P. J., Possible explanation of the radiation observed by Van Allen at high altitudes in satellites, Nuovo Cimento (10), 11, 48-66, 1959.

Keszthelyi, I. Berks, I. Demeter, and I. Fodor, Detection of high energy γ-rays by plastic phosphors, Nucl. Instr. and Meth., 10, 199, 1961.

Koehler, D. R., J. T. Grissom, A fast neutron spectrometric technique, Nucl. Instr. and Meth., 40, 235-237, 1966.

Kopsch, D. and C. Cierjacks, Alpha-proton discrimination with a NE213 liquid scintillator used for the measurement of the (n,α) reaction on C^{12}, Nucl. Instr. and Meth., 54, 277-281, 1967.

Krimigis, S. M. and J. A. Van Allen, Geomagnetically trapped alpha particles, J. Geophys. Res., 72, 5779-5788, 1967.

Kurz, R. J., A 709/7090 Fortran II program to compute the neutron-detection efficiency of plastic scintillators for neutron energies from 1 to 300 Mev, PhD thesis U.C.R.L.-11339, UC-34 Physics-TID-4500 (24th edition) Univ. of Cal.-L.R.L., Berkeley, 1964.

Lal, D., and B. Peters, Cosmic-ray produced radioactivity on the earth, Handbuch Der Physik Cosmic Rays II, Band XL V1/2, 551-612, Springer-Verlag, New York, N.Y., 1967.

Lingenfelter, R. E., The cosmic-ray neutron leakage flux, J. Geophys. Res., 68, 5633-5639, 1963.

Lingenfelter, R. E., Production of carbon 14 by cosmic-ray neutrons, Res. Geophys., 1, 35-55, 1963.

Lockwood, J. A., Private Communication

Madey, R., A spectrometer for energetic neutrons, IEEE Trans. on Nuc. Sci., 426-436, 1968.

Marion, J. B. and J. L. Fowler, editors, Fast Neutron Physics, Interscience Publishers, Inc., New York, N.Y., 258, 1960.

Mehetretter, Private Communication, Stratoscope, Germany, 1968.

Mendell, R. B., Fast-neutron flux in the atmosphere, PhD thesis, N.Y.U., 1963.

Mendell, R. B. and S. A. Korff, Fast-neutron flux in the atmosphere, J. Geophys. Res., 68, 5487-5495, 1963.

Miyake, S., K. Hinotani, I. Katsumata, and T. Kaneko, Cosmic-ray nuclear interactions in nitrogen gas, J. Phys. Soc. Japan, 12, 845-854, 1957.

Mössner, J., G. Schmidt, and J. Schintlmeister, Untersuchung der reaktion C^{12} (n,n') 3α, Nucl. Phys., 75, 113, 1966.

Naugle, J. E. and D. A. Kniffen, Flux and energy spectra of the protons in the inner Van Allen belt, Phys. Rev. Letters, 7, 3-6, 1961.

New England Nuclear Corp., Boston, Mass.

Newkirk, L. L., Calculation of low-energy neutron flux in the atmosphere by the S_N method, J. Geophys. Res., 68, 1825-1833, 1963.

Northrop, T. G., The Adiabatic Motion of Charged Particles, Interscience Publishers, New York, 1963.

Olbert, S., and R. Stora, Theory of high energy N-component cascades, Annals Physics, 1, 247-269, 1957.

Owen, R. B., A. E. R. E. Harwell, Report No. EL/R2712 (1958) and I.R.E. Transactions on Nuclear Science, NS-5, No. 3, 198, 1958.

Patel, V. L., Low frequency hydromagnetic waves in the magnetosphere, U.N.H. Report, 64-5, 1964.

Poole, M. J., The inelastic scattering of fast neutrons, Phil. Mag., 43, 1060-1069, 1952.

Poole, M. J., Neutron flux and spectrum measurement, Proc. Phys. Soc., A, 65, 453-454, 1952.

Reid, W. B., and R. H. Hummel, Pulse shape discrimination in organic scintillators, Can. Nuc. Tech., Jan-Feb, 1966.

Rossi, B. B., High-Energy Particles, Prentice Hall, New York, 1952.

Roush, M. L., M. A. Wilson, and W. F. Hornyak, Pulse shape discrimination, Nuc. Instr. and Meth., 31, 112-124, 1964.

St. Onge, R. N. and J. A. Lockwood, A fast-neutron gamma detector for space research, IEEE Trans. Nuc. Sci., 15-1, 264-267, 1967.

St. Onge, R. N. and J. A. Lockwood, A total enclosing active charged-particle shield, accepted for publication in Nucl. Instr. and Meth., 1968a.

St. Onge, R. N. and J. A. Lockwood, A simple high-resolution pulse shape discriminator, accepted for publication in Nucl. Instr. and Meth., 1968b.

Schwarz, S. and H. O. Zefterstrom, Some remarks on the properties of small organic scintillators as detectors of fast neutrons, Nucl. Instr. and Meth., 41, 93, 1966.

Shklovsky, I. S., V. I. Krassovsky, and Y. I. Galperin, On the nature of corpuscular radiation in the upper atmosphere, Izv. Akad. Nauk. SSSR, Ser. Geofiz. 12, 1261-1268, 1959.

Singer, S. F., Trapped albedo theory at the radiation belt, Phys. Rev. Letters, 1, 181-183, 1958.

Singer, S. F., Cause of the minimum in the earth's radiation belt, Phys. Rev. Letters, 3, 188-190, 1959.

Singer, S. F. and A. M. Lenchek, Progress in Elem. Particle and Cosmic-Ray Physics, Vol VI, edited by J. G. Wilson and S. A. Wouthuysen, Chap. III, Geomagnetically Trapped Radiation, 1962.

Staub, H. H., Experimental Nuclear Physics, edited by E. Segre, Vol. I, Part 1, p. 132. (Staub derived original relation between neutron and proton response), John Wiley & Sons, Inc., New York, 1953.

Trainor, J. H. and J. A. Lockwood, Neutron albedo measurement on polar orbiting satellite, J. Geophys. Res., 69, 3115-3123, 1964.

Van Allen, J. A., G. H. Ludwig, E. C. Ray, and C. E. McIlwain, IGY Satellite Report, it Series no. 3, National Academy of Sciences-National Research Council, Washington 25, D.C., 1958.

Vari-L Co., Inc., (Model #50200E), Stamford, Conn.

Verbinski, V. V., W. R. Burrus, T. A. Love, W. Zobel, N. W. Hill, and R. Textor, Calibration of an organic scintillator for neutron spectrometry, ORNL-TM-2183, to be published in Nucl. Inst. and Meth., 1968.

Vernov, S. N., H. L. Grigorov, I. P. Ivanenko, A. I. Lebedinskii, V. S. Muzin, and A. E. Chudakov, Possible mechanism of production of "terrestrial corpuscular radiation" under the action of cosmic rays, Sov. Phys. Dok., 4, 154-157, 1959.

Wilkinson, D. H., The phoswich-a multiple phosphor, Rev. Sci. Instr., 23, 414-417, 1952.

Wilson, T. E., Production corrections to cosmic-ray neutron albedo measurements, M.S. thesis, U.N.G., 1965.

Wright, G. T., Scintillation decay times of organic crystals Proc. Phys. Soc. (B), 69, 358-372, 1956.

Young, W. R., Neutron spectra from an organic scintillator, PhD thesis, U. Cal. Berkeley, UCRL-16149, 1968.

Zych, A. D., High energy albedo and solar neutrons near the top of the atmosphere, PhD thesis, Case Western Reserve Univ., 1968.

APPENDIX A

A Total Enclosing Active Charged Particle Shield*

R. N. St. Onge and J. A. Lockwood
University of New Hampshire
Physics Department
Durham, New Hampshire

In order to measure accurately the neutron and gamma-ray fluxes at the top of the atmosphere, it is necessary to surround the neutron and gamma-ray detector with an anticoincidence charged-particle shield. Since the ratio of the neutron or γ-ray flux to the charged-particle flux is small, the shield must be very effective (> 99.9%) in rejecting minimum ionizing charged particles. For a series of balloon flights we have designed a 4π active charged-particle shield, which operates in anticoincidence with the enclosed neutron detector. Neutrons are separated from γ-rays in the inner detector by a simple pulse-shape discriminating (PSD) circuit (St. Onge and Lockwood, 1967; St. Onge and Lockwood, 1968). The entire shield has a minimum total mass for the given internal volume and uses only two photomultipliers, both located within the volume of the active shield. The adiabatic light piping concepts used in the shield to minimize the light attenuation from unnecessary corners insures excellent charged-particle

*Accepted for publication, Nucl. Inst. and Meth., 1968.

rejection. Only simple logic circuits are required in the associated electronic system for count rates $\sim 10^3$ sec^{-1}.

The general shape and size of the dome are indicated in the left of Figure 7. Two hollow plastic scintillators (NE102), which are hemispherical sections, are optically mated with a hollow cylindrical section of the same material. A photomultiplier (RCA C70132A) with a curved photocathode is optically potted into the inside of the top section, with the same arrangement in the lower half-section. The effects of both total internal reflection (TIR) and specular reflection (SR) are successfully combined in the shield design. TIR is first used to gather the scintillation light falling within the acceptance angles defined by Snell's law. Second, SR from the crinkled aluminum foil, loosely wrapped around the entire dome, rechannels to the photomultiplier that light failing to meet the initial TIR critical angle. Diffuse white paint is applied directly to the outside of the dome areas near each PM to diffusely scatter more light into the PM cathodes.

The outputs from the two photomultipliers are fed separately into parallel sum and coincidence logic to improve the signal to noise ratio as shown in Figure 8. This insures operation under the worst situations where particles do not traverse entirely through the dome, i.e., enter but do not exit. Two such extreme situations will be described. First,

if a charged particle passes through the dome wall near either PM, there will be a very large signal generated at the PM. However, there may be no detectable signal at the distant PM. Thus, the coincidence circuit would probably not be triggered. On the other hand, the summing circuit, which is followed by a voltage threshold discriminator will recognize the very large signal (near PM) added to the very small signal (distant PM). This large signal in the summing circuit triggers the associated lower level discriminator. Such an event would not be reliably detected in the normal coincidence logic. The second extreme situation will occur when a particle enters the cylindrical section about equi-distant from the two photomultipliers and generates small, approximately equal, signals in the two photomultipliers. Hence, the lower level discriminators before the coincidence circuit, which have been set at a lower level than for the summing circuit, are simultaneously triggered to generate a coincidence gate. In this latter situation, the summing network may also superflously generate a signal from its associated lower level discriminator. However, in this case, definitive gating is provided by the coincidence circuit.

Other events produced by particles not traversing the dome will be a combination of the above two extreme cases. For most cases where the charged particle penetrates completely through the dome the gating is provided

by the coincidence logic. Then, the summing circuit provides redundancy.

This design is based essentially upon the shield thickness being compensatingly greater at larger distances from the phototubes. Consequently, the particle produces an appropriately larger signal farther from the phototubes. Further, the light is adiabatically guided to concentrate upon the small region of the PM cathode. To provide this light generating compensation, and yet facilitate manufacturing, the centers of curvature were offset for the inner and outer spherical surfaces. For an initial design criterion we can write:

$$\text{Sum voltage pulses} = V(PM_1) + V(PM_2)$$
$$= f_1(X)\ g_1\ (X) + f_2(X)\ g_2\ (X) = H,$$

where X = distance (cm) along the light path from the particle entry point to the particular PM.

$g_1(X)$ = thickness function for particle entry at X_1,

$f_1(X)$ = attenuation function for light to travel from X_1 to PM_1,

H = a constant independent of X.

And the attenuation was taken to be:

$f(X) = K \exp(-X/20)$, so that the thickness function $g(X) = f(X)^{-1} = K^{-1} \exp(X/20)$.

This function for a single PM is plotted in Figure A-1 over the necessary range of X. Then as a first approximation for the thicknesses in the dome of a 25 cm diameter, the necessary ratio of the maximum to the minimum thickness was taken as ~3/2. This is one-half the ratio shown in Figure A-1 because two PM's are summed in the flight unit. Since the size of the PM cathode required a minimum dome thickness of about 1.11 cm for adequate strength near the PM, the maximum wall thickness at the center section must be about 1.59 cm, which is accomplished by a center offset of 0.48 cm as shown in Figure 7.

After construction of the shield, the experimental response (i.e., the attenuation function for a constant source intensity) of a single PM to the position of an Am^{241} Integral Light Pulser (Harshaw Chemical Corp.) was measured to be approximately:

$$f(X) \simeq 1.18 \exp(-X/2) + 0.15 \exp(-X/50)$$

as shown in Figure A-1. The added first term in f(X) is related to the initial rapid change with X of the solid angle subtended by the source at the PM, neglected in the original design. The second term exp(-X/50) is the normal exponential light attenuation of the curved material.

Based upon this measurement, we can improve the original design. Howeve,r since the exact inverse of f(X) is not a simple function, it is difficult to machine the shield to conform to $f(X)^{-1}$. But as a best

approximation, the ratio of maximum-to-minimum thickness could be made equal to the fractional loss by transmission for the near-to-the-far light paths. From Figure A-1 this is 5.2, which is twice that for two PM's. Thus, the second generation of charged-particle shields to be built should have a maximum thickness of 2.88 cm with a minimum of 1.11 cm which can be obtained by a center offset of 1.77 cm as shown on the right side of Figure 7.

Some n-γ detecting systems have used one photomultiplier to view both the n-γ detector and the charged-particle shield. Such a shield only encloses the n-γ scintillator against secondary production and not the associated PM or electronics. A pulse-shape discrimination (PSD) circuit separated neutrons from γ-rays in the inner detector and a phoswiching technique (Wilkinson, 1952; Mendell and Korff, 1963) gates off the n-γ detector whenever a charged particle passed through the thin phoswich shield. With such a scheme, it is very difficult to provide the necessary high-resolution, unambiguous scintillation light to the PSD system which is required to separate the neutron and gamma-ray spectra (Mendell and Korff, 1963). Scintillations in the phoswich (charged-particle shield) and in the internal scintillator from neutrons and γ-rays become optically mixed. It is then difficult to decompose the light combinations to distinguish the neutrons from the γ-rays, as well as from the charged particles.

Conversely, if simple flat-sheet scintillators are shaped in the form of a box, many ($\tilde{>}$ 6) PM's are required to provide excellent charged-particle rejection. If the PM's are placed inside, the box must be larger than with the dome design. Such a large shield will have high count rates and, consequently, large dead times. Alternatively, teh PM's could be placed outside, but this would increase the cosmic-ray produced secondaries thereby distorting the ambient neutral particle spectra.

We believe that this represents a considerable advance in the design and operation of charged-particle shields for neutron and gamma-ray experiments. A recent balloon flight of several hours duration has shown that the original design is adequate. It is important to note that this minimum mass shield would not work reliably without both the concept of non-uniform thickness and the parallel sum-coincidence electronic logic.

APPENDIX B

A Simple High Resolution Pulse Shape Discriminator*

R. N. St. Onge and J. A. Lockwood
University of New Hampshire
Physics Department
Durham, New Hampshire

1. Introduction

In experiments to measure the fast neutron energy spectrum at the top of the earth's atmosphere, it is necessary to separate the neutron events from the γ-rays, assuming the usual anticoincidence charged-particle shield is included. The pulse-shape discriminating system to be described provides good separation of neutrons from gamma rays over an extensive energy range. For γ-rays the energy resolution obtained with the organic liquid scintillator is good enough to determine the energy spectrum of the γ-rays. The data display method permits the simultaneous determination of both the neutron and γ-ray pulse height spectrums. This pulse-shape discriminator (PSD) has been used to measure the neutron and γ-ray spectra in the atmosphere with balloons and will be incorporated in a forthcoming series of rocket flights to evaluate the energy spectrum of the cosmic-ray neutron leakage flux.

The requirements imposed and successfully realized in the design of the PSD were (1) unambiguous simultaneous

*Accepted for publication, Nucl. Inst. and Meth., 1968.

identification of both particle energy and particle type; (2) wide dynamic range (neutrons, $1 < E_n < 30$ Mev; γ-rays, $0.5 < E_\gamma < 10$ Mev); (3) simplicity; (4) use of passive circuit elements for high temperature stability and low power consumption; and (5) minimum sensitivity to photomultiplier (PM) gain changes. Present PSD methods do not meet all these criteria simultaneously. For example, the many methods suggested by Forte et al. (1961) use fast diodes which have inherently poor temperature characteristics and a limited useful dynamic range. The PSD of Brooks (1959) and later Daehnick and Sherr (1961) is very difficult to adjust over a wide dynamic range, is quite sensitive to any PM gain changes and only the neutron channel is directly displayed. The space charge saturation method first employed by Owen (1958), Batchelor et al. (1960), and Broek and Anderson (1960) has a very limited dynamic range. The method of Alexander and Goulding (1961) is very complex. Zero-crossing methods (Forte et al., 1961; Roush et al., 1964) are also quite involved.

In this paper we will describe the PSD circuit, the method of incorporating an in-flight calibrator into the n-γ detecting system and typical PSD separations of protons from electrons.

2. Description of the PSD Circuit

Since different particles in traversing some scintillators lose energy by exciting the electronic

transitions of organic molecules in a unique manner, the nuclear particle type and energy can usually be simultaneously identified. The excited scintillator subsequently radiates this energy in a particular combination of modes uniquely dependent upon the particle type and its energy loss (Wright, 1956). Discrimination among the different types of particles in a scintillator is usually made by comparing the amplitudes of the fast component to total output of all the decay modes for each particle type (Brooks, 1959). Although it is expected theoretically that the optimum comparison would be between the amplitudes of the fast and the slow components, the system to be described will compare the slow-to-the-total integrated amplitude of all decays. The reason for this method of comparison lies in the saturating, nonlinear characteristics of the PM, i.e., very fast, high-intensity decays cannot be faithfully followed because of space charge saturation. Thus, the use of these distorted fast decays would cause a greater dispersion in the particle separation. Also, the use of the total integrated signal serves a dual purpose. First, the necessary pulse height spectrum can be simultaneously extracted from it. Second, since the total integrated signal must always be greater than either its fast or slow component at the same PM output, the total integrated signal may be picked off at an earlier dynode to avoid any subsequent space charge saturation. Hence, practical considerations dictate the

comparison of the slow-to-the-total pulse amplitudes.

The basic idea of the PSD is the partially destructive and constructive interference of a pair of electronic pulses derived from one PM detector pulse. This one original pulse may be taken either from a dynode or the anode of the PM. The particular method of obtaining this pair of pulses from one pulse uses a 50Ω miniature fast pulse transformer (Vari-L Co., Inc.) connected to the 50Ω anode output of an RCA 8575 PM as shown in Figure A-2. Such a device will produce two identical, conjugate, 180^{o} out-of-phase, unipolar pulses from one input pulse, i.e., opposite polarity, but exactly in time phase. These two opposite polarity pulses are then operated upon separately and subsequently recombined to interfere. The summing operation can be carried out in either of two methods: a simple resistor summing network or another two input, noninverting fast pulse transformer.

Either the first or the second operation (as shown in Figure A-2) can be chosen to suit the particular scintillator or PM characteristics. Such operations might be: RC differentiation, RC integration, delay, clipping, stretching and identity (no operation).

The particular pair of operations chosen for the fast organic liquids such as Nuclear Enterprises 213 or 222 were RC differentiation and identity, indicated schematically in Figure A-3. One pulse is RC differentiated with

a short time constant, thus producing a bipolar pulse. The other pulse, of opposite polarity, is added to interfere approximately and thereby cancel the first part of the RC differentiated bipolar pulse. Such a cancellation produces an extremely shape sensitive output without the use of any nonlinear devices. The unipolar output is finally integrated before it enters a preamplifier. Since this pulse is related to a differentiation, it is conveniently defined as the (dL/dt) pulse and is particularly dependent on particle type.

Simultaneously a pulse is taken from another dynode, integrated for several decay times, and then amplified. So this pulse is defined as the $\int L\,dt$ pulse and is related to particle energy.

The two pulses (dL/dt) and $\int L\,dt$ are plotted against each other on a two-parameter field to realize the particle separation. This display method is similar to that used by dE/dx x E detector systems.

The entire PSD circuit designed for space use weighs less than 20 grams and is less than 5 cm in diameter when mounted on a single printed circuit board. It has been used with the RCA 8575 PM operated at negative high voltage. A preliminary layout is shown in Figure A-4. There is no limitation to the size reduction possible, but since stray capacitance is important, optimization would be necessary with each redesign.

3. Results

Figure A-5 is a two-dimensional low-level contour display of (dL/dt) vs $\int L\,dt$ for the neutron and γ-ray spectra from an Am-Be source. The Co^{60} Compton-edge pulse height corresponds to an electron energy of 1.1 Mev or of recoil protons of about 3 Mev. For a relative comparison with the many PSD systems, we have plotted in Figure A-6 a one-dimensional section through a two-dimensional spectrum at the Co^{60} Compton edge (50% point). The relative separation of γ and n events is best described by the M value, defined by (Reid and Hummel, 1966):

$$M = \frac{\Delta}{\delta_1 + \delta_2} \text{ , where } \Delta = \text{peak-to-peak separation,}$$

and δ_1 and δ_2 are the full widths at half maximum for the two peaks. For the data shown, M = 3.1.

We find that M values of 2 can be obtained down to proton energies of about 1 Mev. On the other hand, the upper limit can be extended to greater than 15 Mev with no apparent decrease in M. Moreover, the actual dynamic range is limited, not by the PSD itself, but by the characteristics of the amplifiers and pulse height analyzers following the PSD.

The test results from exposing the actual balloon flight unit to the 14 Mev monoenergetic output from the (d,t) reaction and to a Co^{60}, γ-ray source simultaneously

are shown in Figure A-7. The neutron energy range is 1 to 15 Mev and with a gain change can be increased to 30 Mev. Contours of full width at half maximum (FWHM) are plotted. The co-ordinate system is nonlinear to make optimum use of the pulse height analyzer range, assuming that the neutron differential energy spectrum at the top of the atmosphere can be crudely represented by K/E.

Two methods of in-flight calibration (IFC), both of which used alpha particle sources, were tried. These were designed about the concept of a 4π-enclosing, anti-coincidence, charged particle shield (St. Onge and Lockwood, 1967). This allows the inner, enclosed NE213 detector to "observe" only neutral radiation. Since external alpha particles would normally be excluded, the α-particle region of the two-parameter display can be conveniently used to display the output from an internal α-particle IFC.

The first method involved a radioactive alpha-emitting salt of Am^{241} completely soluble in NE213 and yet not detrimental to the PSD property of the scintillator (New England Nuclear Corp.). Although this approach was successful, it was not useful in this application because the light output obtained by alpha particle excitation of the organic scintillator was too small relative to neutron excitation in the energy range of interest.

The second IFC method used a small chip of NaI (Tl) light pulser (Harshaw Chemical Corp.) doped with Am^{241} (~4 mm diameter x 4 mm long). The pulse-shape separation with such a technique is exceptional because the much slower decay time of NaI(Tl) is easily discriminated from the fast organic (NE213) decays, i.e., the PSD system is operating as a phoswich (Wilkinson, 1952).

The pulse heights from the scintillator for the IFC can be adjusted by changing the size of the exit aperture on the crystal face of the miniature light pulser. The allocation of PHA area to the pertinent energy region of interest can be optimized, yet an α-IFC peak can be retained in the adjacent region. The output from such an IFC is shown in the upper right-hand portion of the dL/dt vs $\int L\,dt$ plot in Figure A-7. Improved energy resolution in the IFC can be obtained by using a stronger source. In this flight unit the telemetry system limited the counting rate of the IFC source to ~4 sec^{-1}.

4. Discussion

Although this method has the obvious disadvantage of requiring a two-parameter PHA, one can obtain excellent n-γ separation (M~3) over a wide dynamic range ($1 < E_n < 30$ Mev) at relatively high count rates (> 5 x 10^4 sec^{-1}). No effort was made to go to neutron energies lower than one Mev, nor has the upper limit been explored. No adjustment of the PSD is needed for changes in any of

PSD liquid scintillators, or particle energy.

In conclusion, this PSD system has the advantage of simplicity, passiveness and miniaturization. It operates over a wide dynamic range with high resolution and makes possible multiple particle pulse-shape discrimination.

APPENDIX C

THERMAL RADIATION CALCULATION FOR THE FLIGHT PACKAGE

Preflight calculations (Mehltretter, 1968) were made to determine the significant, physically-adjustable parameters necessary to obtain a desirable internal temperature for the neutron detector contained in a box 0.54 x 0.54 x 0.69 m.

The purpose of such calculations was to determine the necessary color of paint to be applied to the exterior surface of the package so that during the balloon flight the inner detector would be at a temperature near 20°C. The choice of the color affects the emissivity (ε) and the absorptivity (α). After several series of iterative calculations similar to the final one shown, it was determined that a particular type of flat white paint would maintain the temperature at the optimum 20°C. Another variable also determined by the following series of calculations was the required thickness of foam insulation to surround the detector. For the calculations shown we merely used the values for these variables deduced from a previous series of iterative calculations. These final calculations yielded the optimum conditions.

The following approach was taken in these calculations. First, the diffusion approximation was used to calculate the temperature difference between the center of the detector and the outer surface at equilibrium. Second, the minimum time

taken to reach equilibrium was calculated from specific heat considerations. Third, the outer surface temperature was determined from the conservation of energy. Finally, the inner detector temperature was calculated from the combined results.

The diffusion approximation was used to calculate the inner to outer temperature difference. For the cubic package we can write $R = K\ A\ dT/dX$, where R = rate of power input to package to operate internal electronics system, K = thermal conductivity, A = transverse area of package, dT = inner to outer temperature difference, and dX = thickness of thermal barrier. After rearranging and integrating over both temperature and thickness, the temperature difference is given by $T = RX/KA$. For the package, R = 4.25 watts = 14.5 B.T.U./hour, X = 6 inch (average), K = 0.3 B.T.U. inch $hour^{-1}$ ft^{-2} $F°^{-1}$, and A = 4.4 ft^2. If we substitute these dimensions and physical constants for the package into this expression, we find that T = 66 F° = 37 C°.

The time to reach equilibrium can be estimated provided that equilibrium is reached within the flight time (~11 hours). Although we know that the mass of the detector is 47 pounds (2.1, 10^4 gm), we can only estimate the average specific heat of this composite of materials as $\bar{c} \simeq 0.2$ cal gm^{-1} $C°^{-1}$ ($\pm$ 20%). Such an approximation initially disregards the thermal radiation loss. Putting $\Delta t/\Delta T = M\ \bar{c}/R$ where Δt = time to reach equilibrium, R = power input (4.25 watts), M = total mass of materials (2.1, 10^4 gm), $\bar{c}$ = average specific

heat (0.2 cal gm^{-1} $C°^{-1}$), and ΔT = estimated temperature change. Thus, the minimum time to reach equilibrium is approximately 69 hrs $C°^{-1}$.

Since the flight time (~11 hours) is much shorter than this equilibrium time, we expect that any temperature changes will be slow and slight. But, of course, this was deduced by assuming no internal power loss through surface radiation. Therefore, the actual time to reach equilibrium would be longer, which emphasizes that the package temperature cannot change appreciably during the flight time. However, since it is possible to have a heat flow into the system from the solar-heated exterior surfaces, we must calculate the exterior surface temperature from radiant energy considerations.

The conservation of energy was used to calculate the exterior surface temperature of the detector. The energy rate to the surface must equal the radiant losses as given by Stefan's law.

$$E_i + E_\odot + E_E = \sigma T^4 A_{(total)}$$

where E_i = internal power delivered to outer surface, $E_\odot$ = absorbed solar power, and E_E = absorbed albedo power. As a first approximation, we will neglect E_i in comparison with $E_\odot$ and E_E. This will be justified later. Approximating the package to a cube with a total surface area of 6A, where A is the area of one surface, we can write: $(\alpha_\odot/\varepsilon)$ (2A) $J_\odot$ + (α_E/ε) (3A) $J_E = \sigma T^4$ (6A), where $J_\odot = 13.10^{-2}$ watt cm^{-2} (solar constant), $J_E = 2.4\ 10^{-2}$ watt cm^{-2}, and $\sigma = 5.67\ 10^{-12}$

watt cm^{-2} $°C^{-4}$. The choice of white paint gives: $\alpha_{\odot}$ = 0.3, α_E = 0.9, and ε = 0.9. Thus, (σT^4) = 2.65 10^{-2} watt cm^{-2}, which gives T (external) = -18°C. Thus, the exterior surface of the package will have a temperature of ~ -18°C. However, we must first justify the assumption of neglecting E_i with respect to the $E_{\odot}$ and E_E terms. $E_i/6$ (A) = 4.25 watts/ 2 10^{+4} cm^{+2} ~ 2.1 10^{-4} watt cm^{-2}. Since this is less than 1% of the other two terms, we can properly neglect it.

In the beginning of this appendix we calculated the temperature difference between the inner and outer surface to be ~ 37C°. We can now determine the equilibrium inner temperature by combining the results of all the above calculations. The inner equilibrium temperature will be +19°C and the time to reach equilibrium at least 69 hours/C°. Since this temperature is quite suitable for the instrument, we began the balloon flight preparations from Texas by operating the detector within an environmental chamber set to maintain a temperature of 19°C.

The temperature extremes of the actual balloon flight for this detector were 21.4 $\pm$ 0.9°C for 11 hours. Thus, the calculated temperature predictions were in good agreement with the actual data.

APPENDIX D

CALCULATIONS OF LOCALLY PRODUCED NEUTRONS

Since high-energy cosmic rays interact with the mass of the flight system to produce neutrons, it is necessary to determine the relative importance of this contaminant (Trainor and Lockwood, 1964; Wilson, 1965). In order to minimize the effect of local production, the system was designed as two separate packages. The detector package was flown 2.76 m above the more massive electronics and battery package. Hence, the following calculations are made in two parts: the neutron production from the massive lower electronics and battery package as measured by the upper neutron detector and the neutron production of the upper package as measured by the enclosed neutron detector. The evaporation neutrons produced are assumed to be isotropically emitted and to have an energy range of from 1 to 10 Mev. This production neutron flux will be compared to the albedo neutron flux over their common energy range at the Pfotzer maximum.

1. Production in Lower Package

The rate of neutron production by the primary cosmic-ray flux is given by (Boella et al., 1965): $n = 2\pi \Phi_p \bar{\lambda}^{-1} \bar{\nu}$ neutrons sec^{-1} gm^{-1}, where n = number of neutrons per gram per second produced, Φ_p = primary flux of particles cm^{-2} sec^{-1} $ster^{-1}$, $\bar{\nu}$ = average multiplicity number of neutrons

produced per interaction, $\bar{\lambda}$ = average interaction length in gm cm^{-2}. This is an approximate expression, valid only if $\bar{\lambda}$ is large compared to the thickness of material in grams per square centimeter. Since we neglect any subsequent absorption of these locally produced neutrons, this estimate will be a worst case consideration.

The mass of air which the balloon displaces will be considered as a relative void. This relative void is equal to the local mass of the detection system. We will consider the balloon as a relatively deficient secondary production source and the detector system as a surplus production source. Since the number of neutrons per second per gram of producer changes less than a factor of two for these two different materials, we can easily estimate their relative contributions. Each producer will contribute in proportion to the solid angle subtended by the detector as seen from the mass centroid of the respective producer. However, since the balloon is at least 50 times more distant from the detector than the major mass of the detector system, the relative decrease in the neutron flux from the balloon void is less than 10^{-3} of the increase from the production due to the mass of the detector materials. Therefore, we need only consider the contamination from local production due to the detection system.

We will use the results of a similar calculation by Boella et al. (1965) for Φ_p, $\bar{\lambda}$, and $\bar{\nu}$. They found n = 8 x 10^{-3} neutrons sec^{-1} gm^{-1} for aluminum and n = 14 x 10^{-3} neu-

trons sec^{-1} gm^{-1} for nickel-cadmium at a geomagnetic cutoff of 4.6 Gv at solar minimum. Although the present flight was made at ~4.8 Gv and near solar maximum, the results are probably reliable to within 20 percent.

The production flux superimposed upon the albedo flux will be: $\Phi(\text{production}) = \sum_{(Al,\ Ni\text{-}Cd)} n\ M\ A^{-1}\ (\Omega/4\pi)$ where Φ = locally produced neutron flux at detector, neutron sec^{-1} cm^{-2}, M = mass of producer (4.5×10^4 gm-Al, 9.8×10^4 gm - Ni-Cd), A = projected area of detector (25.4 cm^{-2}), Ω = solid angle subtended by detector $\sim(A/R^2)$, R = separation in meters (m) of detector and mass (Al-3.48m, Ni-Cd-4.17m), Σ = summed over both aluminum and nickel-cadmium.

This results in a contaminating neutron flux of $\sim 0.7 \times 10^{-3}$ neutrons sec^{-1} cm^{-2} from the lower package. However, since the neutron flux in the same energy region is in the order of several neutrons sec^{-1} cm^{-2} (Haymes, 1964), the local neutron production from the lower package is less than a 0.1 percent correction.

2. Production in Upper Package

The upper package encloses the neutron detector with a polyurethane foam thermal covering and a perforated aluminum frame located outside the active charged-particle shield. The foam insulation ($\sim 5.5 \times 10^3$ gm) is located at an average distance of 23 cm from the inner 6.5 cm x 6.54 cm diameter neutron detector cell. The aluminum frame ($\sim 2.5 \times 10^3$ gm) is at a radius of 30 cm from the inner detector. Therefore, the pro-

duction count rate is $\Phi = \Sigma_{(\text{foam, frame})}\ \Phi = 0.8 \times 10^{-3}$ (foam) + 1.6×10^{-3} (frame) neutrons $\text{sec}^{-1}\ \text{cm}^{-2}$, where $\Phi = 2.4 \times 10^{-3}$ neutrons $\text{sec}^{-1}\ \text{cm}^{-2}$.

The National Center for Atmospheric Research (NCAR) balloon launch group also added a ballast and telemetry package (7×10^{4} gm @ 4.3 m) below the entire system. The added neutron flux that this will produce is 0.4×10^{-3} neutrons $\text{sec}^{-1}\ \text{cm}^{-2}$.

The total neutron production from the entire system (3.5×10^{-3} neutrons $\text{sec}^{-1}\ \text{cm}^{-2}$) is 0.1 percent of the neutron flux. Thus, we feel justified in neglecting any significant contribution from both the system production and the relative void of the balloon.

APPENDIX E

THE NEUTRON SPECTRUM UNFOLDING PROCEDURE

The unfolding process as discussed in Chapter IV, Section 3, can be broken down into four operations. First, the conversion from counts per logarithmic flight channel to counts per linear TMC channel. Second, the subsequent conversion from counts per TMC channel to the number of recoil protons per Mev of energy. Third, the evaluation of the derivative of the smoothed proton curve as a function of energy. Fourth, the evaluation of the response kernel as a function of energy.

We converted from counts per $\int Ldt$ flight channel (Figure 24c) to counts per TMC channel with a plot of flight channel versus TMC channel number, Figure 17. From this curve we obtained the beginning and end points of each flight channel in terms of TMC channel number, as well as the width of each channel in terms of TMC channels. The channel widths were then plotted versus flight channel number, Figure A-8, and a straight line drawn through these points. From this curve we obtained a smooth set of channel widths. The counts per flight channel were divided by this channel width to obtain the counts per flight channel in terms of counts per TMC channel.

The second conversion is almost identical to the first, so we need only discuss the difference. We begin

this operation with a set of calibration curves (counts per TMC channel versus TMC channel number) for Na^{22}, AmBe, Th^{228}, and the (D,T) reaction. With the use of Figure 16 we converted the beginning and end points from TMC channels into their equivalent Na^{22} light units. We converted from the channels in Na^{22} light units to energy, obtained the channel widths in terms of energy, plotted this versus light units, and from this curve (Figure A-9) obtained the number of recoil protons per Mev. This number was multiplied by a factor of 1.42 to scale the spectrum to the Pfotzer maximum count rate as shown in Figure 28a. Also shown in Figure 28a is the absolute Pfotzer maximum spectrum, protons/cm^2-sec-Mev. This was obtained by dividing by the isotropic area, A_i (total surface area/4) and the total time of accumulation (49 x 60 sec).

The number of counts per flight channel was smoothed using the three point sliding average relation:

$$\bar{N}_i = 1/2 \ (N_i + 1/2 \ (N_{i-1} + N_{i+1}) \ )$$

where N_i = number of recoil protons per Mev in the i^{th} channel and $\bar{N}_i$ = smoothed value for i^{th} channel. The smooth recoil-proton energy spectrum obtained from Figure 28a after the application of the above relation is given in Figure 28b.

The third step involved the evaluation of the deviative d/dE (dNp/dE) as a function of energy. This was evaluated from Figure 28b and the slope is shown in Figure

A-11.

The final and fourth step was the solution for the neutron spectrum (dNn/dE) as a function of energy (E) by the use of the following relation:

$$dN_n/dE = -\left(\frac{\varepsilon}{n_H \sigma_H L}\right) d/dE \left(dN_p/dE\right) F(E)^{-1} f(a,L)^{-1}$$

where $a(E) = (n_C\sigma_C + n_H\sigma_H)$ is the total effective cross-section, L is the length of the scintillator (4.60 cm), A_i is the isotropic area (total area/4) = 25.4 cm^2). F(E) is a small correction factor for second scattering and wall effects. f(a,L) = (1 - exp(-aL))/aL is a small correction factor for the neutron flux attenuation within the scintillator. The strength of the correction factor F for second scattering and wall effects is given in Figure A-10. The resulting neutron energy spectrum at Pfotzer maximum is shown in Figure 29.

APPENDIX F

THE CONTRIBUTION OF PROTONS FROM $C^{12}(n,p)$ REACTIONS

There are two carbon interactions which produce secondary protons, $C^{12}(n,p)\ B^{12}$ and $C^{12}(n,n'p)\ B^{11}$. These reactions must be considered since the PSD would recognize the resultant protons while the unfolding method of Appendix E considered only secondary protons from n(H,P) n'. Madey (1968) concluded that the $C^{12}(n,p)\ B^{12}$ cross section is the dominating reaction from 16 Mev < E_n < 30 Mev. Another argument, outside of cross-sectional considerations, can be based upon considering these two reactions for the two different incident neutron energies which would produce equal energies for the secondary protons. Since the $C^{12}(n,n'p)\ B^{11}$ channel produces three nucleons, two of which are mass one, we expect that most of the available energy will be distributed between the proton and the neutron. Therefore, the $C^{12}(n,n'p)\ B^{11}$ reaction will produce lower energy protons than the $C^{12}(n,p)\ B^{12}$ reaction for equal incident neutron energies. We conclude that the $C^{12}(n,p)\ B^{12}$ reaction will produce more protons of higher energy than the $C^{12}(n,n'p)\ B^{11}$ reaction. Therefore, we must calculate the number of protons that are produced by carbon relative to the number of protons produced by hydrogen in the same proton energy intervals from $C^{12}(n,p)\ B^{12}$.

We will estimate the contamination ratio (R) of the

$C^{12}(n,p)\ B^{12}$ proton count rate to the H(n,p)n' proton count rate at equal proton energies. This is approximately proportional to the following:

$$R \simeq (dN_p/dE)_{n,C^{12}} / (dN_p/dE)_{n,H} \simeq$$

$$\simeq n_c \sigma_c(E_n)\, \phi(E_n) \,/\, n_H \sigma_H(E_p)\, \phi(E_p)$$

The numerator is the relative count rate of contaminating protons due to the atmospheric albedo neutron flux upon carbon in the NE213 scintillator by the $C^{12}(n,p)\ B^{12}$. The denominator is the corresponding rate due to H(n,p)n'. However, in order to assure that the two reactions will produce protons of the same energy, the incident neutron energy for the carbon reaction must be higher than that for the hydrogen reaction. The relation between these two energies can be calculated from a knowledge of the Q value for the carbon reaction. Kurz (1964) gives Q as -12.59 Mev. Halliday (1955) relates Q for the general reaction X(a,b)Y,

$$E_b^{1/2} = \frac{\left\{\cos\Theta\,(m_a m_b E_a)^{1/2} \pm \left\{m_a m_b \cos^2\Theta + (m_Y + m_b)[m_Y Q + (m_Y - m_a)E_a]\right\}^{1/2}\right\}}{(m_Y + m_b)}$$

The ratio of n_H/n_C for NE213 is 1.2. The carbon cross-section is taken from the work of Kurz (1964) and values for albedo flux are taken from Lingenfelter (1963). We must point

out that this method can only estimate this ratio (R) since the carbon reaction is really a multi-channel reaction. We will assume that the protons from carbon come out with all energies between zero and E_{max} with equal probabilities. This approximation is similar to the approximation used in the H(n,p)n' reaction.

The ratio (R) was calculated for three proton energies distributed over our measured energy range, 3.6 Mev, 11.1 Mev, and 20.2 Mev. The respective values for (R) were: 0.44%, 1.9%, and 3.1%.

The R value will be approximately equal to the error introduced in the unfolding process by neglecting the effects of carbon in producing protons. Since this error was found to be small (~<3%) with respect to the statistical errors in the experiment, we neglect it. However, we must point out that the ratio (R) increases with energy and that experiments at energies beyond 30 Mev the error will be significant (~15% at 50 Mev) and must be considered in the spectrum unfolding.

Zych (1968) experimentally found such a large effect for carbon at higher energies (12 - 100 Mev).

APPENDIX G

THE CONTRIBUTION OF ALPHA PARTICLES FROM $C^{12}(n,\alpha)$ REACTIONS

Since we measured the flux and energy spectrum due to neutral particles interacting with an organic to produce alpha particles, we will attempt a crude theoretical estimate of this effect. Kurz (1964) gives estimated cross sections for the two possible alpha particle producing reactions, $C^{12}(n,3\alpha)n'$ and $C^{12}(n,\alpha)\ Be^{9}$. The respective Q values, threshold energies (E_T) and maximum cross sections (σ(max)) are: -7.26 Mev, 7.9 Mev, 0.31 barns and -5.71 Mev, 6.2 Mev, 0.15 barns. Although the $C^{12}(n,3\alpha)n'$ maximum cross section is twice that of $C^{12}(n,\alpha)\ Be^{9}$, Kurz considers the former cross section to fall more rapidly with energy until at $E_n \gtrsim 80$ Mev, both are approximately 0.1 barns and constant.

The relative count rate of alpha particles to recoil protons of equal light outputs, i.e., equal $\int$Ldt channel numbers, can be crudely estimated from the following relation:

$$R(\alpha/p) \cong \frac{(dN_\alpha/dE)_{E_\alpha}}{(dN_p/dE)_{E_p}} = \frac{n_c \sigma_c (dN_n/dE)_{E_{n,\alpha}}}{n_H \sigma_H (dN_n/dE)_{E_{n,p}}}$$

where R(α/p) is the ratio of the alpha particles count rate to proton count rate at the same $\int$Ldt light outputs. $(dN_\alpha/dE)_{E_\alpha}$ and $(dN_p/dE)_{E_p}$ are the resultant alpha particle and recoil-proton spectra evaluated at specific energies, $E_\alpha \neq E_p$.

$(dEn/dE)_{E_{n\to\alpha}}$ is the neutron spectrum evaluated at the particular energy required to produce the correct alpha particle energy.

The relation between the light yields from both protons and alpha particles is taken from Verbinski (1968) and is given in Figure 11.

The relationship between the energy of the incident neutron and the resulting alpha particle's maximum energy is calculated from the same relation used in Appendix F from Halliday (1955).

In particular, from the relation of Halliday we find that a 30 Mev neutron will produce maximum alpha particle energy of 22 Mev. From the graph of Figure 11 we find that this 22 Mev alpha particle will produce 6.4 Na^{22} light units which is equivalent to that produced by a 13.5 Mev proton. Therefore, we must compare the count rate of 22 Mev alpha particles to the count rate of 13.5 Mev protons. However, the alpha particles are produced by 30 Mev neutrons, while the protons are produced by 13.5 Mev neutrons. Therefore:

$$R_{(\alpha/p)} = \frac{(dN_\alpha/dE)_{E_\alpha = 22\,Mev}}{(dN_p/dE)_{E_p = 13.5\,Mev}}$$

$$= \frac{1}{1.2}\,\frac{\sigma_c(E_n = 30\,Mev)\,(dN_n/dE)_{E=30\,Mev}}{\sigma_H(E_n = 13.5\,Mev)\,(dN_n/dE)_{E=13.5\,Mev}}$$

$$= 6 \pm 3\,10^{-2}\ \text{(alpha particles/protons)}$$

The carbon cross section was taken from the data of Kurz (1964) as 0.140 barns and the atmospheric neutron spectrum was taken from the work of Hess et al. (1961).

Since we have neglected the other C^{12} channel of $C^{12}(n,3\alpha)n'$, we expect that the above estimate of ~6% must be a minimum estimate for $R(\alpha/p)$. A similar calculation involved 27 Mev alpha particles from 35 Mev neutrons and 17 Mev protons from 17 Mev neutrons. This resulted in a ratio of $\approx (7 \pm 3)\ 10^{-2}$.

The average measured flight ratio R was found to be ~10% from Figure 12. Although this agreement is very good, we must point out that there are many sources of error involved. Two of the most important are σ(carbon) and (dNn/dE).

However, if the carbon cross section is better measured, we feel that this method of comparing the ratio of alpha particles to recoil protons can be used to derive the atmospheric neutron spectrum.

FIGURE CAPTIONS

Figure 1a. The cosmic-ray albedo-neutron decay model for the production of the inner-radiation zone (reproduced from Hess, 1968).

Figure 1b. The high-energy trapped proton energy spectrum in the inner zone (reproduced from Naugle and Kniffen, 1961).

Figure 2. The approximate vertical intensities of cosmic-ray secondary components as functions of atmospheric depth (the solid curves (μ,p,e) are reproduced from Rossi, 1952).

Figure 3. A comparison at high altitudes of three calculations of the neutron flux as a function of atmospheric depth with the experimental observations of Haymes (1964) (reproduced from Haymes, 1964).

Figure 4. Energy distribution of high-energy protons in the middle of the inner zone of the radiation belt. The solid curve is the theoretical spectrum expected from the cosmic-ray neutron albedo decay theory and the data are from Freden and White, 1960, (reproduced from Freden and White, 1960).

Figure 5. A comparison of cross sections for fast-neutron reactions used in detectors.

Figure 6. Light attenuation as a function of distance in plastic scintillators as seen with two types of cylindrical photocathode configurations, flat end and flat end with sides.

Figure 7. Charged-particle anticoincidence shield designs with hemispherical photocathodes.

Figure 8. Parallel sum and coincidence logic of the charged-particle shield system.

Figure 9. Data obtained with the PSD system of St. Onge and Lockwood (1968) showing particle separation for gamma rays, muons, and neutrons. The PSD system was inserted between the two components of a muon telescope with an AmBe neutron source near by. The upper diagram was obtained in coincidence with the μ-telescope, while the lower was measured in anticoincidence.

Figure 10. A detailed, composite enlargement of Figure 9.

Figure 11. Energy as a function of light output for gamma rays, protons, alphas, and carbon nuclei in NE213 (Verbinski et al., 1968). Our four calibration points (Na^{22}, Th^{228}, AmBe

and D,T) are also shown for gamma rays and neutrons.

Figure 12. Two-parameter ($\int$Ldt x dL/dt) flight data taken from 16.4 Kft, 541 mb to 63.0 Kft, 62 mb.

Figure 13a. Block diagram of the complete logic system used in the balloon flight.

Figure 13b. Two-parameter ($\int$Ldt x dL/dt) error-detecting transmission scheme.

Figure 14a. Na^{22} (1.28 Mev gamma ray) $\int$Ldt calibration

Figure 14b. Th^{228} (2.615 Mev gamma ray) $\int$Ldt calibration

Figure 15a. AmBe (2.43 Mev gamma ray) $\int$Ldt calibration

Figure 15b. (D,T) (14.1 Mev neutron) dL/dt and $\int$Ldt calibration.

Figure 16. The $\int$Ldt light output as a function of linear TMC channel number for the scintillator, preamp, amplifier, and linear routing logic system. These four data points were obtained from combining Figures 11 (Verbinski et al., 1968), 14, and 15. This was used to correct for nonlinearities in the integrated system.

Figure 17. The linear TMC channel number as a function of flight channel number for the dL/dt and $\int$Ldt pulses. The flight PHA behavior is logarithmic for both parameters, dL/dt and $\int$Ldt.

Figure 18. The count rate as a function of atmospheric depth for the three groups of scaled data recorded during the flight. None of these include the IFC count rate which was 3.4 counts/sec.

Figure 19. The $\int$Ldt x dL/dt uncorrected data recorded during the flight from 40.0 Kft. to 63 Kft. The data located in the upper left-hand corner is the continuation from the upper right-hand corner. The integrated light output $\int$Ldt is the horizontal axis.

Figure 20. The linear $\int$Ldt light pulse spectrum from the in-flight calibrator (IFC).

Figure 21. The map of the flight trajectory for the balloon which was launched Sept. 7, 1968, from Palestine, Texas, and impacted at Big Springs, Texas.

Figure 22. The assent pressure profile record of the balloon flight from launch to float altitude.

Figure 23. The $\int$Ldt x dL/dt uncorrected data recorded during the flight from 15.4 Kft to 40.0 Kft.

Figure 24a. The uncorrected $\int$Ldt flight recoil-proton pulse spectrum directly extracted from Figure 23.

Figure 24b. The $\int$Ldt recoil-proton pulse spectrum from Figure 19. Figures 24 a and b can be compared for spectrum differences with altitude.

Figure 24c. The sum of the data in Figures 24a and 24b. This is also the recoil-proton data of Figure 12.

Figure 25. The secondary alpha-particle pulse spectrum extracted from Figure 12.

Figure 26a. The uncorrected pulse spectrum directly extracted from Figure 23.

Figure 26b. The corresponding spectrum from Figure 19. Figures 26a and b can be compared for spectrum differences with altitude.

Figure 26c. The corresponding spectrum from Figure 19.

Figure 27. The IFC $\int$Ldt pulse spectrum taken during the assent of the balloon. The upper figure was taken from Figure 23 and the lower figure was taken from Figure 19. These IFC spectra cover all of the flight data used in the analysis.

Figure 28a. The recoil-proton spectrum calculated from Figure 24c and scaled to Pfotzer maximum.

Figure 28b. The proton spectrum of Figure 28a obtained after applying an averaging relation $\bar{N}_i = 1/2\ N_i + 1/4\ (N_{i+1} + N_{i-1})$.

Figure 29. The final neutron spectrum at Pfotzer maximum unfolded from Figure 28b.

Figure 30. The secondary alpha-particle spectrum unfolded from Figure 25 and scaled to Pfotzer maximum.

Figure 31a. The final Compton electron spectrum at Pfotzer maximum unfolded from Figure 26c.

Figure 31b. The smoothed Compton electron spectrum of Figure 31a after being averaged with the relation: $\bar{N}_i = 1/2\ N_i + 1/4\ (N_{i-1} + N_{i+1})$.

Figure 32. The amplitude and slope as a function of energy for the neutron spectrum at Pfotzer maximum. This was de-

rived from Figure 28b using the approximation: $dN_n/dE = B(E)E^{-\beta(E)}$.

Figure 33. The calculated equilibrium neutron flux versus energy at different atmospheric depths for geomagnetic latitude 44°. This figure is reproduced from Figure 1, p. 666 of Hess et al. (1961).

Figure 34. A comparison of three neutron spectrums at Pfotzer maximum (100 gm km^2) and the theoretical source spectrum. (Reproduced from Hess et al., 1961)

Figure 35. Response of a composite detector to neutrons and gamma rays of various energies: Curve A, 0.5 Mev electrons and 2 Mev neutrons; Curve B, 1 Mev electrons and 3.3 Mev neutrons; Curve C, 2 Mev electrons and 5.4 Mev neutrons; Curve D, 4 Mev electrons and 8.8 Mev neutrons. This figure is reproduced from p. 31, Figure 5C of Mendell, 1963.

APPENDIX FIGURES

Figure A-1. The transmission characteristics of the dome-type charged-particle shields (reproduced from St. Onge and Lockwood, 1968b).

Figure A-2. A schematic diagram of the PSD operations (reproduced from St. Onge and Lockwood, 1968a).

Figure A-3. The detailed PSD circuit diagram (reproduced from St. Onge and Lockwood, 1968b).

Figure A-4. The PSD mounted on printed circuit board using microstripe impedence matching techniques (reproduced from St. Onge and Lockwood, 1968b).

Figure A-5. A preliminary two-parameter (64 x 64) contour display of AmBe neutrons and gamma rays. The section denoted the $\int$Ldt Co^{60} Compton edge.

Figure A-6. The section of Figure A-5 taken at the $\int$Ldt value corresponding to the Compton edge of Co^{60}. The"M" value is ~3.1. The "window" widths on the $\int$Ldt section are 4 percent.

Figure A-7. A laboratory, preliminary two-parameter (64 x 64) contour display of Compton electrons, recoil protons and the IFC. The width of the dark bands are equal to one full width at half maximum (FWHM).

Figure A-8. The calibration data for the $\int$Ldt flight channel

widths in linear TMC units as a function of the flight channel number.

Figure A-9. The calibration data used to convert channel widths from Na^{22} light units to energy (Mev).

Figure A-10. The calculated correction factor (F) for second scattering and wall effects versus neutron energy.

Figure A-11. The slope (α) of the recoil proton spectrum of Figure 28b obtained from the approximate relation: $dNp/dE = A(E)\ E^{-\alpha(E)}$.

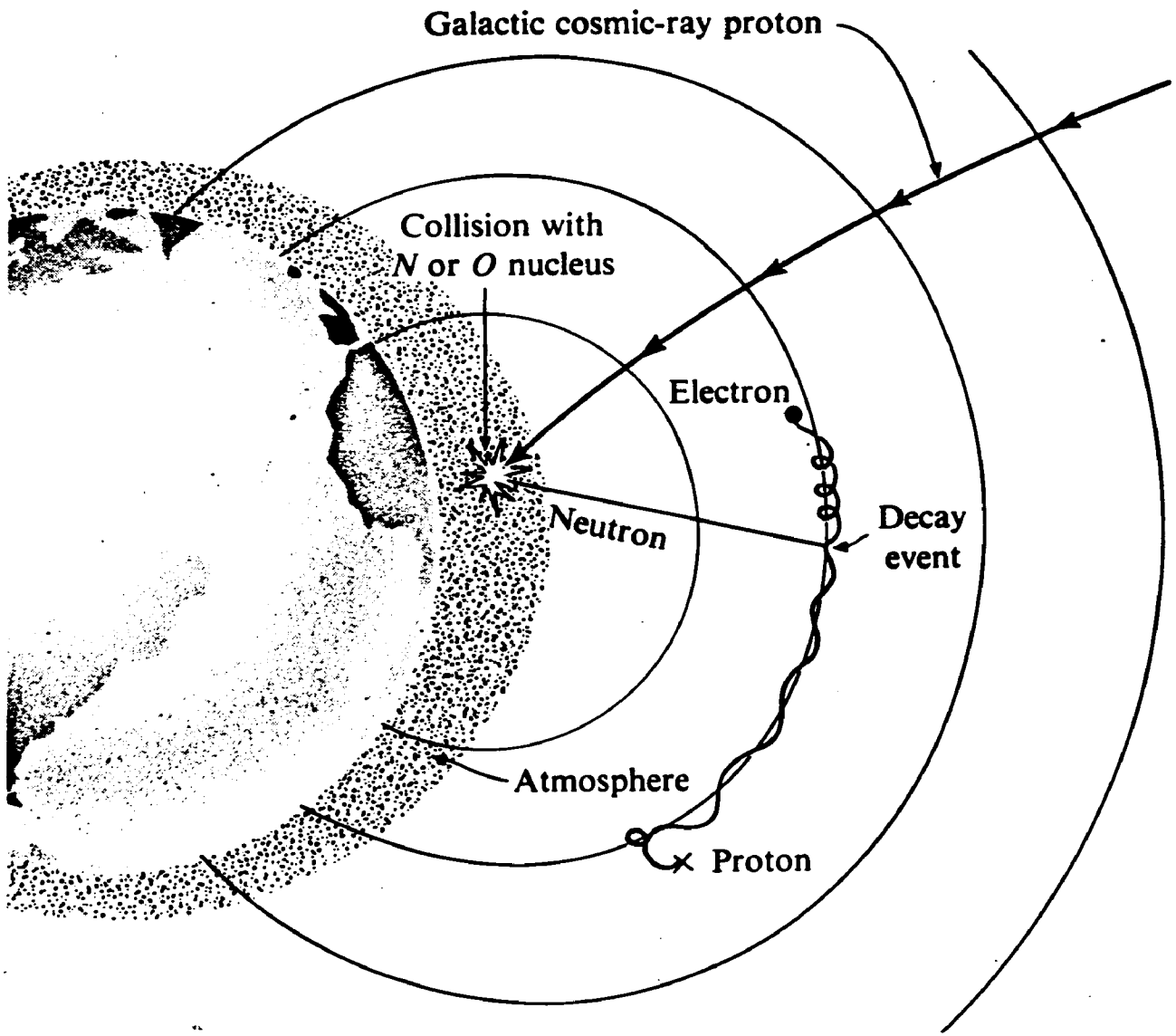
Galactic cosmic-ray proton
Collision with
N or O nucleus
Electron
Neutron
Decay
event
Atmosphere
Proton

Figure 1a

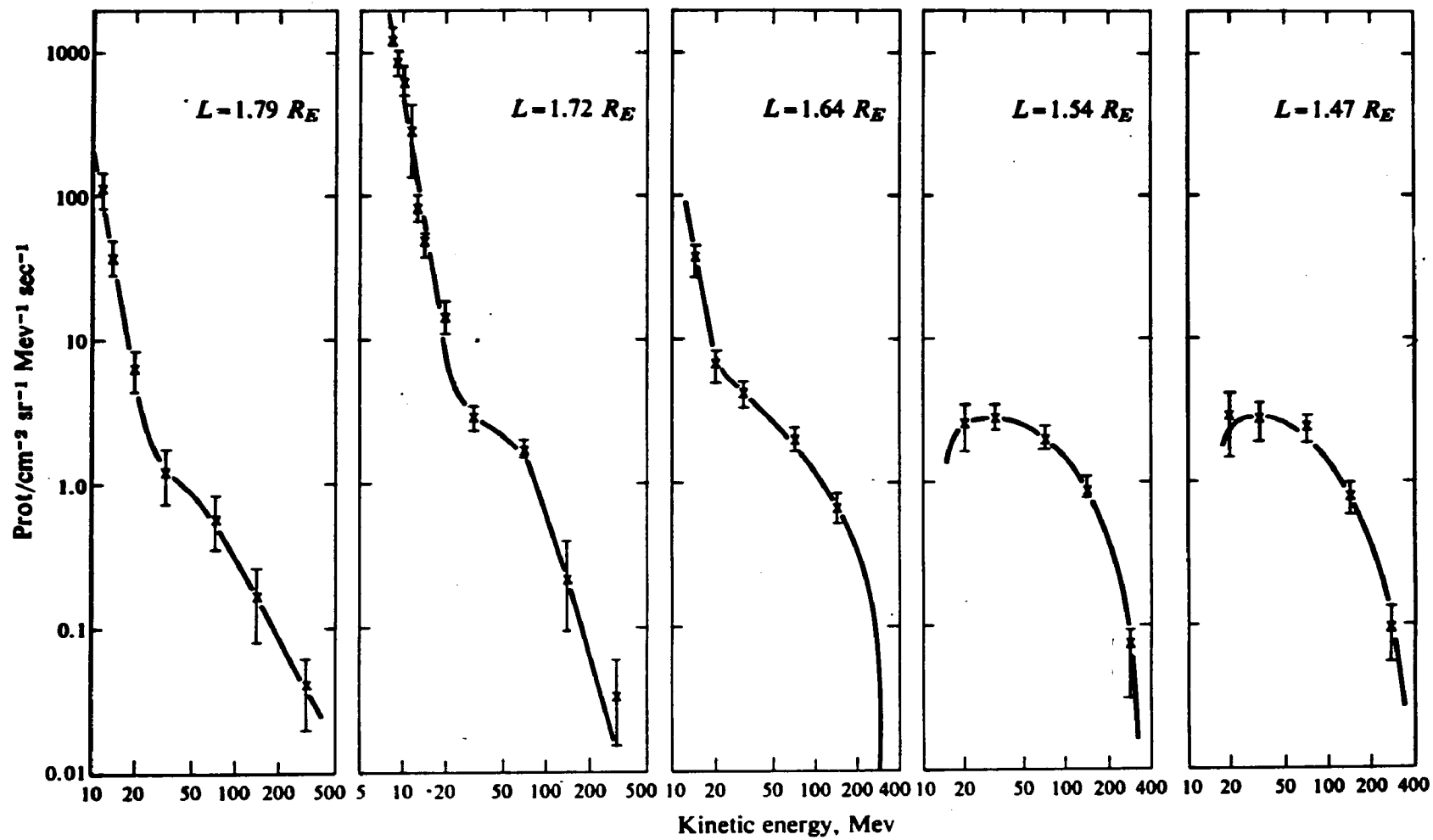
L = 1.79 R_E
L = 1.72 R_E
L = 1.64 R_E
L = 1.54 R_E
L = 1.47 R_E
Prot/cm⁻² sr⁻¹ Mev⁻¹ sec⁻¹
1000
100
10
1.0
0.1
0.01
10 20 50 100 200 500
5 10 20 50 100 200 500
10 20 50 100 200 400
10 20 50 100 200 400
10 20 50 100 200 400
Kinetic energy, Mev

Figure 1b

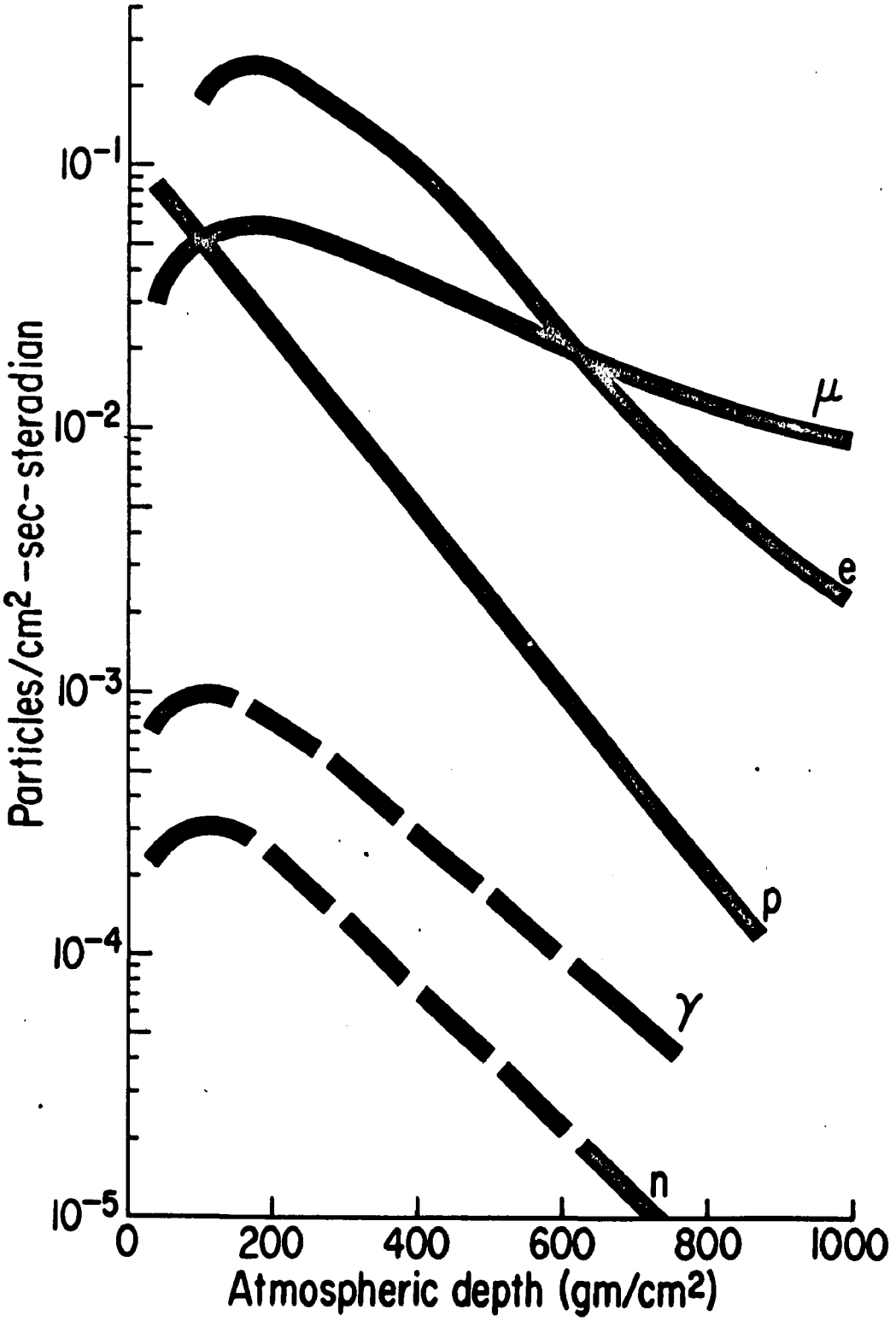
Particles/cm²-sec-steradian
10⁻¹
10⁻²
10⁻³
10⁻⁴
10⁻⁵
μ
e
p
γ
n
0
200
400
600
800
1000
Atmospheric depth (gm/cm²)

Figure 2

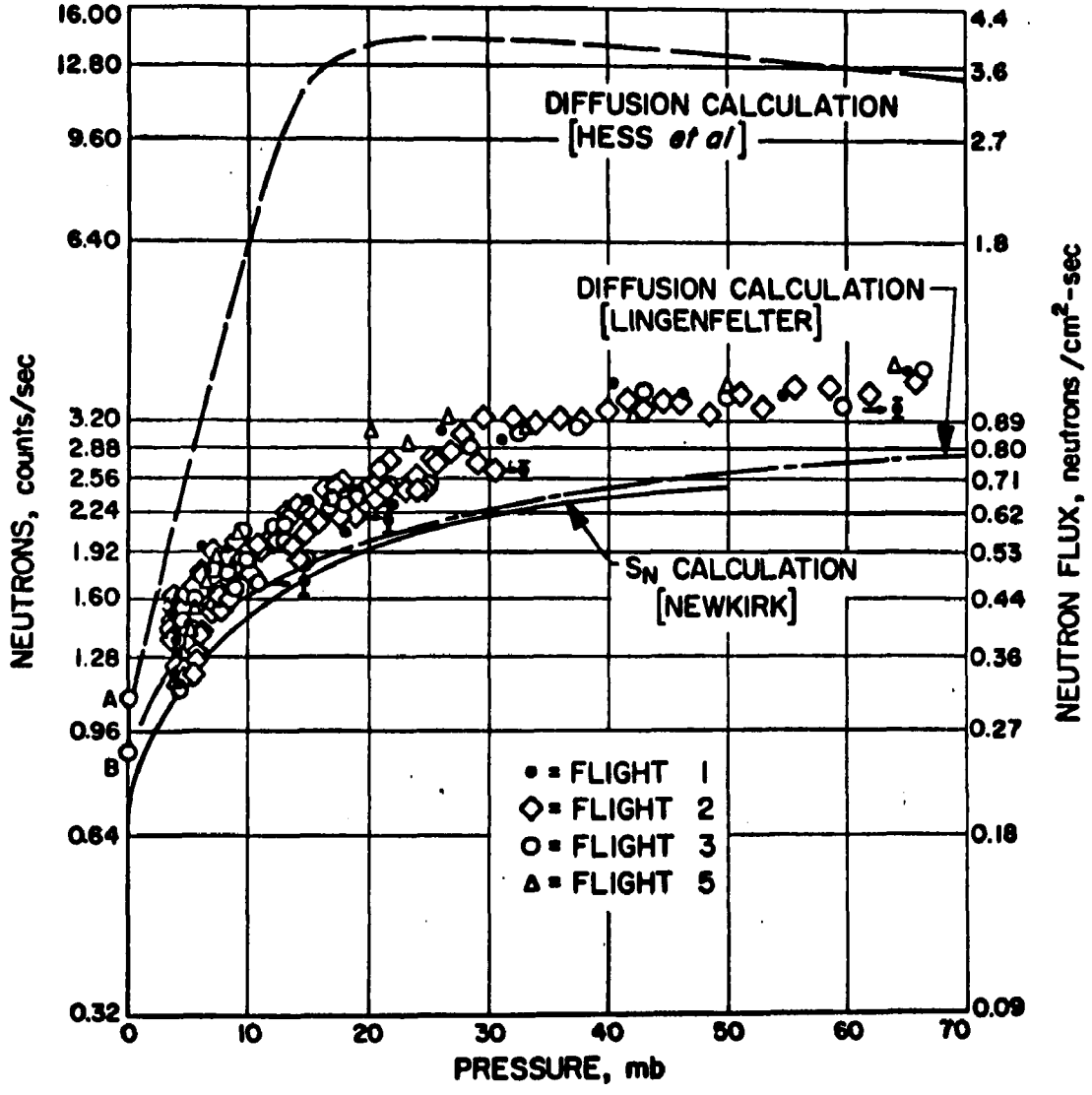
16.00
12.80
9.60
6.40
3.20
2.88
2.56
2.24
1.92
1.60
1.28
A
0.96
B
0.64
0.32
NEUTRONS, counts/sec
4.4
3.6
2.7
1.8
0.89
0.80
0.71
0.62
0.53
0.44
0.36
0.27
0.18
0.09
NEUTRON FLUX, neutrons/cm²-sec
DIFFUSION CALCULATION
[HESS et al]
DIFFUSION CALCULATION
[LINGENFELTER]
S_N CALCULATION
[NEWKIRK]
• = FLIGHT 1
◇ = FLIGHT 2
○ = FLIGHT 3
△ = FLIGHT 5
0
10
20
30
40
50
60
70
PRESSURE, mb

Figure 3

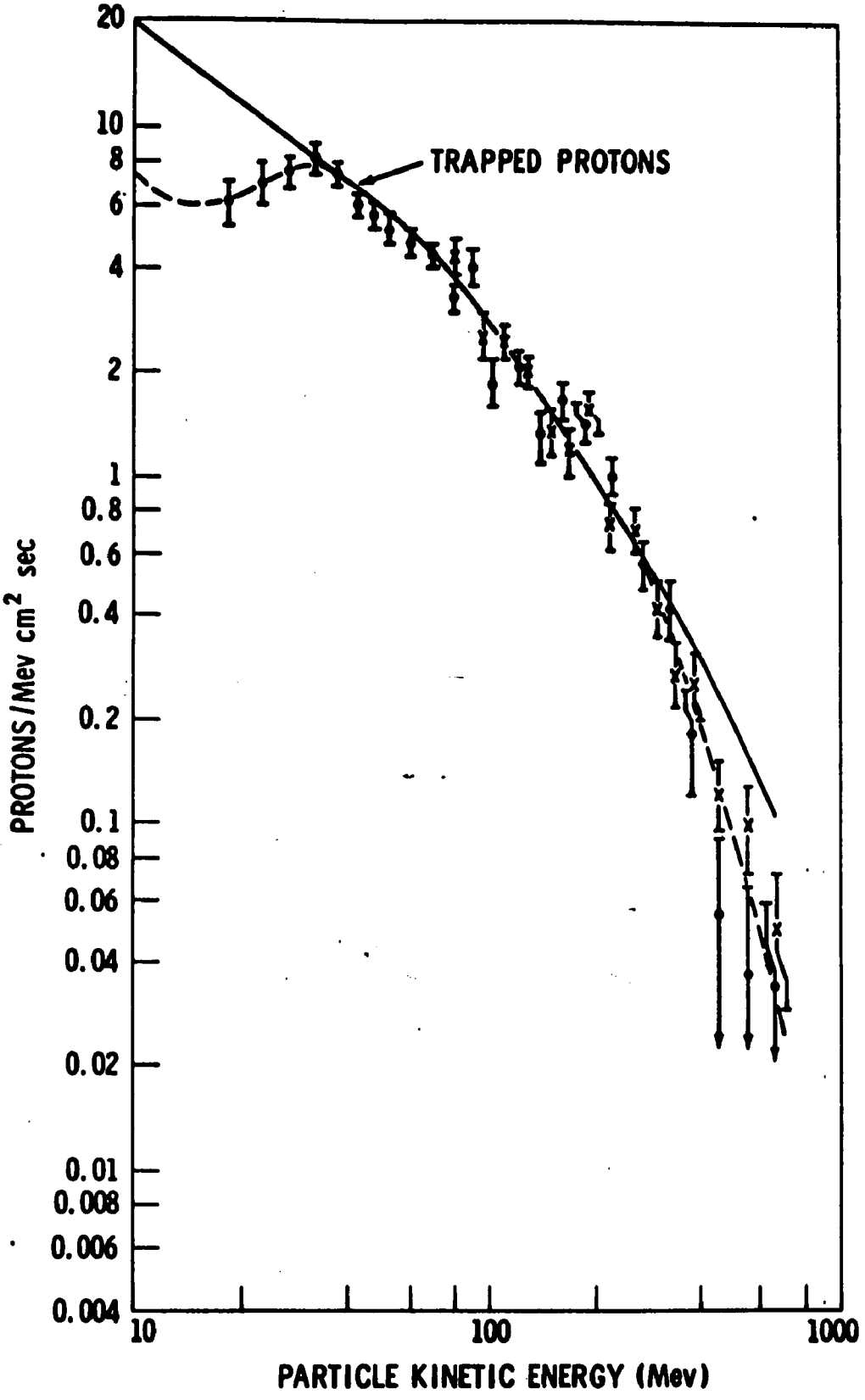
TRAPPED PROTONS
PROTONS/Mev cm^2 sec
PARTICLE KINETIC ENERGY (Mev)
20
10
8
6
4
2
1
0.8
0.6
0.4
0.2
0.1
0.08
0.06
0.04
0.02
0.01
0.008
0.006
0.004
10
100
1000

Figure 4

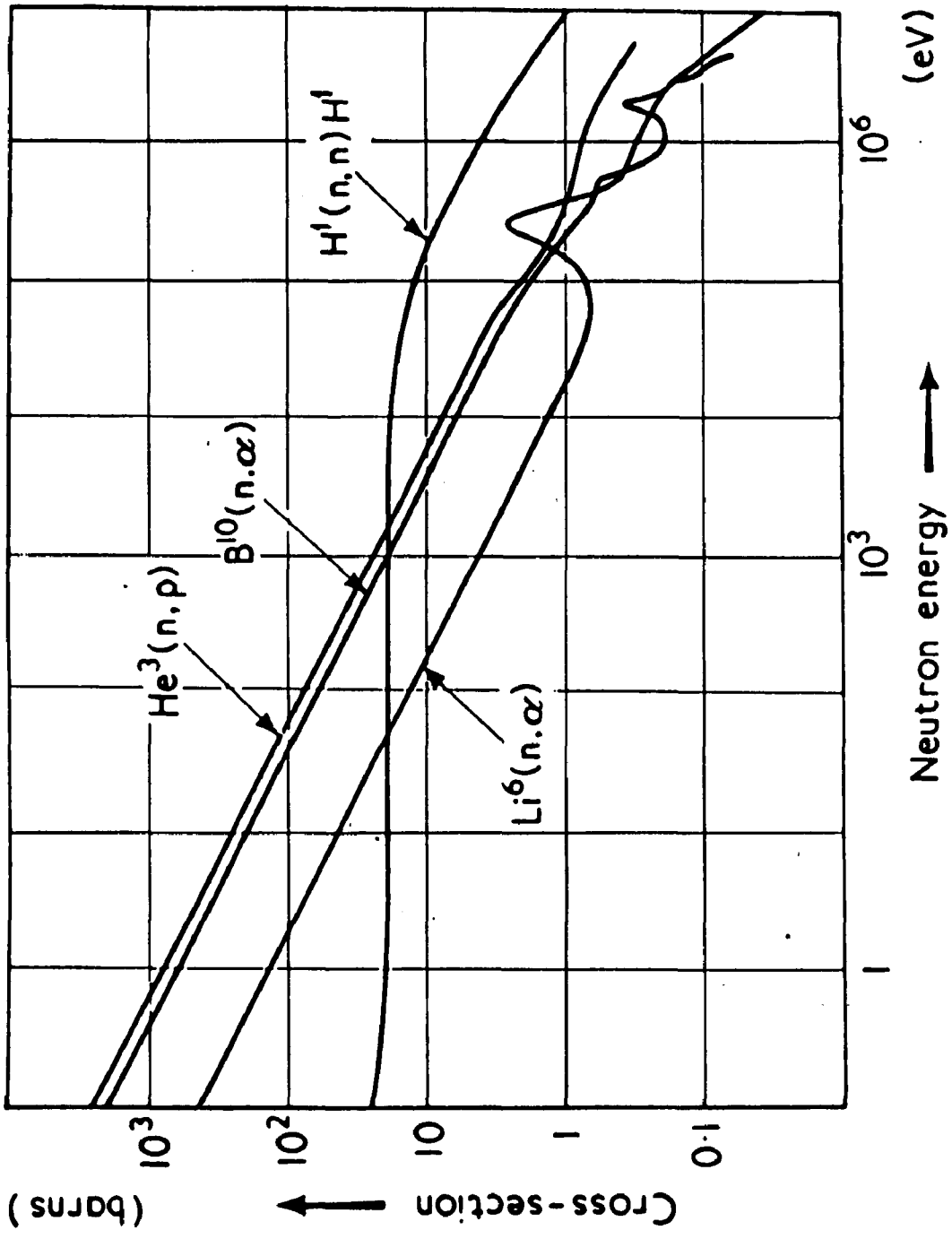
Cross-section
(barns)
10^3
10^2
10
1
0·1
Neutron energy
(eV)
10^6
10^3
1
$H^1(n,n)H^1$
$B^{10}(n,\alpha)$
$He^3(n,p)$
$Li^6(n,\alpha)$

Figure 5

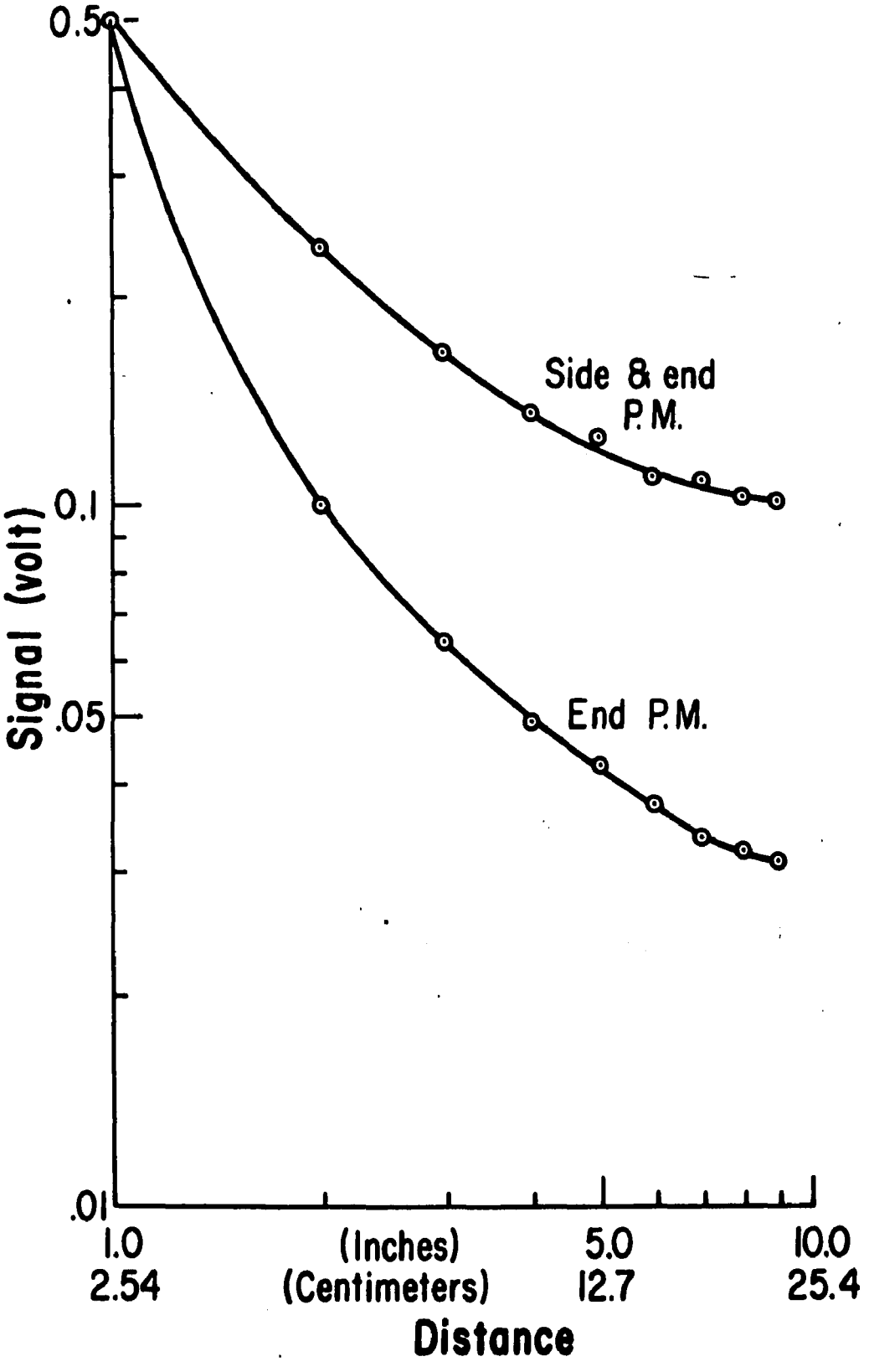
0.5
0.1
.05
.01
Signal (volt)
Side & end P.M.
End P.M.
1.0
2.54
(Inches)
(Centimeters)
5.0
12.7
10.0
25.4
Distance

Figure 6

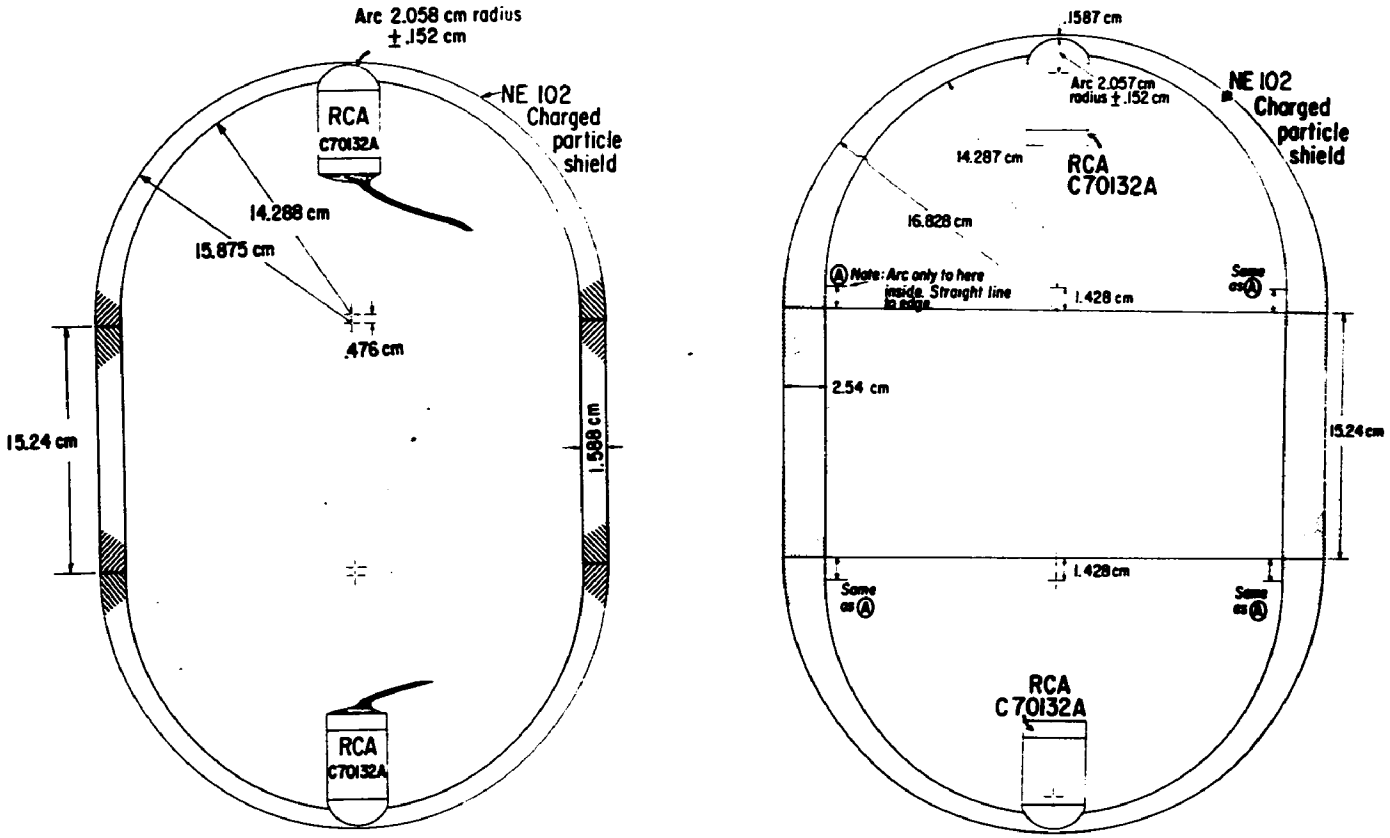
Arc 2.058 cm radius
±.152 cm
NE 102
Charged
particle
shield
RCA
C70132A
14.288 cm
15.875 cm
.476 cm
15.24 cm
1.588 cm
RCA
C70132A
.1587 cm
Arc 2.057 cm
radius ±.152 cm
NE 102
Charged
particle
shield
14.287 cm
RCA
C70132A
16.828 cm
Note: Arc only to here
inside. Straight line
to edge
Same
as A
1.428 cm
2.54 cm
15.24 cm
1.428 cm
Same
as A
Same
as A
RCA
C70132A

Figure 7

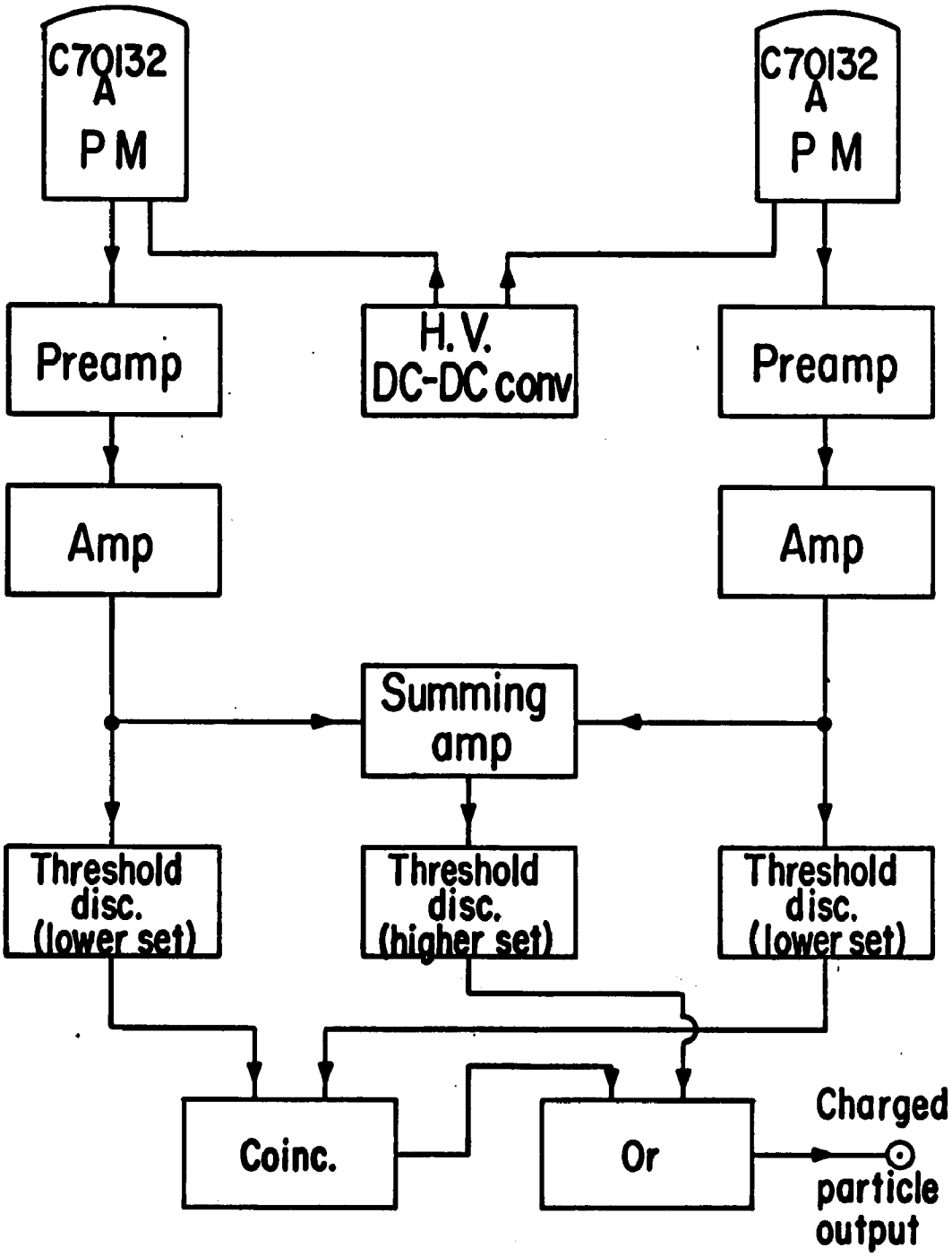

Charged particle shield system

Figure 8

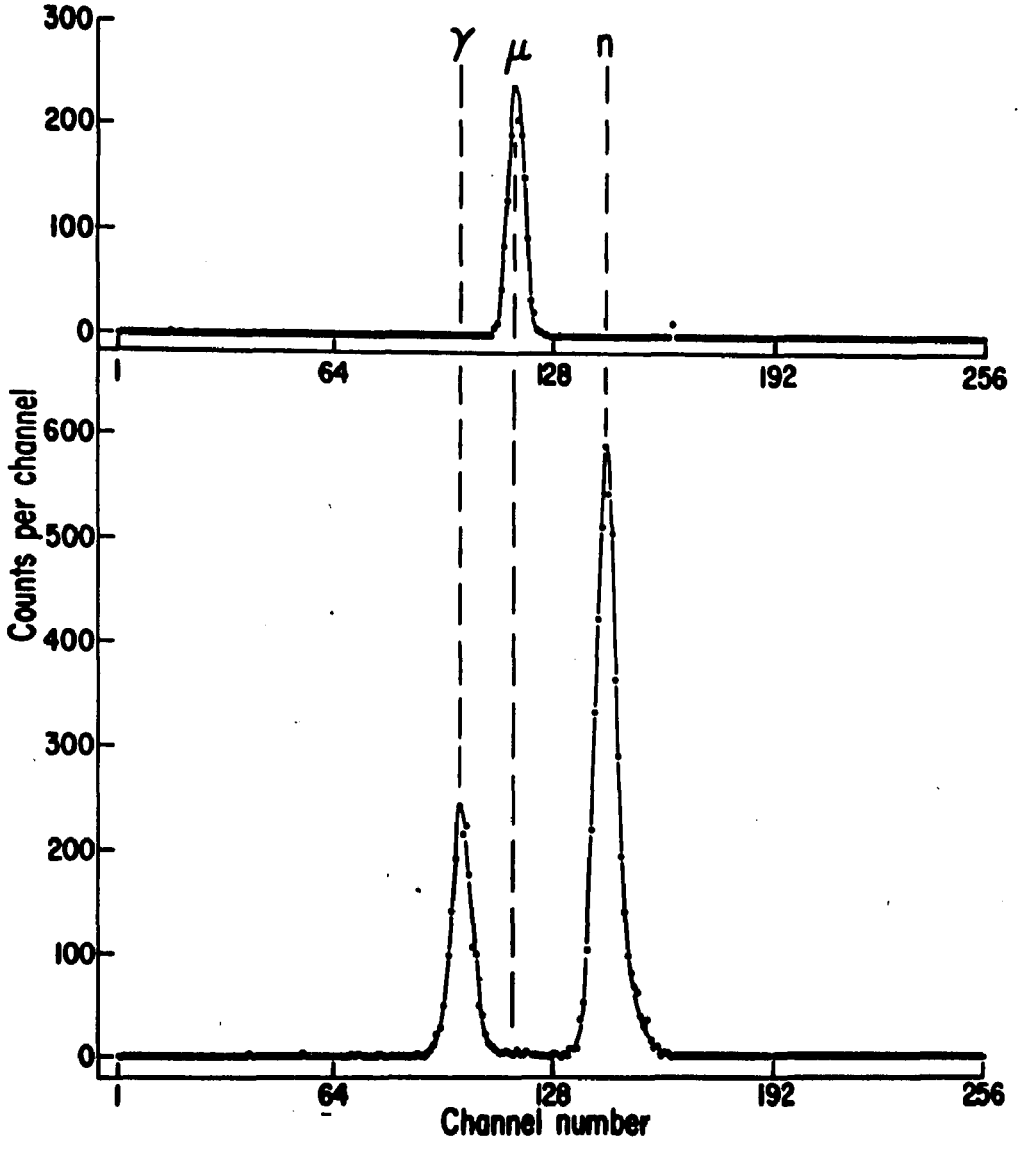
γ
μ
n
300
200
100
0
1
64
128
192
256
600
500
400
300
200
100
0
Counts per channel
Channel number

Figure 9

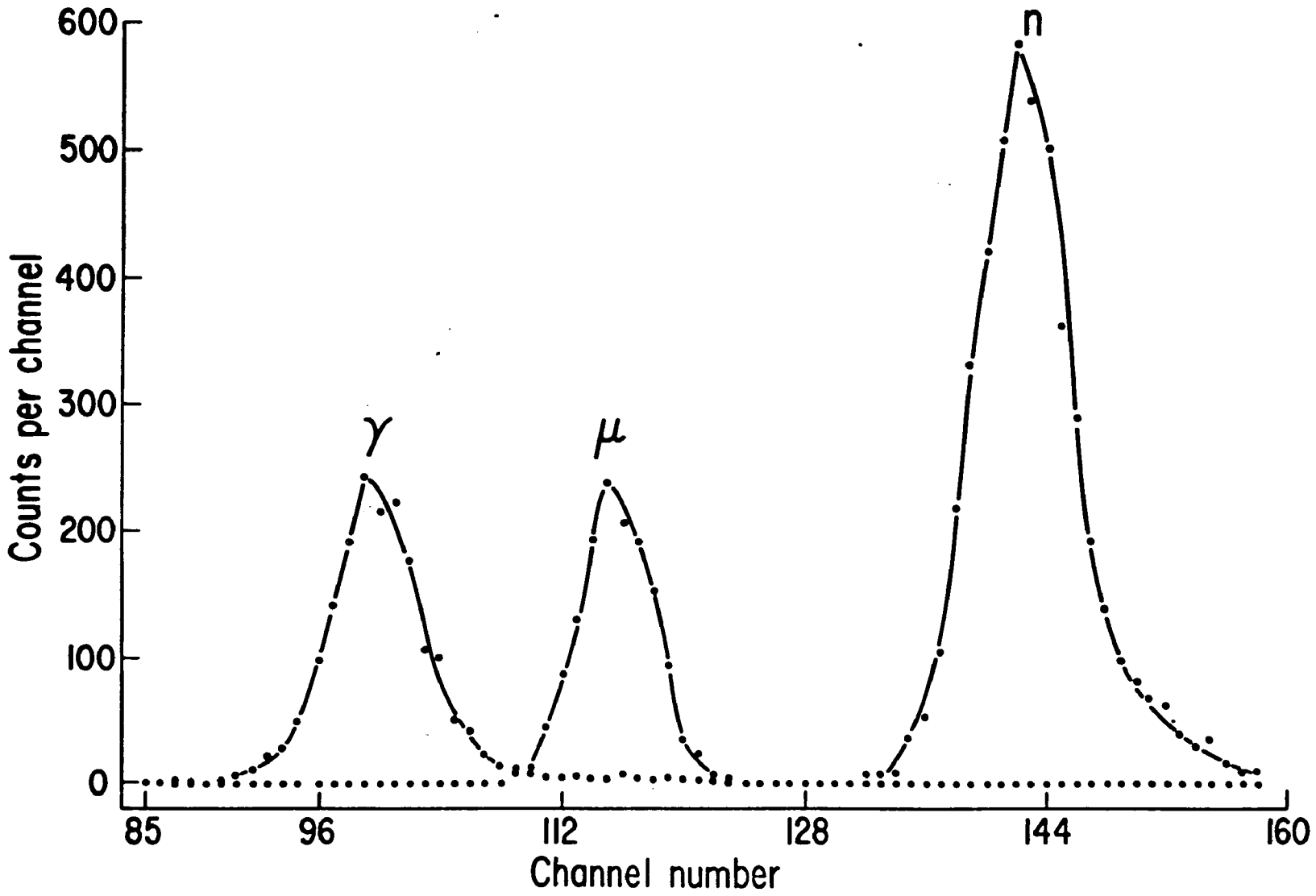
600
500
400
300
200
100
0
Counts per channel
γ
μ
n
85
96
112
128
144
160
Channel number

Figure 10

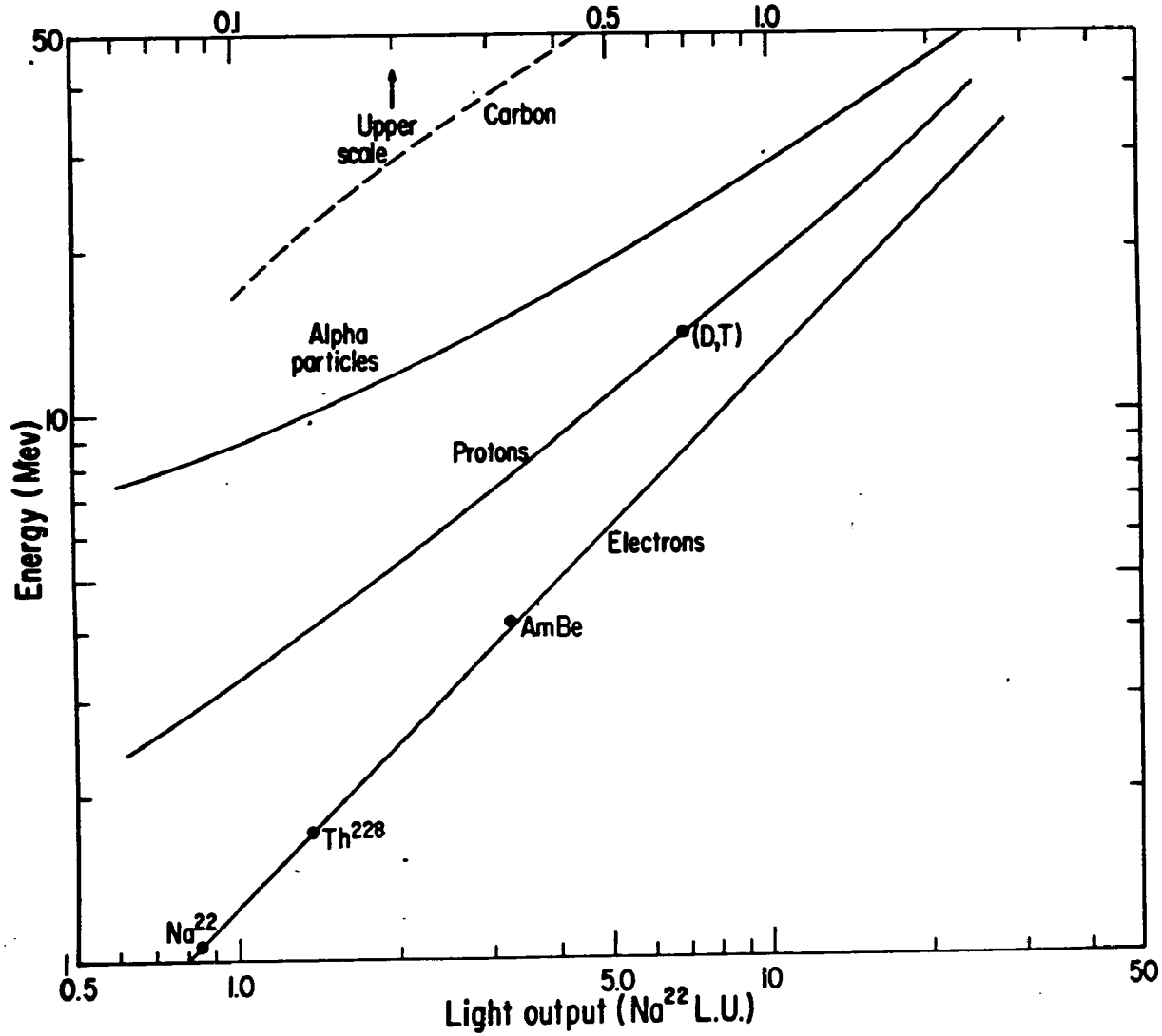
0.1
0.5
1.0
50
Upper scale
Carbon
Alpha particles
(D,T)
Protons
Electrons
AmBe
10
Energy (Mev)
Th228
Na22
1
0.5
1.0
5.0
10
50
Light output (Na22 L.U.)

Figure 11

Figure 12

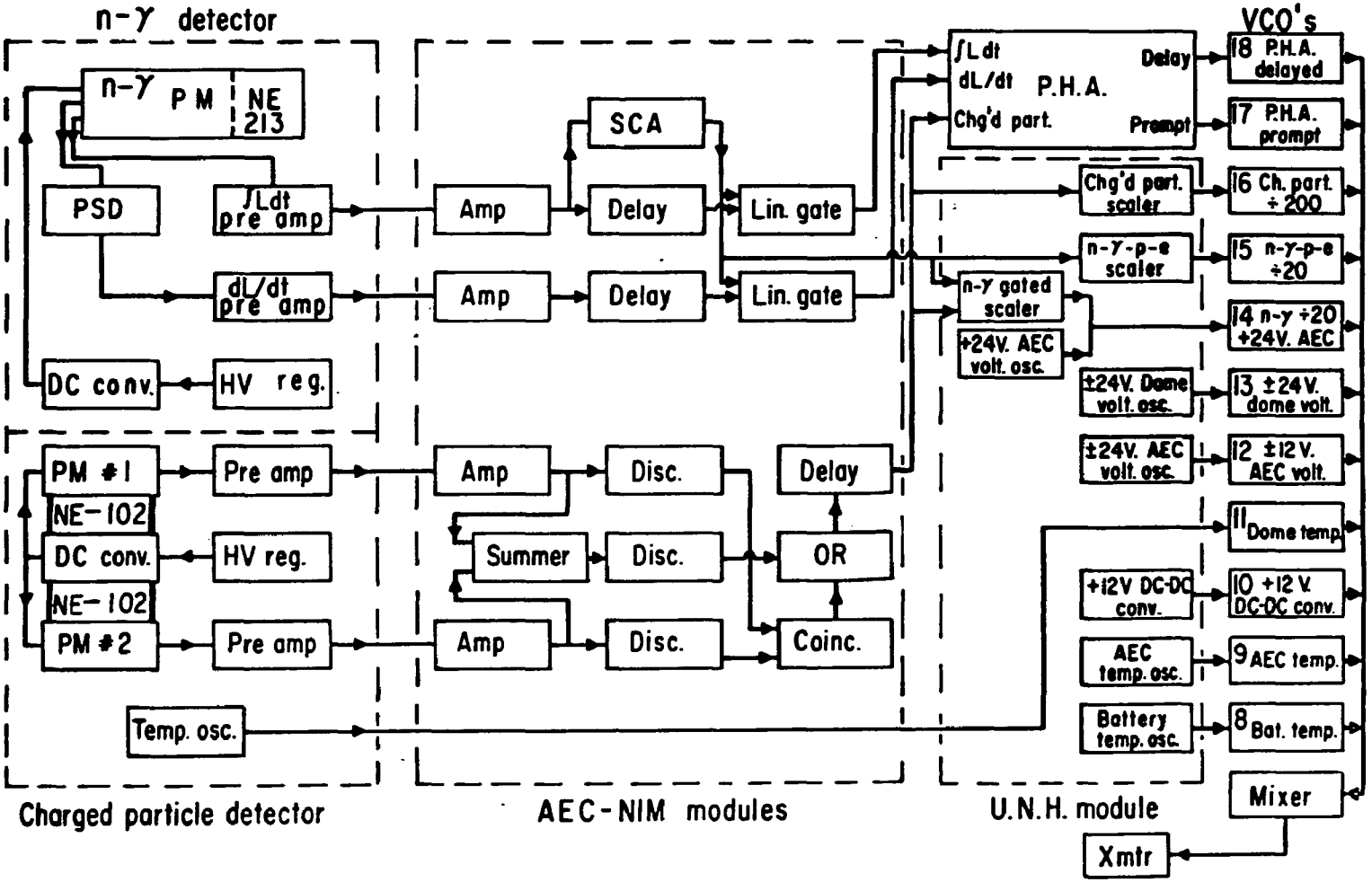
n-γ detector
n-γ PM
NE 213
PSD
∫Ldt pre amp
dL/dt pre amp
DC conv.
HV reg.
SCA
Amp
Delay
Lin. gate
Amp
Delay
Lin. gate
PM #1
NE-102
DC conv.
NE-102
PM #2
Pre amp
HV reg.
Pre amp
Amp
Disc.
Summer
Disc.
Amp
Disc.
Delay
OR
Coinc.
Temp. osc.
∫L dt
dL/dt P.H.A.
Chg'd part.
Delay
Prompt
Chg'd part. scaler
n-γ-p-e scaler
n-γ gated scaler
+24V. AEC volt. osc.
±24V. Dome volt. osc.
±24V. AEC volt. osc.
+12V DC-DC conv.
AEC temp. osc.
Battery temp. osc.
VCO's
18 P.H.A. delayed
17 P.H.A. prompt
16 Ch. part. ÷200
15 n-γ-p-e ÷20
14 n-γ ÷20 +24V. AEC
13 ±24V. dome volt.
12 ±12V. AEC volt.
11 Dome temp.
10 +12V DC-DC conv.
9 AEC temp.
8 Bat. temp.
Mixer
Xmtr
Charged particle detector
AEC-NIM modules
U.N.H. module

Figure 13a

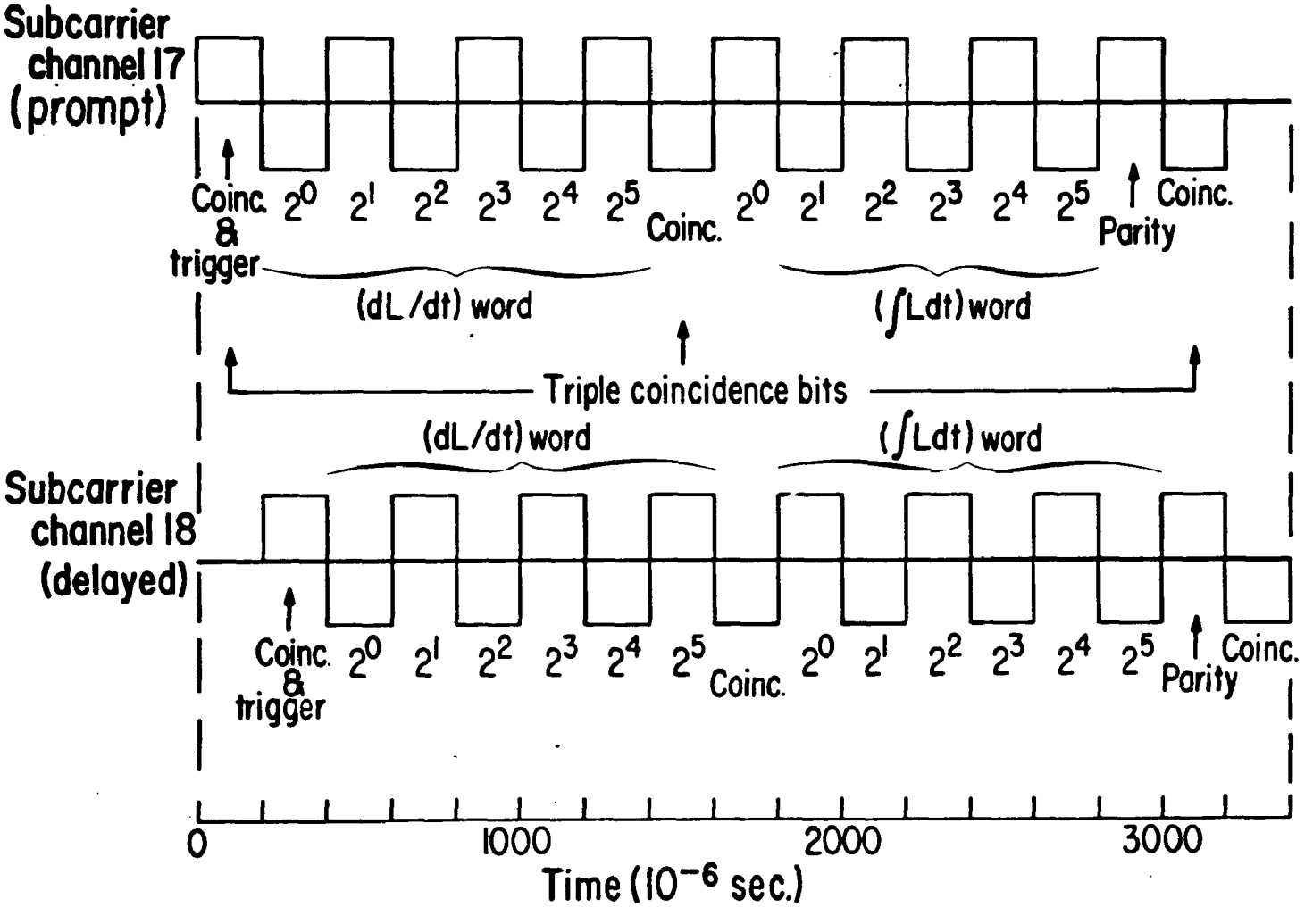
Subcarrier channel 17 (prompt)
Coinc. & trigger
2^0 2^1 2^2 2^3 2^4 2^5
Coinc.
2^0 2^1 2^2 2^3 2^4 2^5
Parity
Coinc.
(dL/dt) word
(∫Ldt) word
Triple coincidence bits
(dL/dt) word
(∫Ldt) word
Subcarrier channel 18 (delayed)
Coinc. & trigger
2^0 2^1 2^2 2^3 2^4 2^5
Coinc.
2^0 2^1 2^2 2^3 2^4 2^5
Parity
Coinc.
0
1000
2000
3000
Time (10^{-6} sec.)

Figure 13b

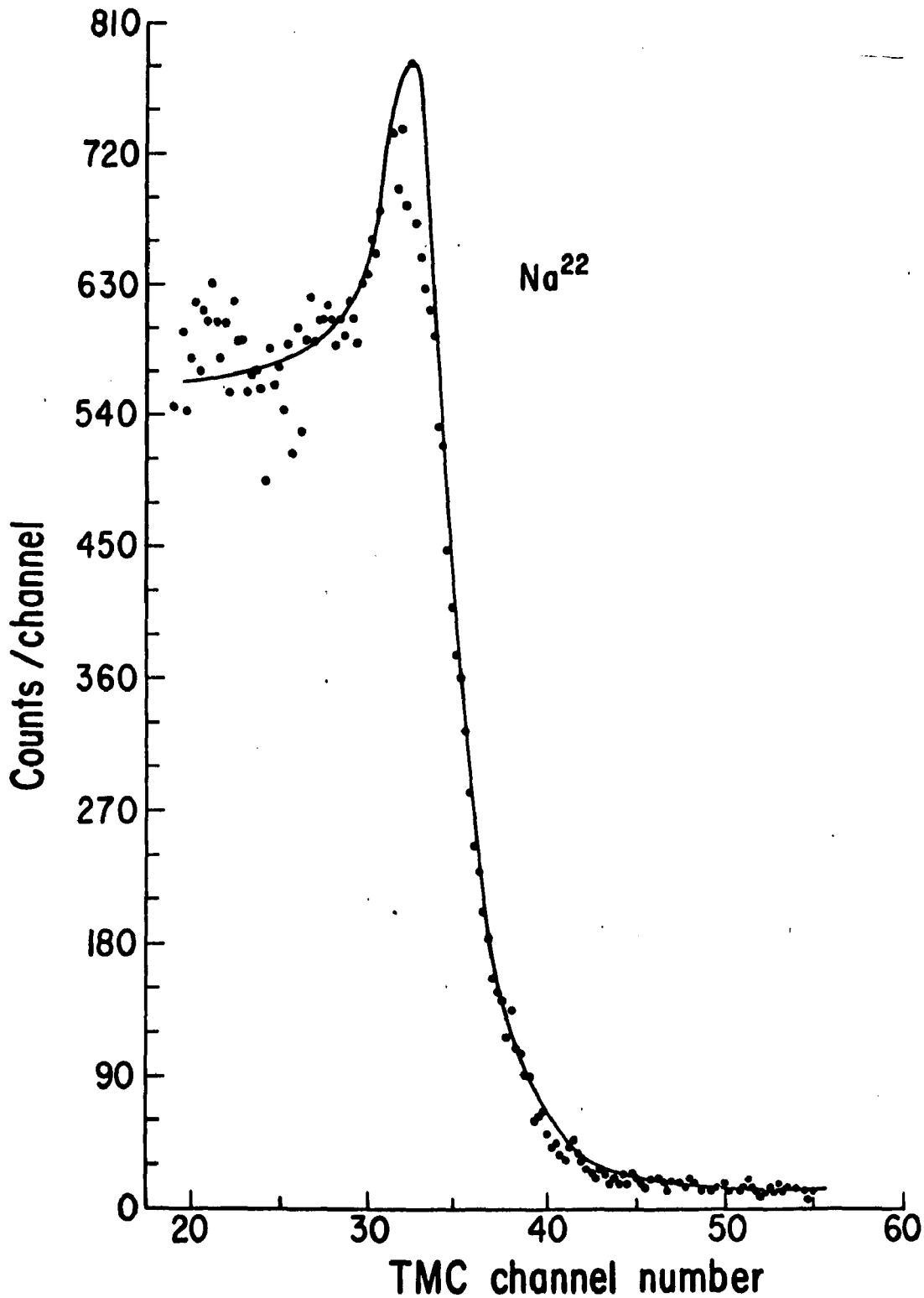
810
720
630
540
450
360
270
180
90
0
Counts /channel
Na22
20
30
40
50
60
TMC channel number

Figure 14a

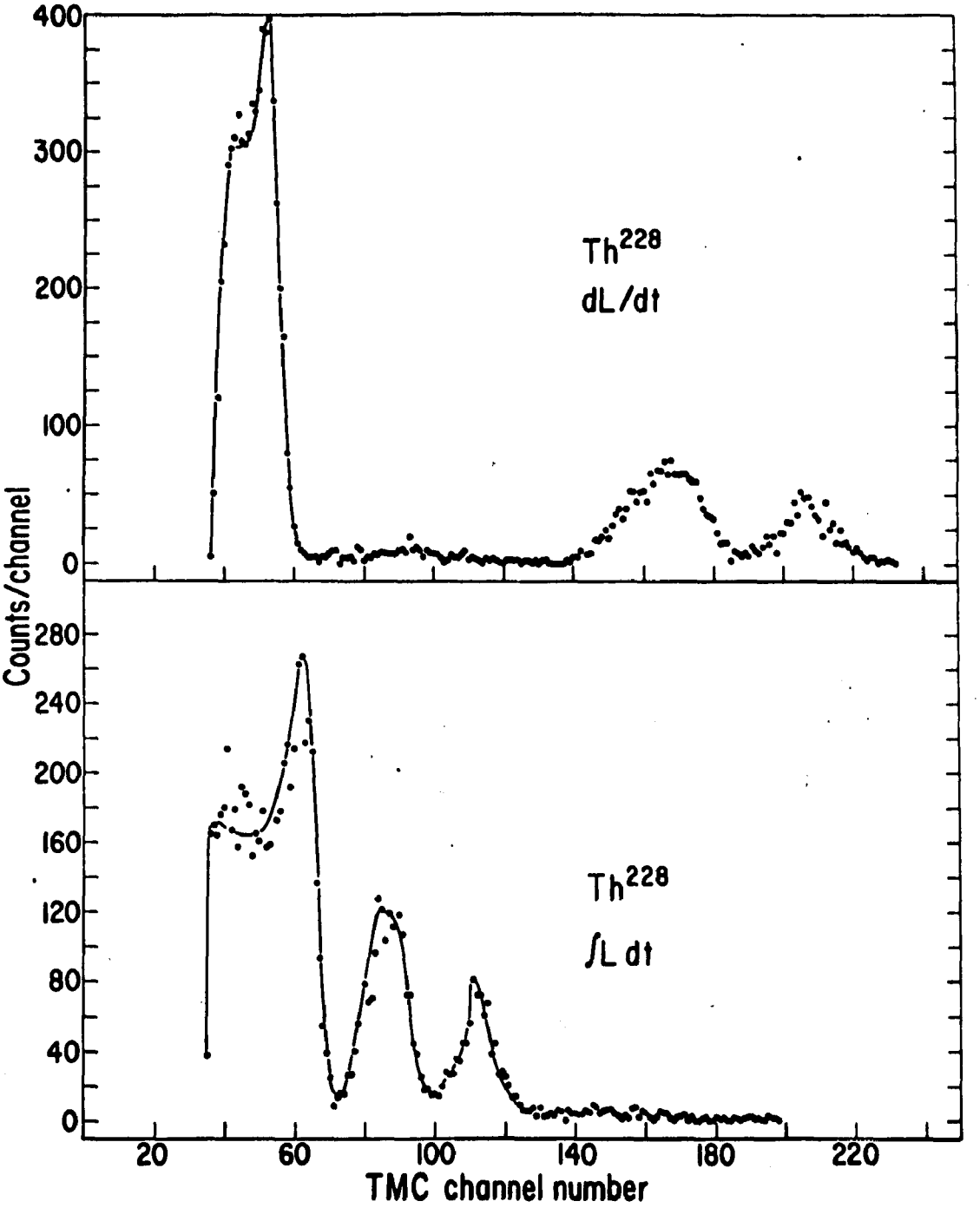
400
300
200
100
0
Th228
dL/dt
Counts/channel
280
240
200
160
120
80
40
0
Th228
∫L dt
20
60
100
140
180
220
TMC channel number

Figure 14b

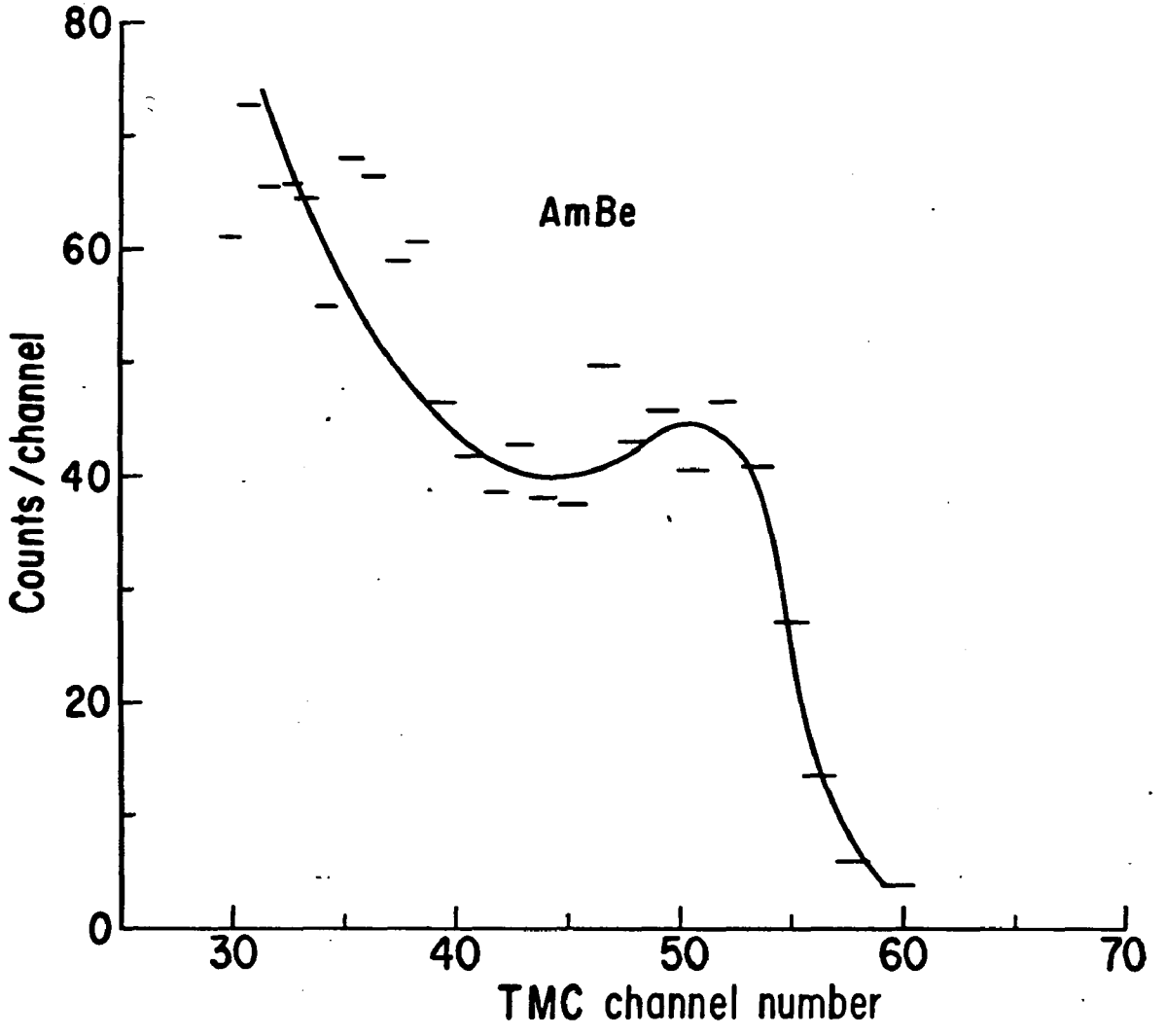
80
60
40
20
0
Counts /channel
AmBe
30
40
50
60
70
TMC channel number

Figure 15a

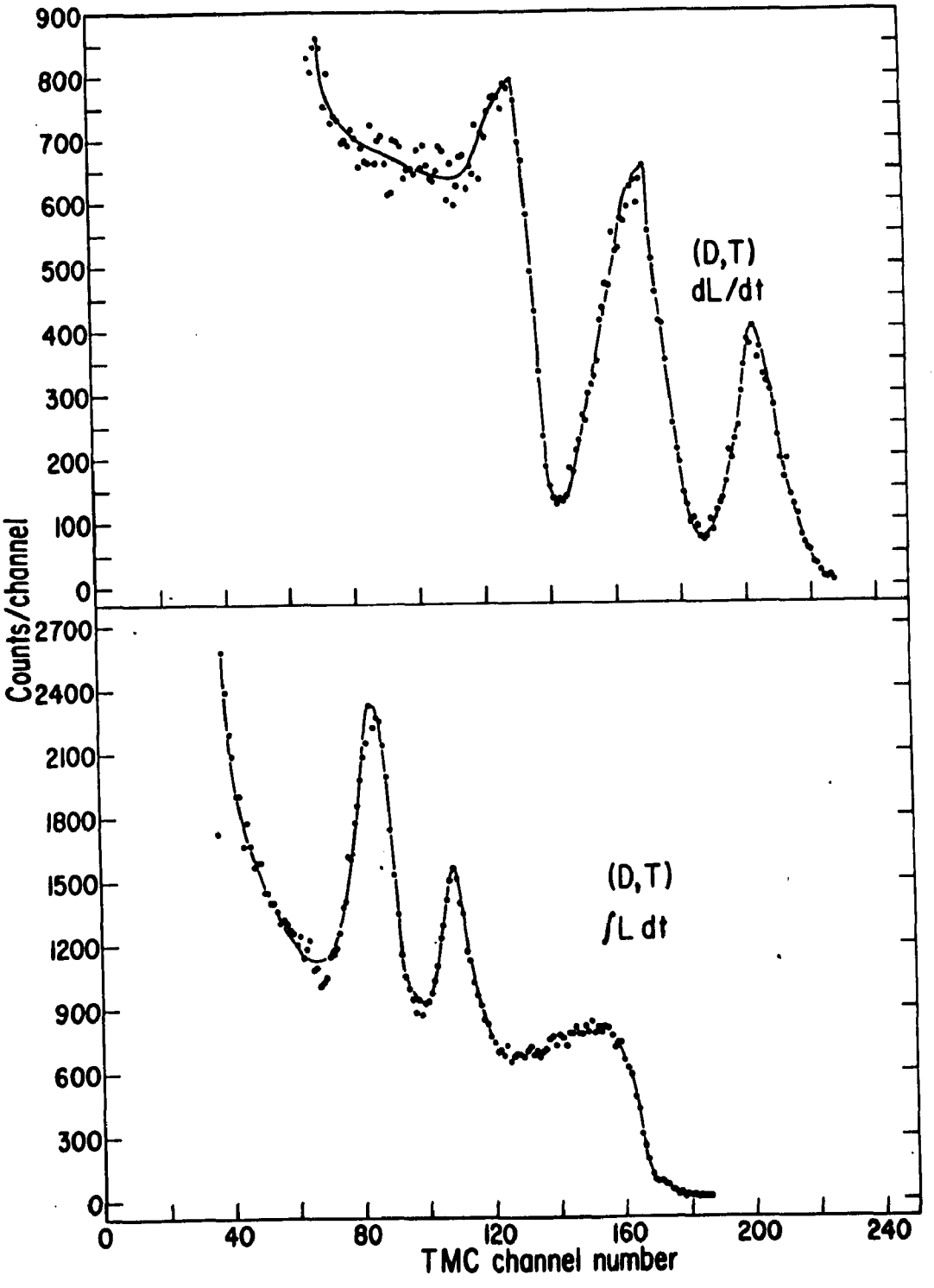
900
800
700
600
500
400
300
200
100
0
(D,T)
dL/dt
Counts/channel
2700
2400
2100
1800
1500
1200
900
600
300
0
(D,T)
∫L dt
0
40
80
120
160
200
240
TMC channel number

Figure 15b

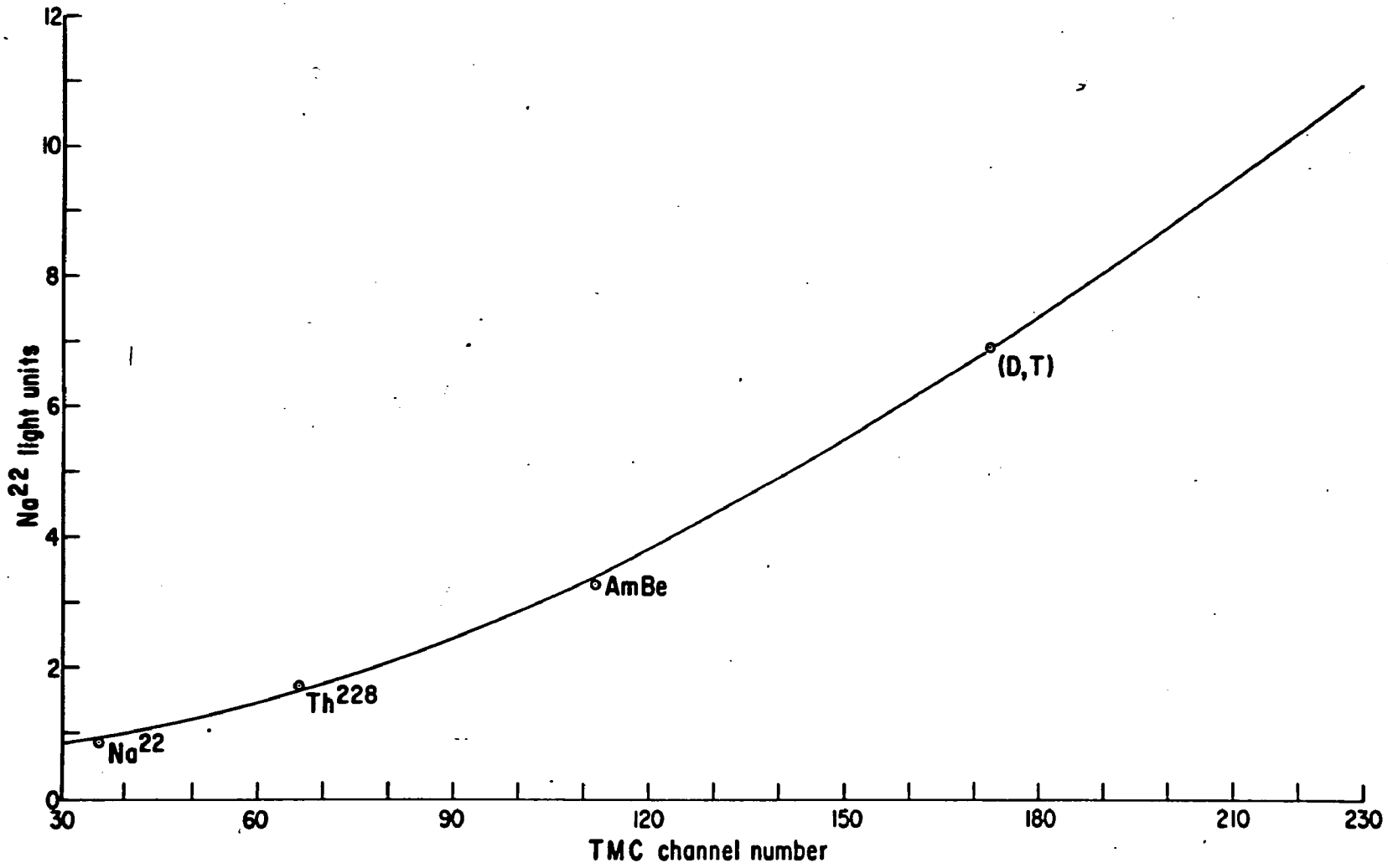
12
10
8
6
4
2
0
Na^{22} light units
Na^{22}
Th^{228}
AmBe
(D,T)
30
60
90
120
150
180
210
230
TMC channel number

Figure 16

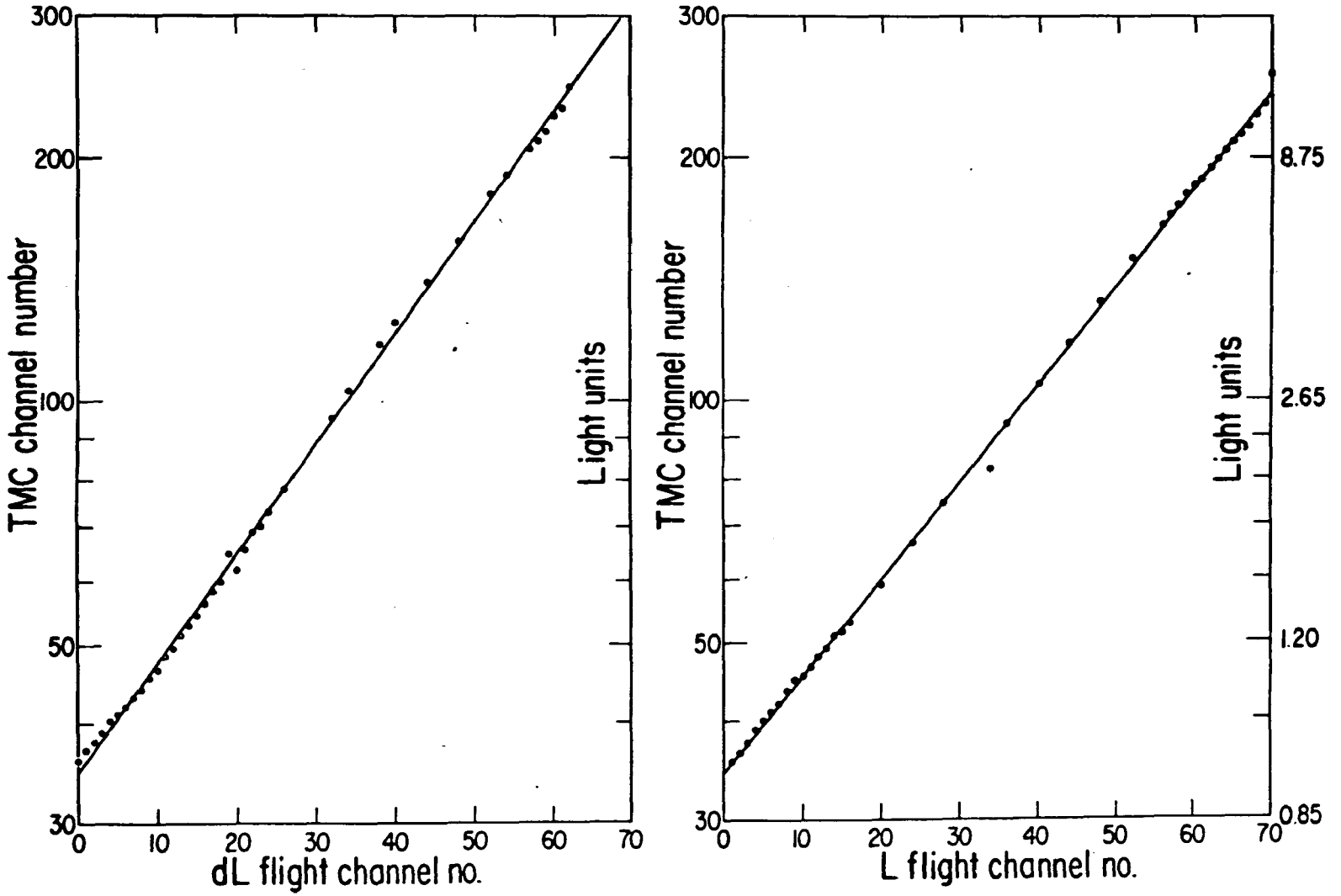
300
200
100
50
30
TMC channel number
0
10
20
30
40
50
60
70
dL flight channel no.
Light units
L flight channel no.
8.75
2.65
1.20
0.85

Figure 17

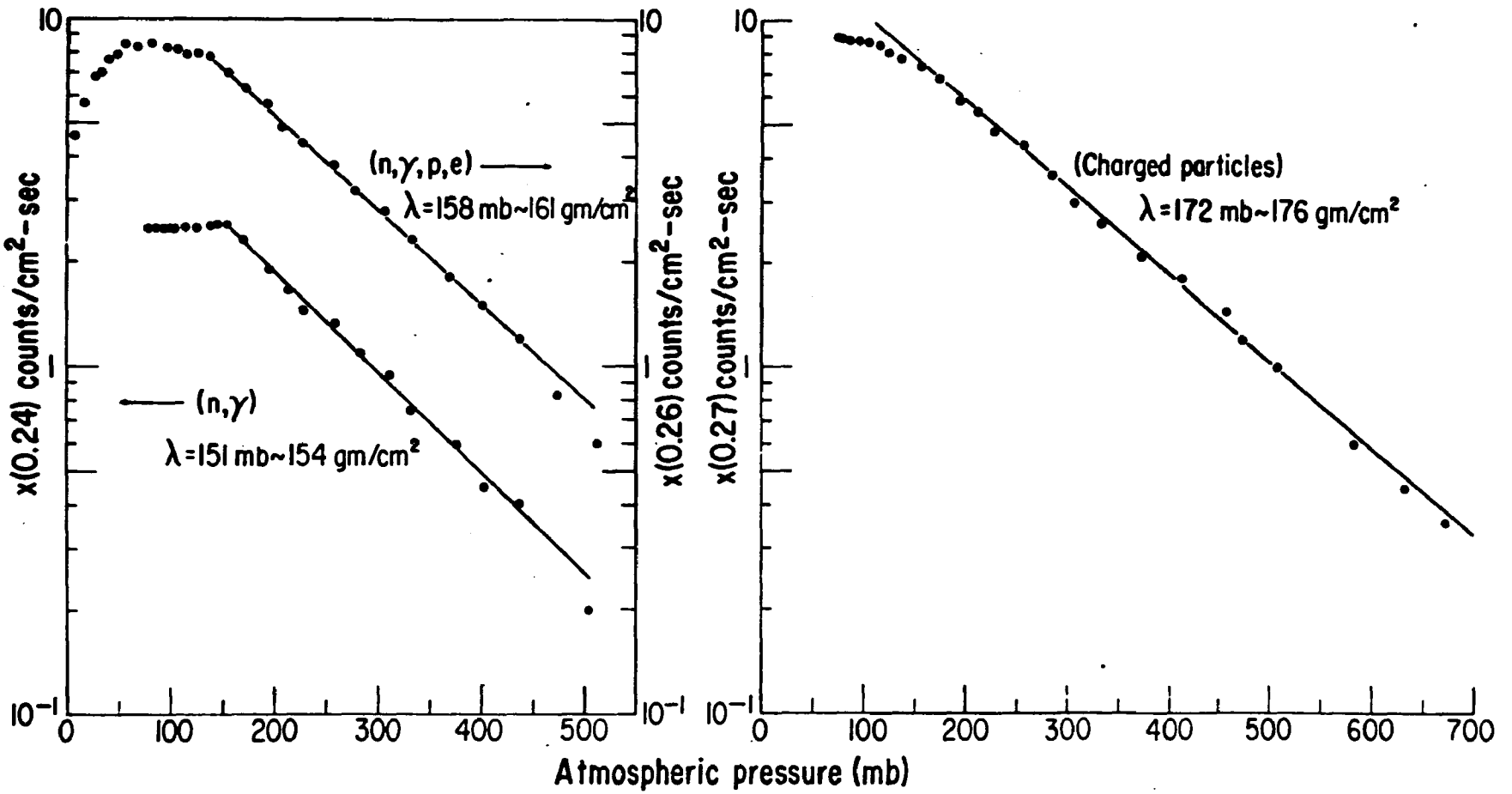
10
1
10⁻¹
x(0.24) counts/cm²-sec
(n,γ,p,e)
λ=158 mb~161 gm/cm²
(n,γ)
λ=151 mb~154 gm/cm²
0
100
200
300
400
500
x(0.26) counts/cm²-sec
x(0.27) counts/cm²-sec
(Charged particles)
λ=172 mb~176 gm/cm²
600
700
Atmospheric pressure (mb)

Figure 18

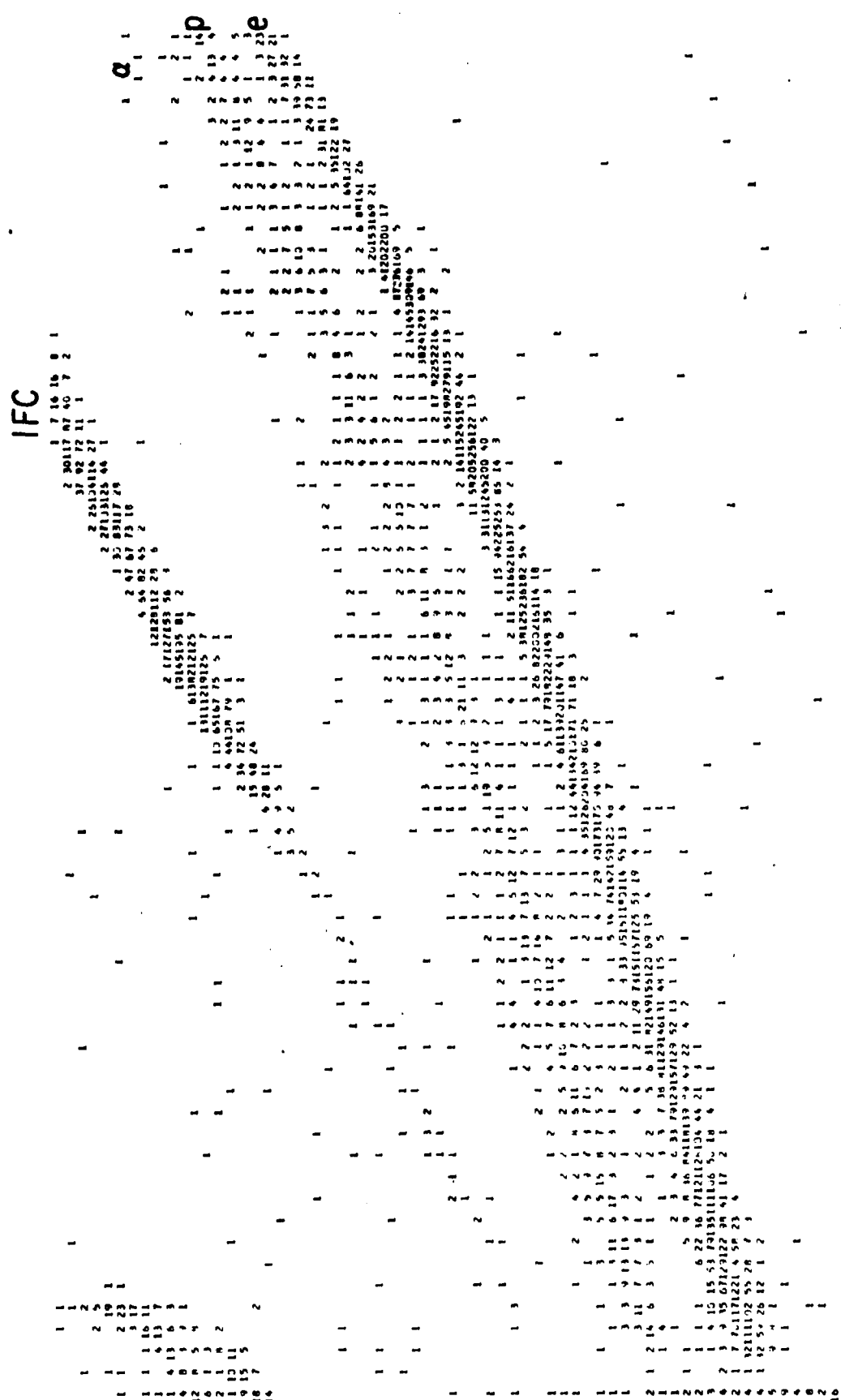

Figure 19

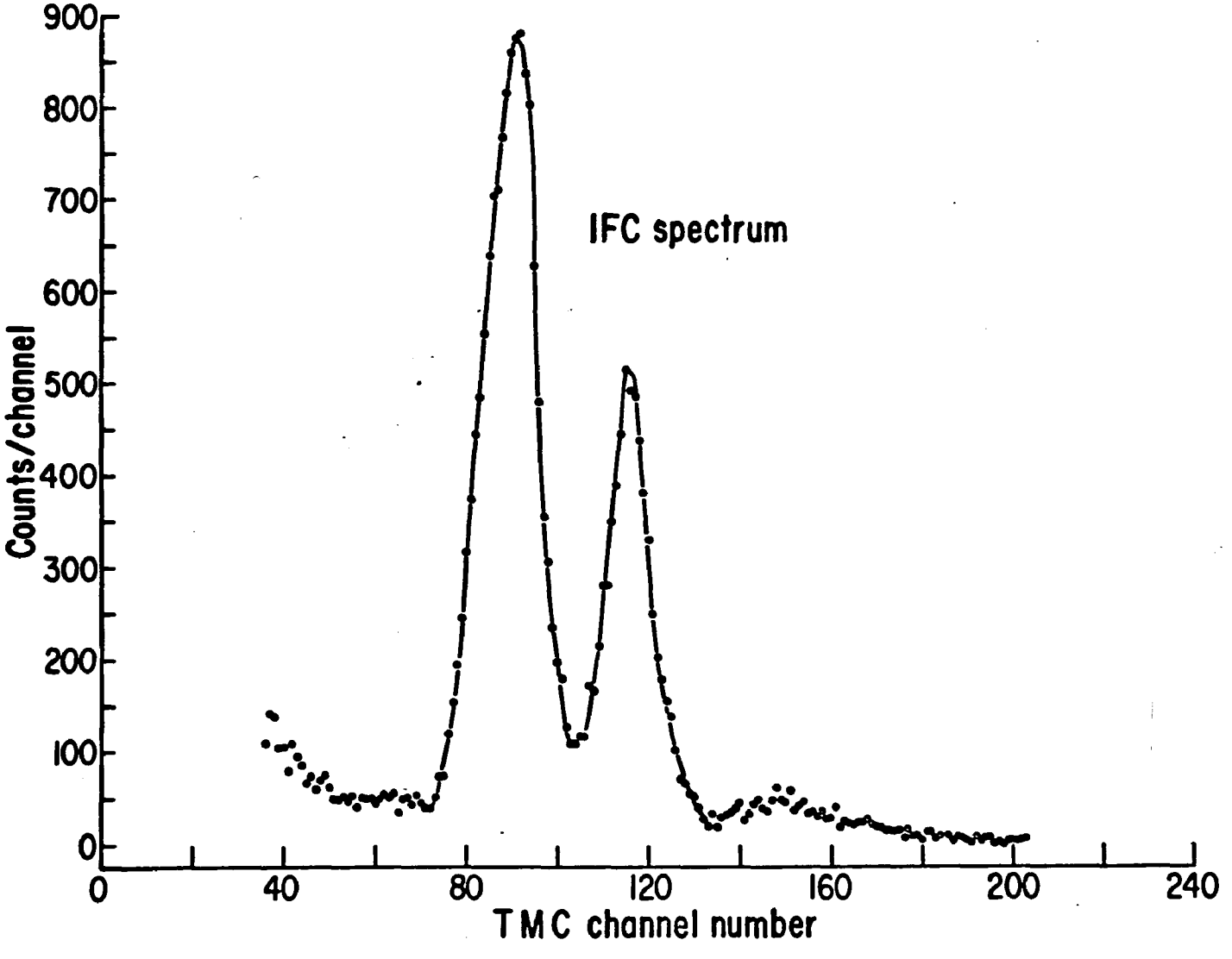
IFC spectrum
Counts/channel
TMC channel number
0
100
200
300
400
500
600
700
800
900
0
40
80
120
160
200
240

Figure 20

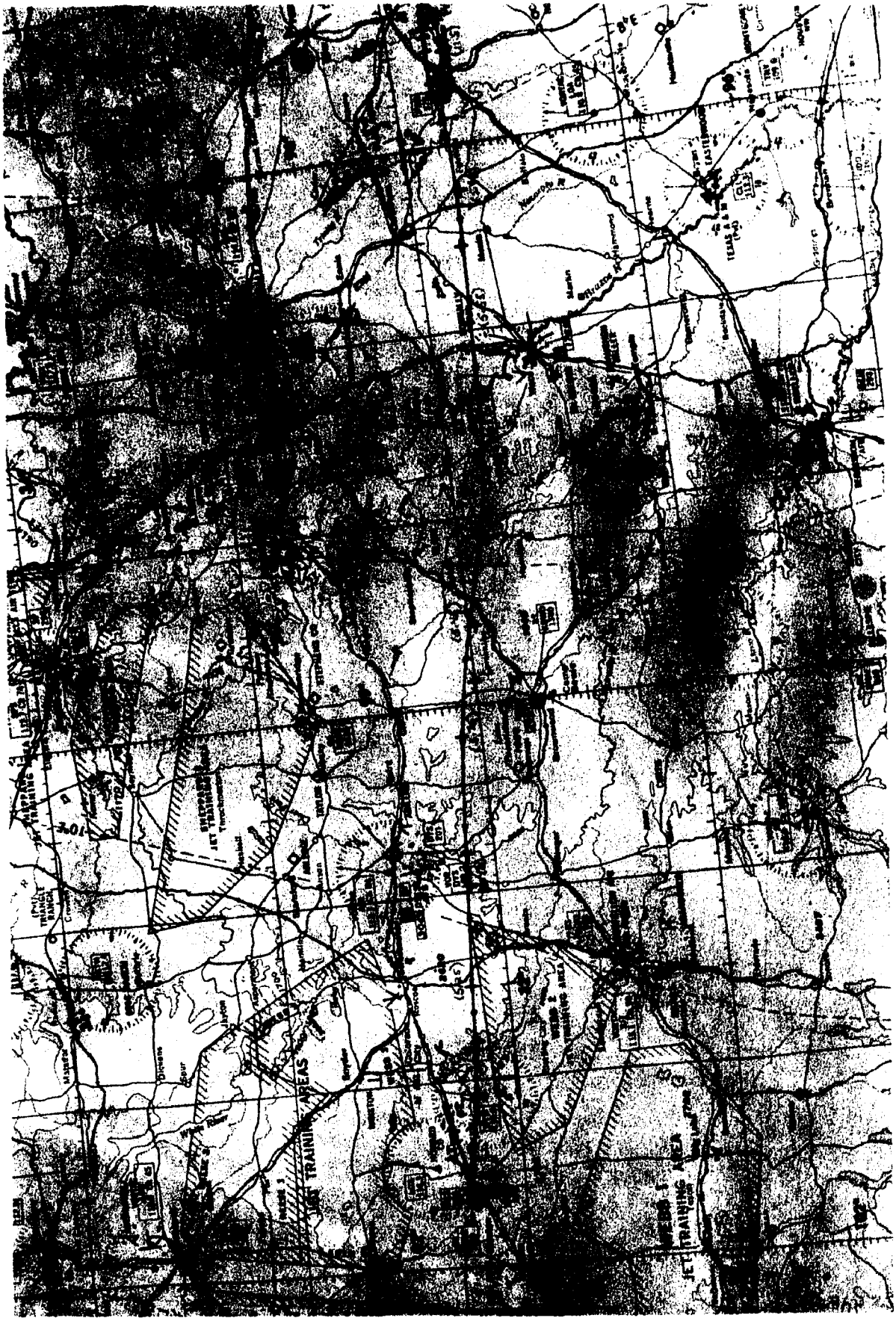

Figure 21

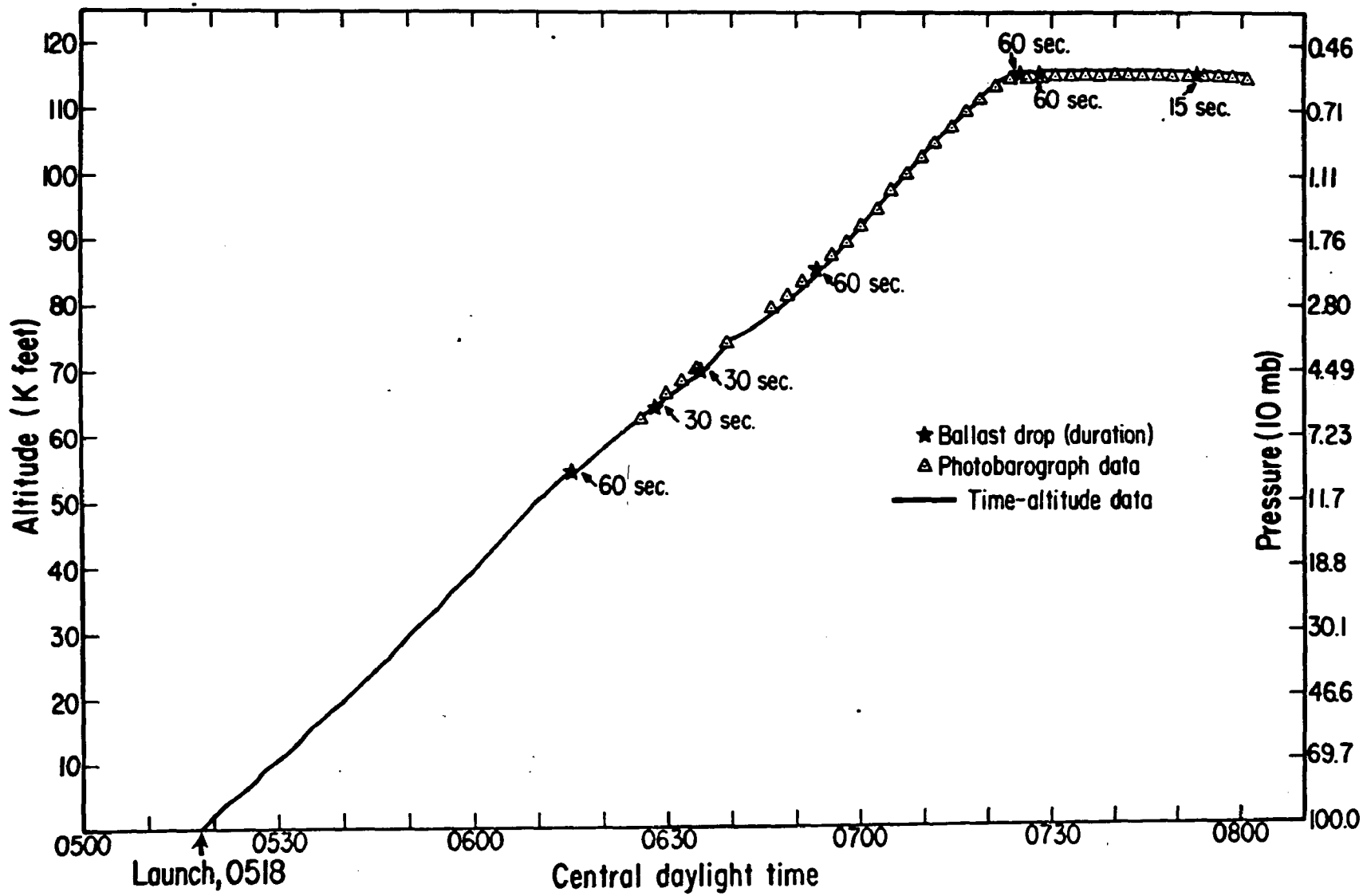
Altitude (K feet)
120
110
100
90
80
70
60
50
40
30
20
10
Pressure (10 mb)
0.46
0.71
1.11
1.76
2.80
4.49
7.23
11.7
18.8
30.1
46.6
69.7
100.0
60 sec.
60 sec.
15 sec.
60 sec.
30 sec.
30 sec.
60 sec.
★ Ballast drop (duration)
△ Photobarograph data
Time-altitude data
0500
0530
0600
0630
0700
0730
0800
Launch, 0518
Central daylight time

Figure 22

dL/dt→

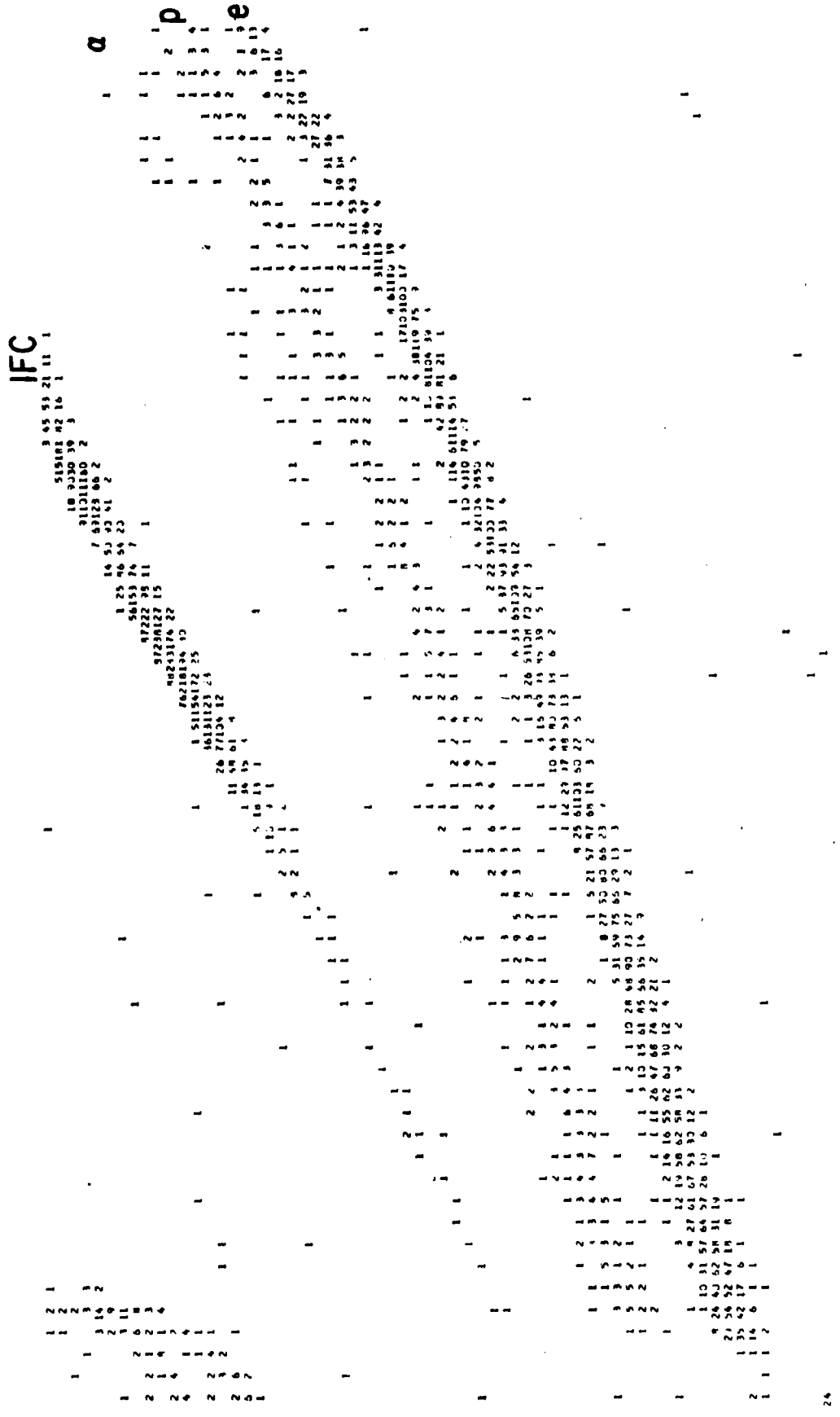

∫Ldt→

Figure 23

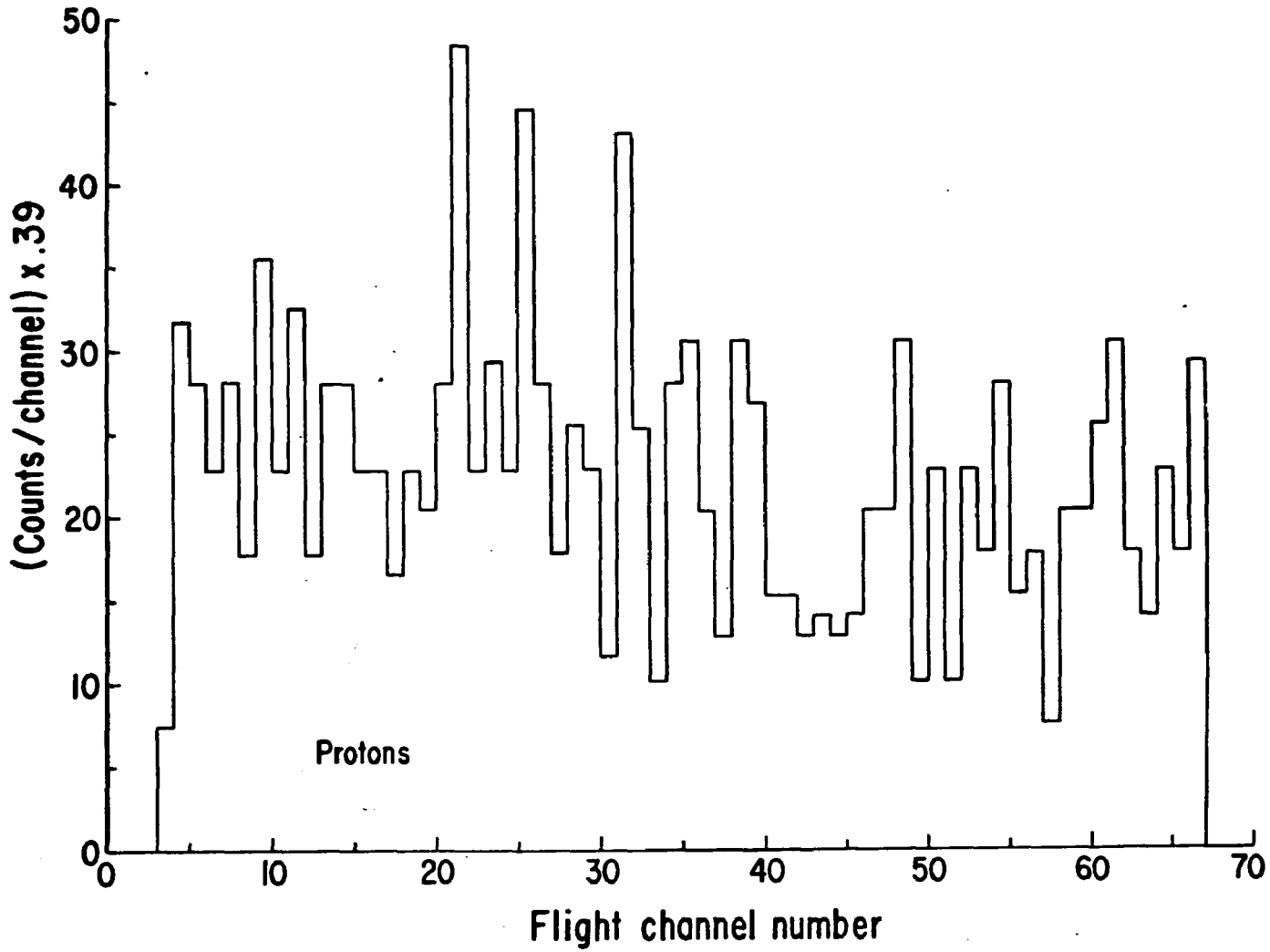
50
40
30
20
10
0
(Counts/channel) x .39
Protons
0
10
20
30
40
50
60
70
Flight channel number

Figure 24a

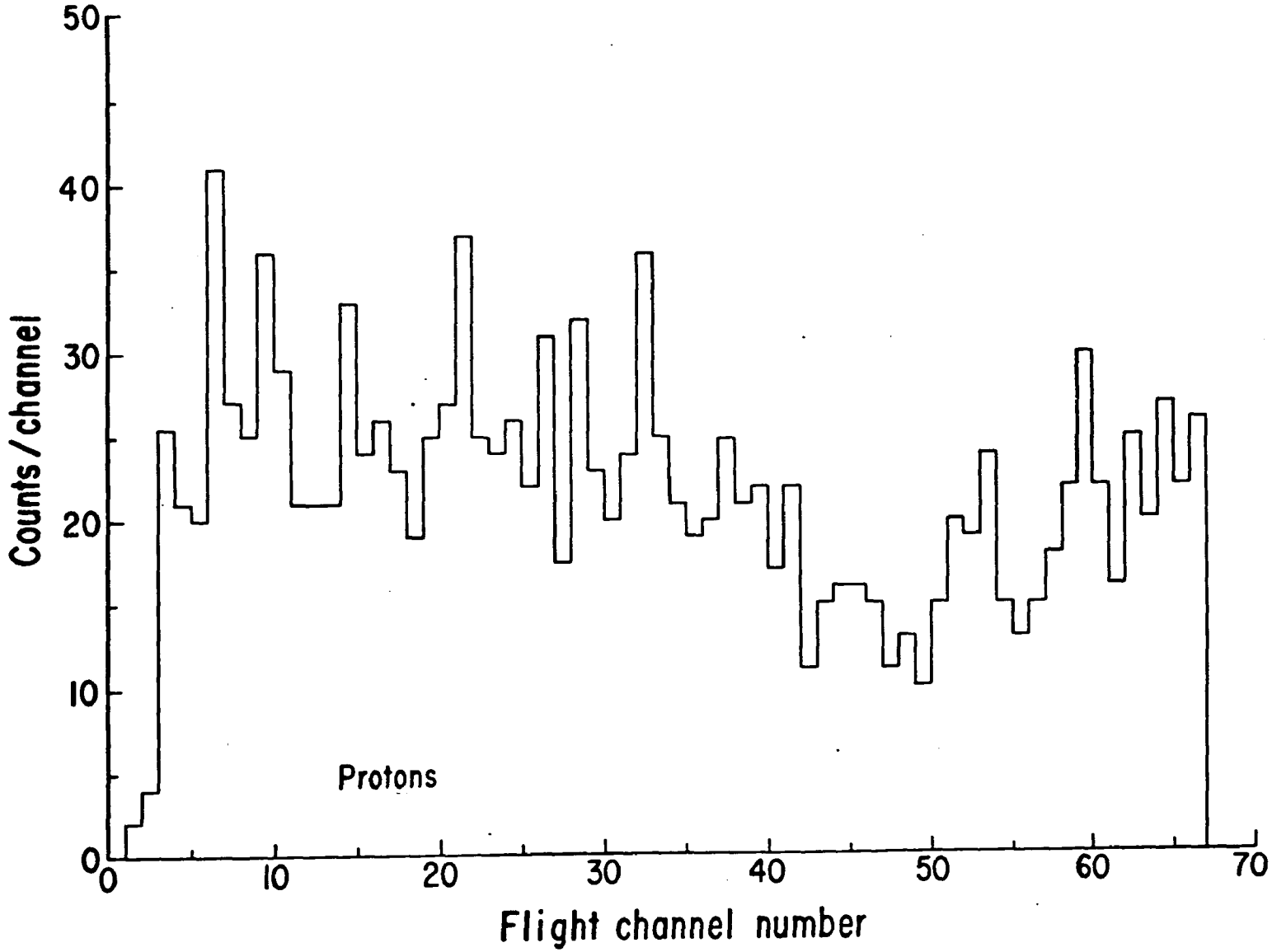
Counts/channel
Flight channel number
Protons
0
10
20
30
40
50
60
70

Figure 24b

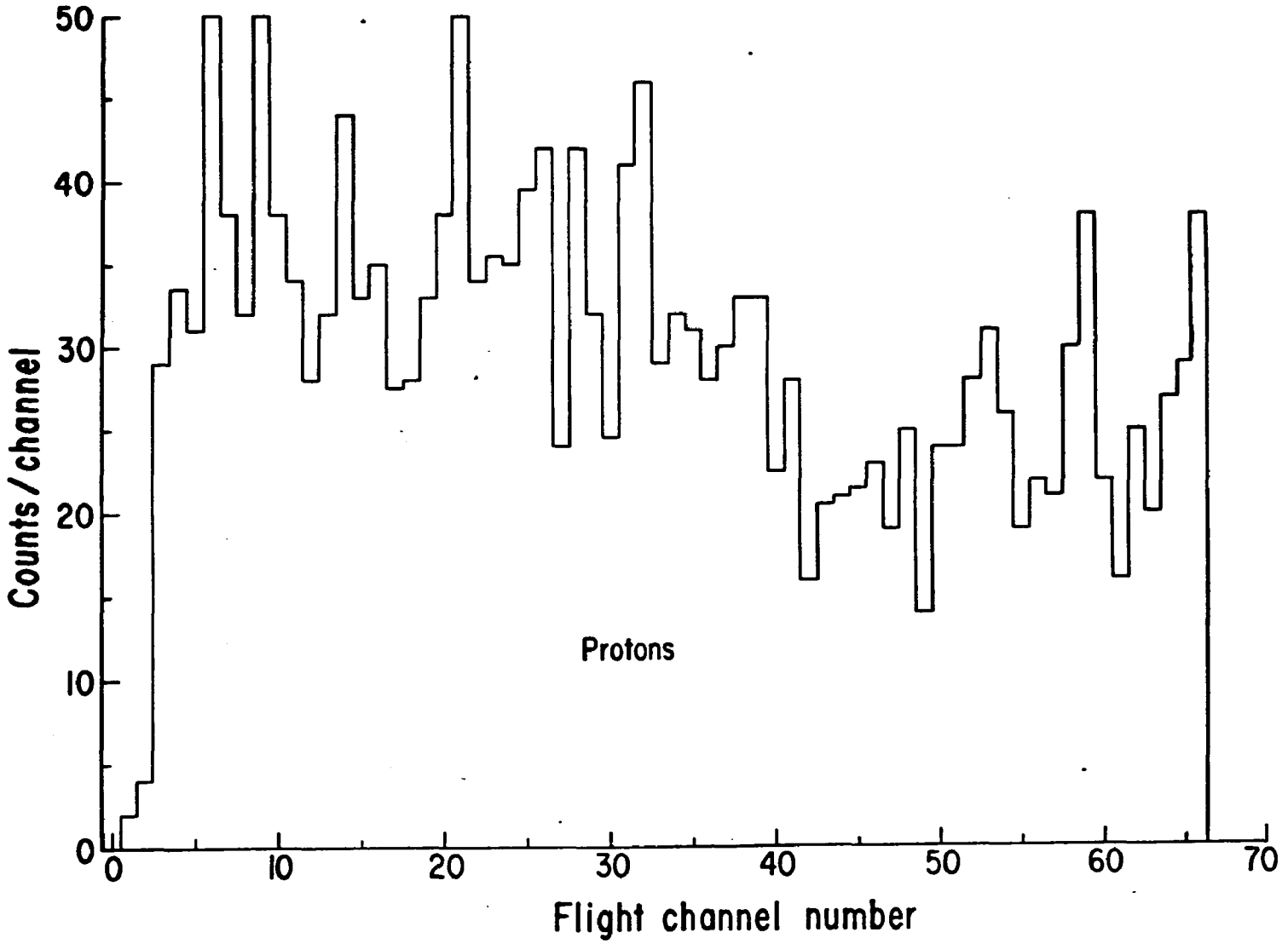
Counts/channel
Protons
Flight channel number
0
10
20
30
40
50
60
70

Figure 24c

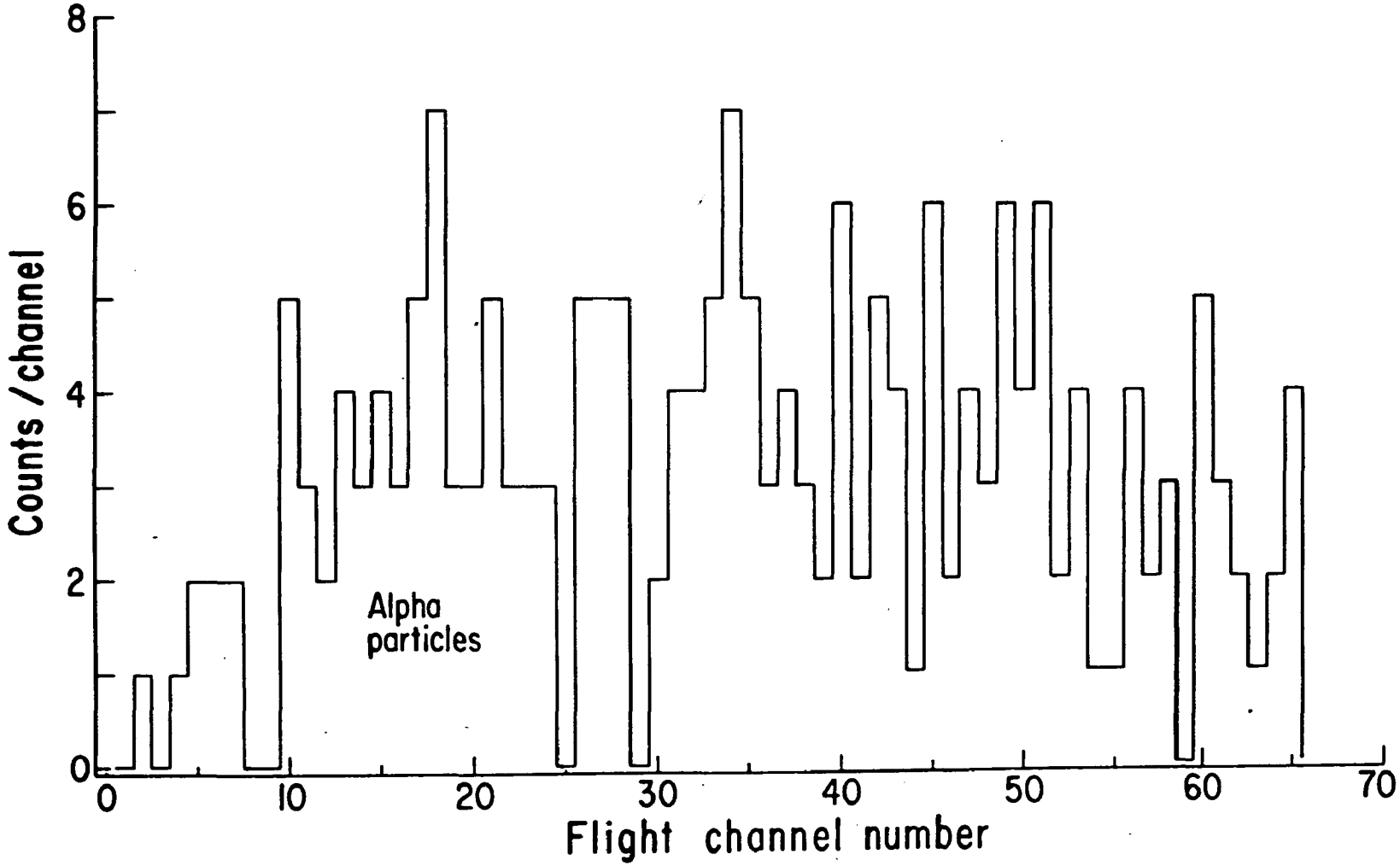
Counts / channel
Alpha particles
Flight channel number
0
2
4
6
8
0
10
20
30
40
50
60
70

Figure 25

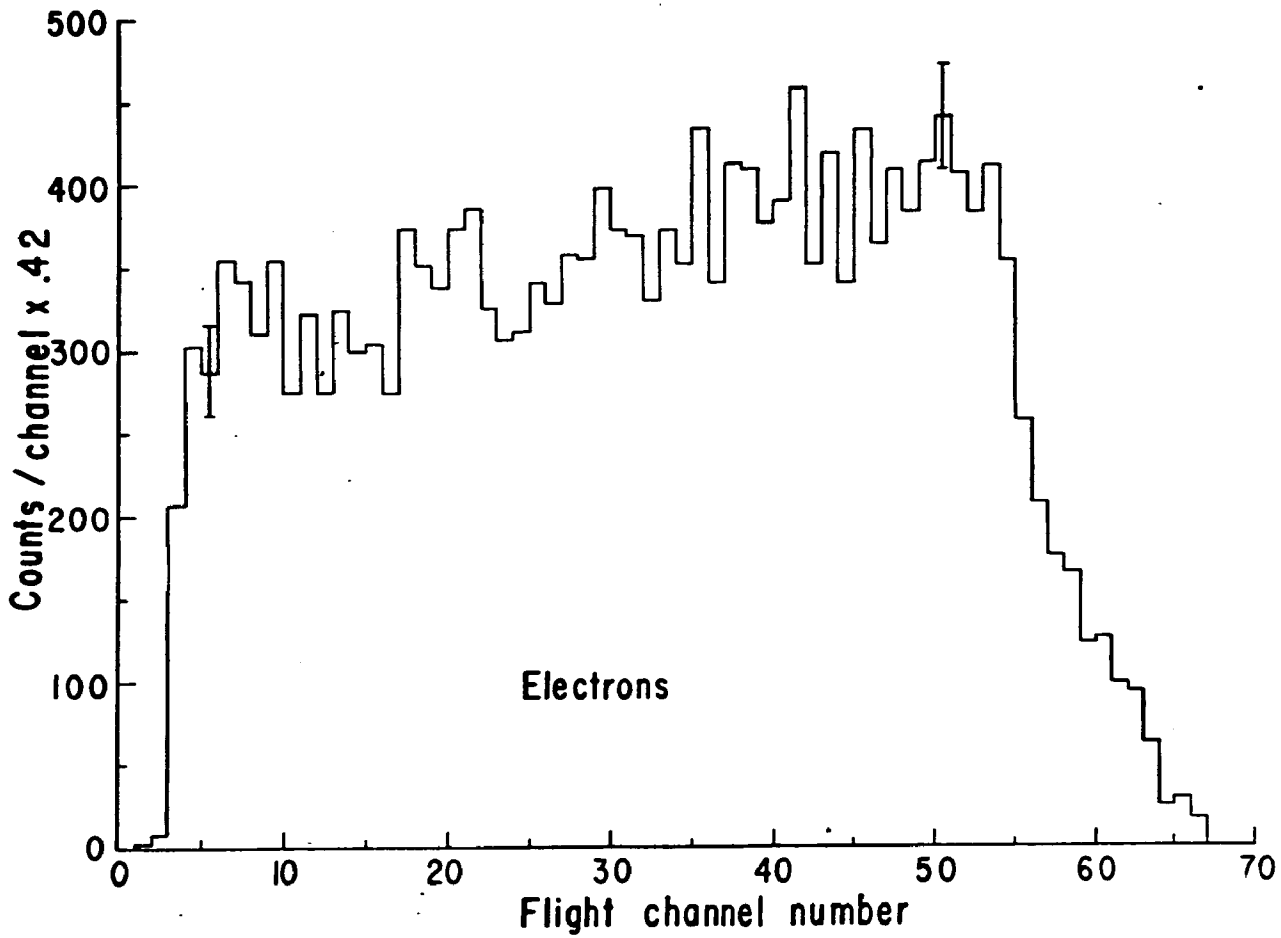
500
400
300
200
100
0
Counts / channel x .42
Electrons
0
10
20
30
40
50
60
70
Flight channel number

Figure 26a

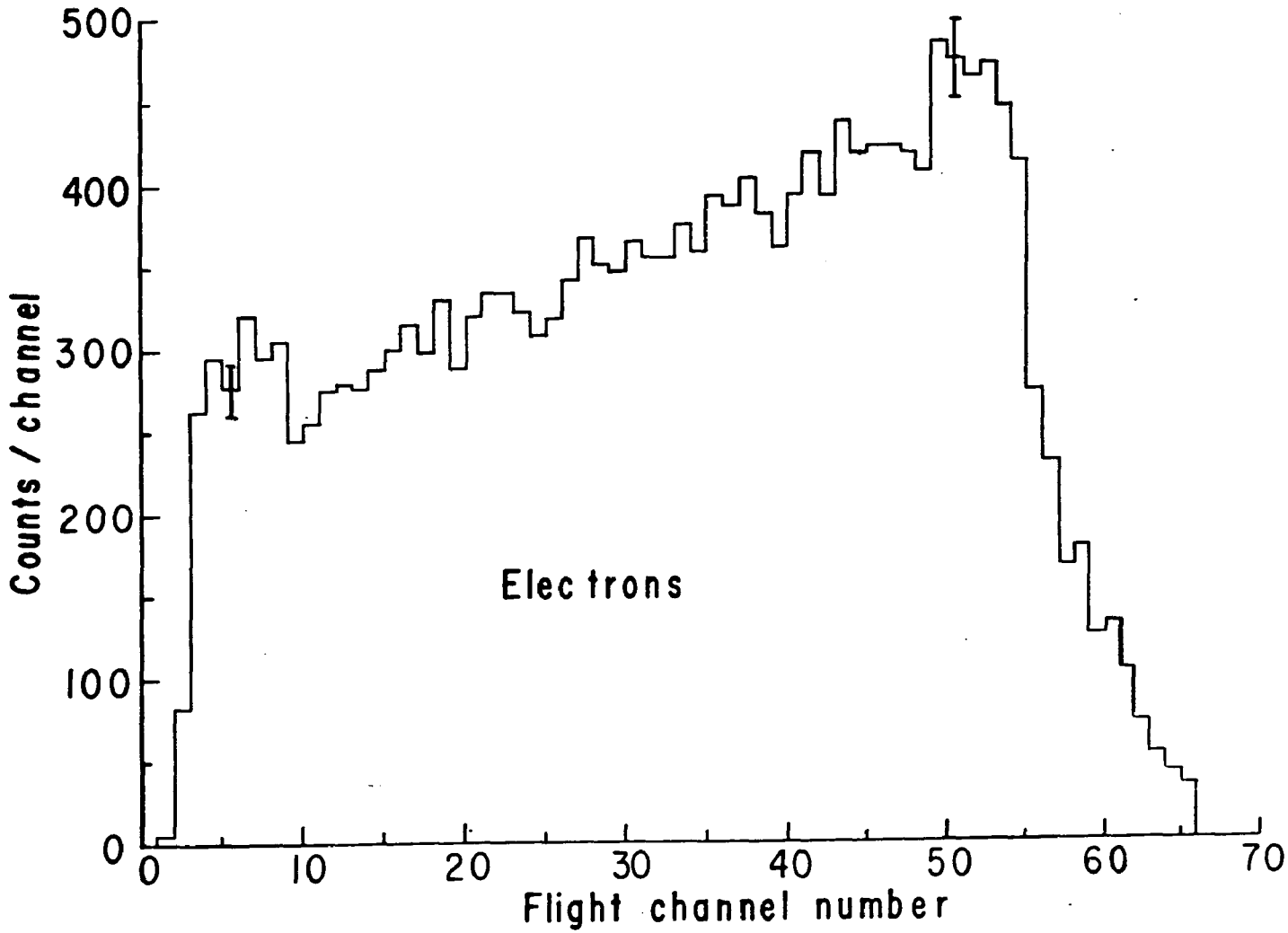
Counts / channel
500
400
300
200
100
0
Electrons
0
10
20
30
40
50
60
70
Flight channel number

Figure 26b

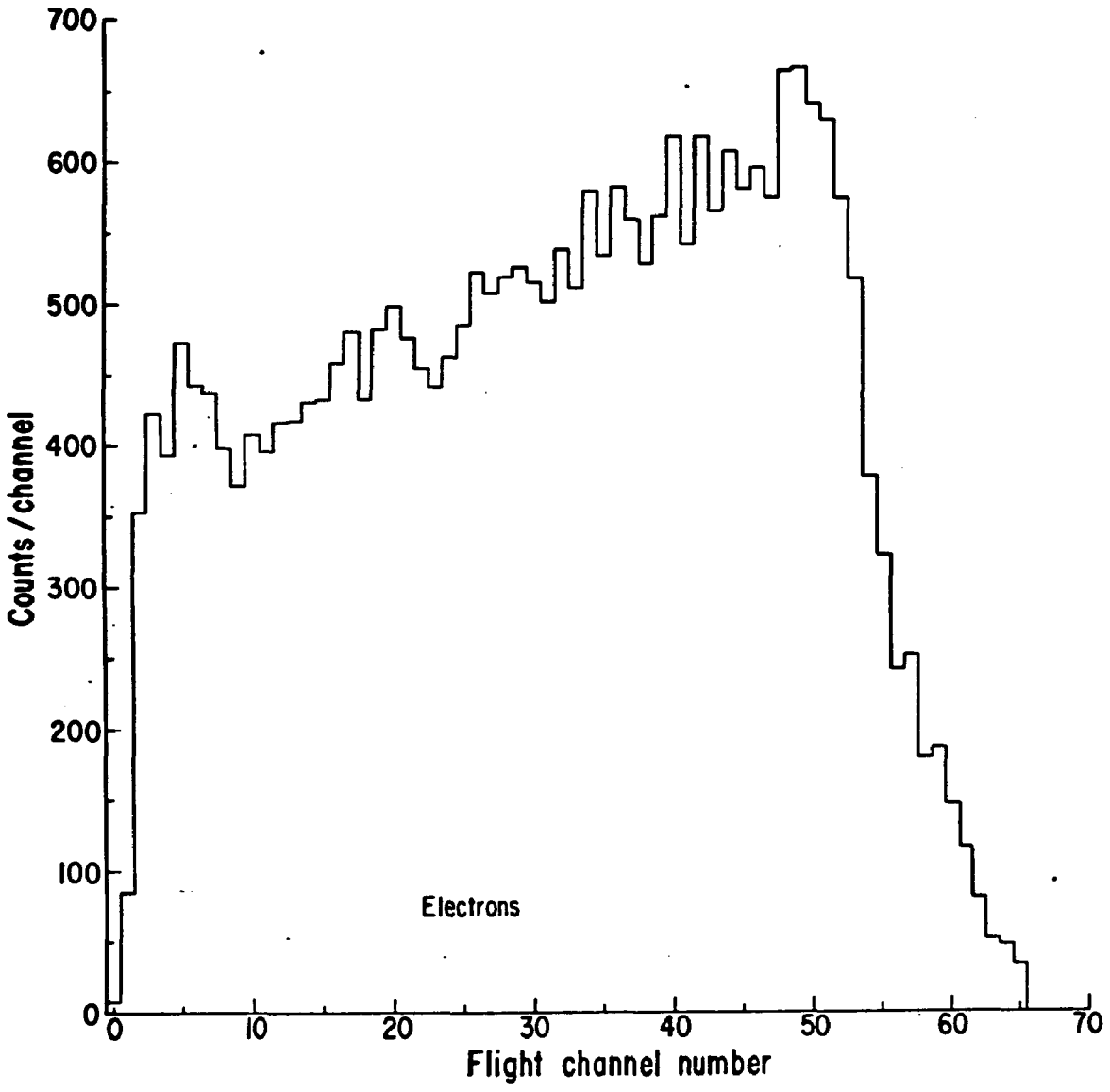
700
600
500
400
300
200
100
0
Counts / channel
Electrons
0
10
20
30
40
50
60
70
Flight channel number

Figure 26c

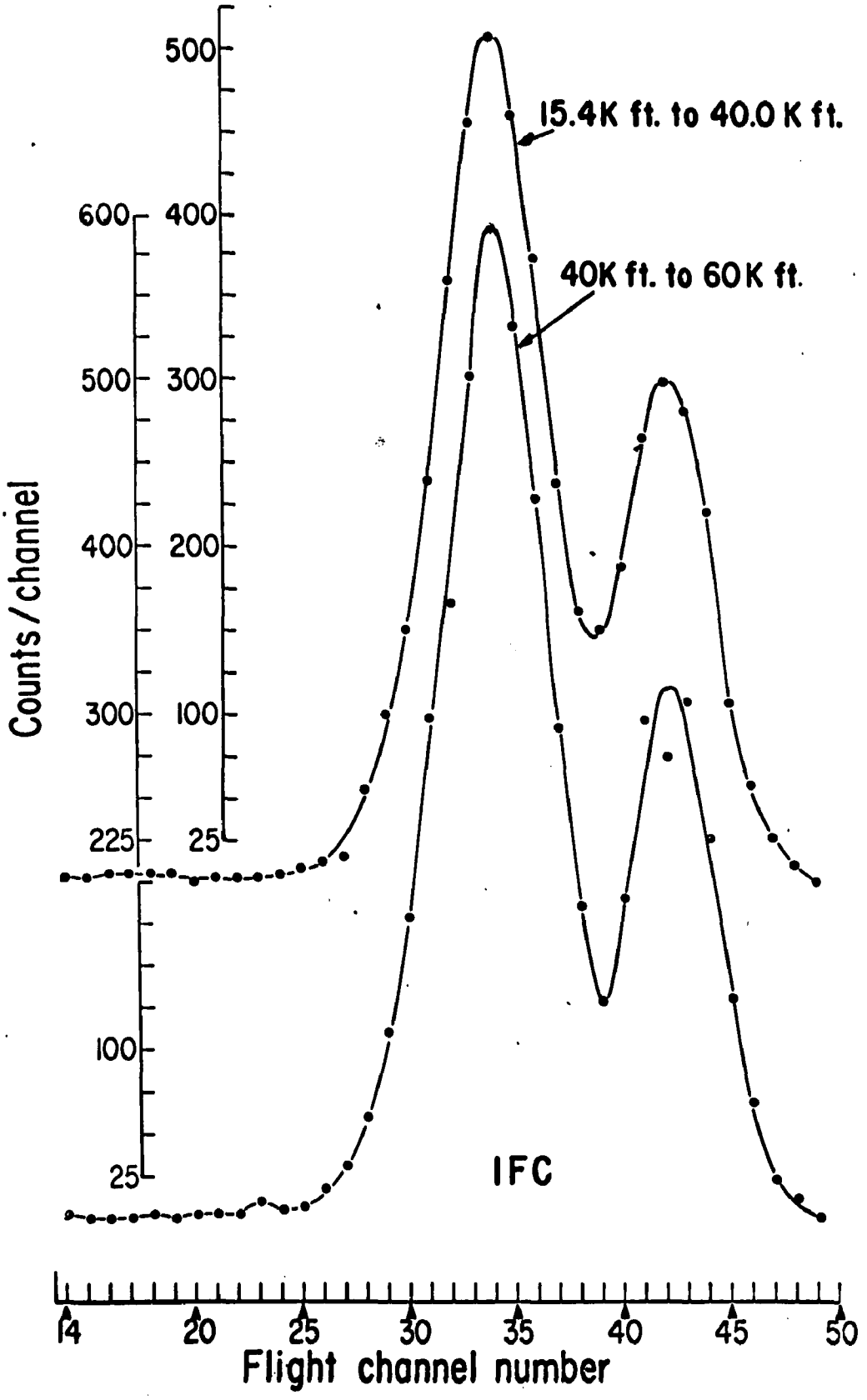
15.4K ft. to 40.0 K ft.
40K ft. to 60K ft.
Counts / channel
500
600
400
500
300
400
200
300
100
225
25
100
25
IFC
14
20
25
30
35
40
45
50
Flight channel number

Figure 27

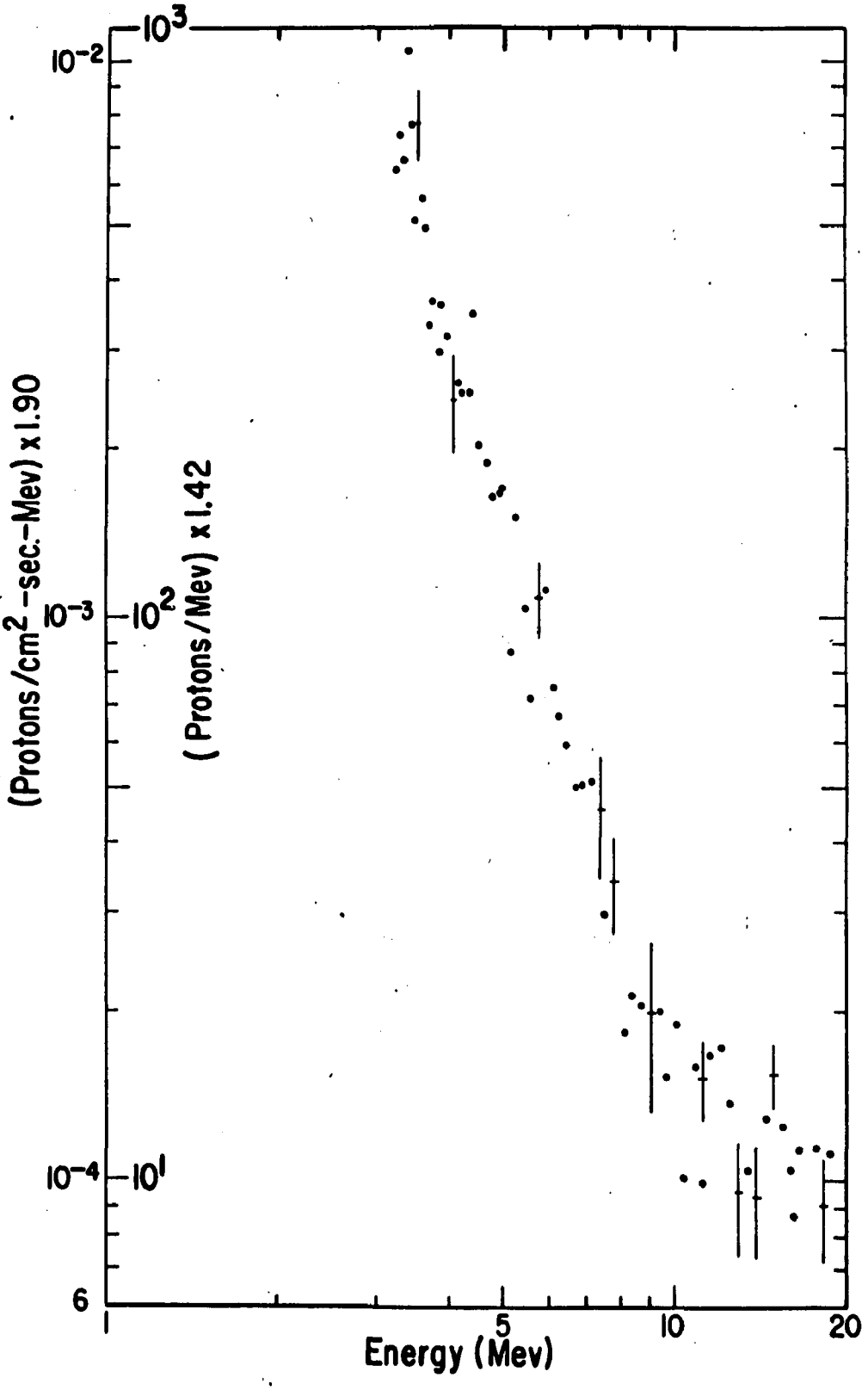
10^{3}
10^{-2}
10^{2}
10^{-3}
10^{1}
10^{-4}
(Protons/cm^2-sec.-Mev) x1.90
(Protons/Mev) x1.42
6
5
10
20
Energy (Mev)

Figure 28a

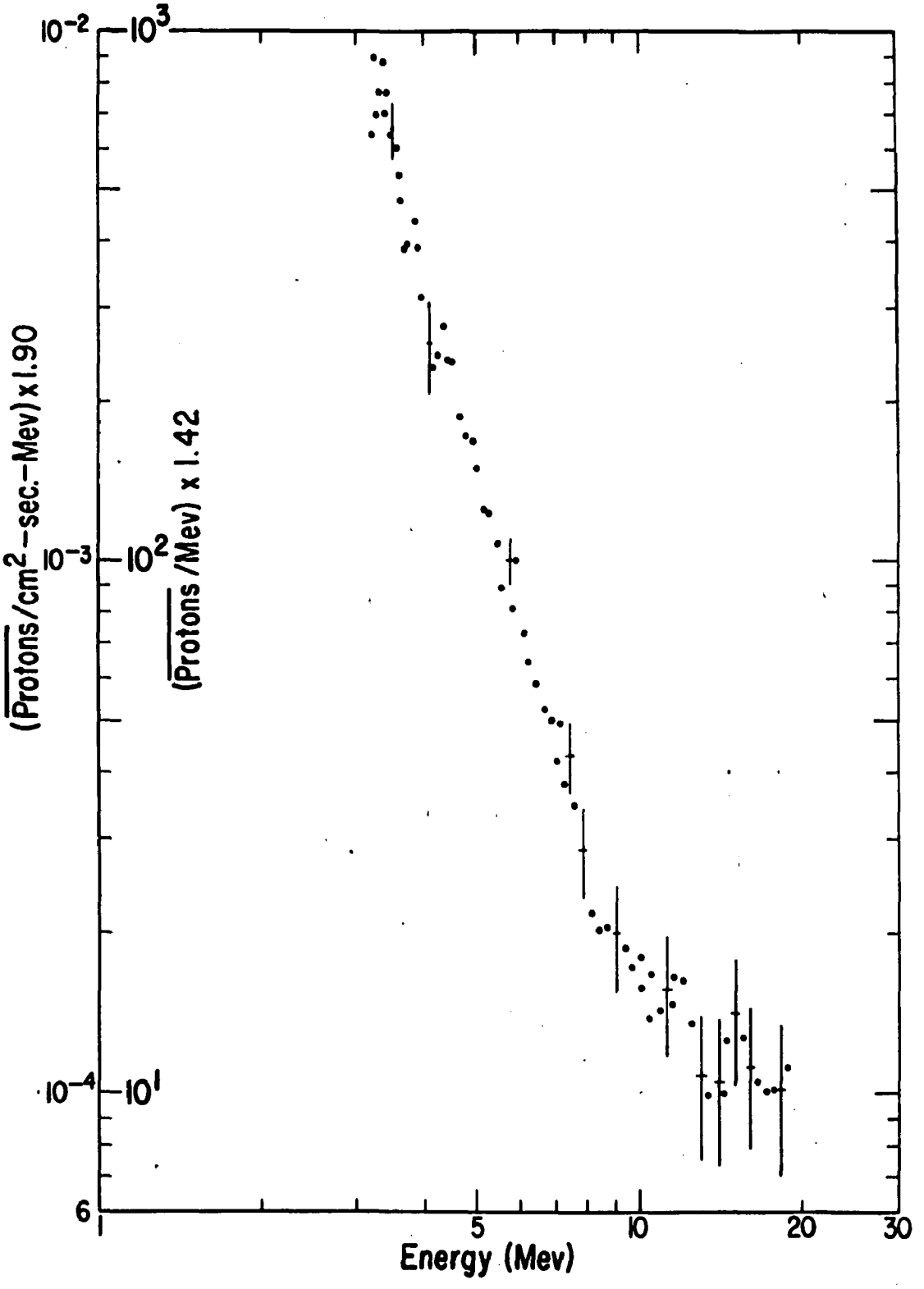
10^{-2}
10^{3}
10^{-3}
10^{2}
10^{-4}
10^{1}
6
$(\overline{\text{Protons}}/\text{cm}^2-\text{sec.}-\text{Mev})\times 1.90$
$(\overline{\text{Protons}}/\text{Mev})\times 1.42$
1
5
10
20
30
Energy (Mev)

Figure 28b

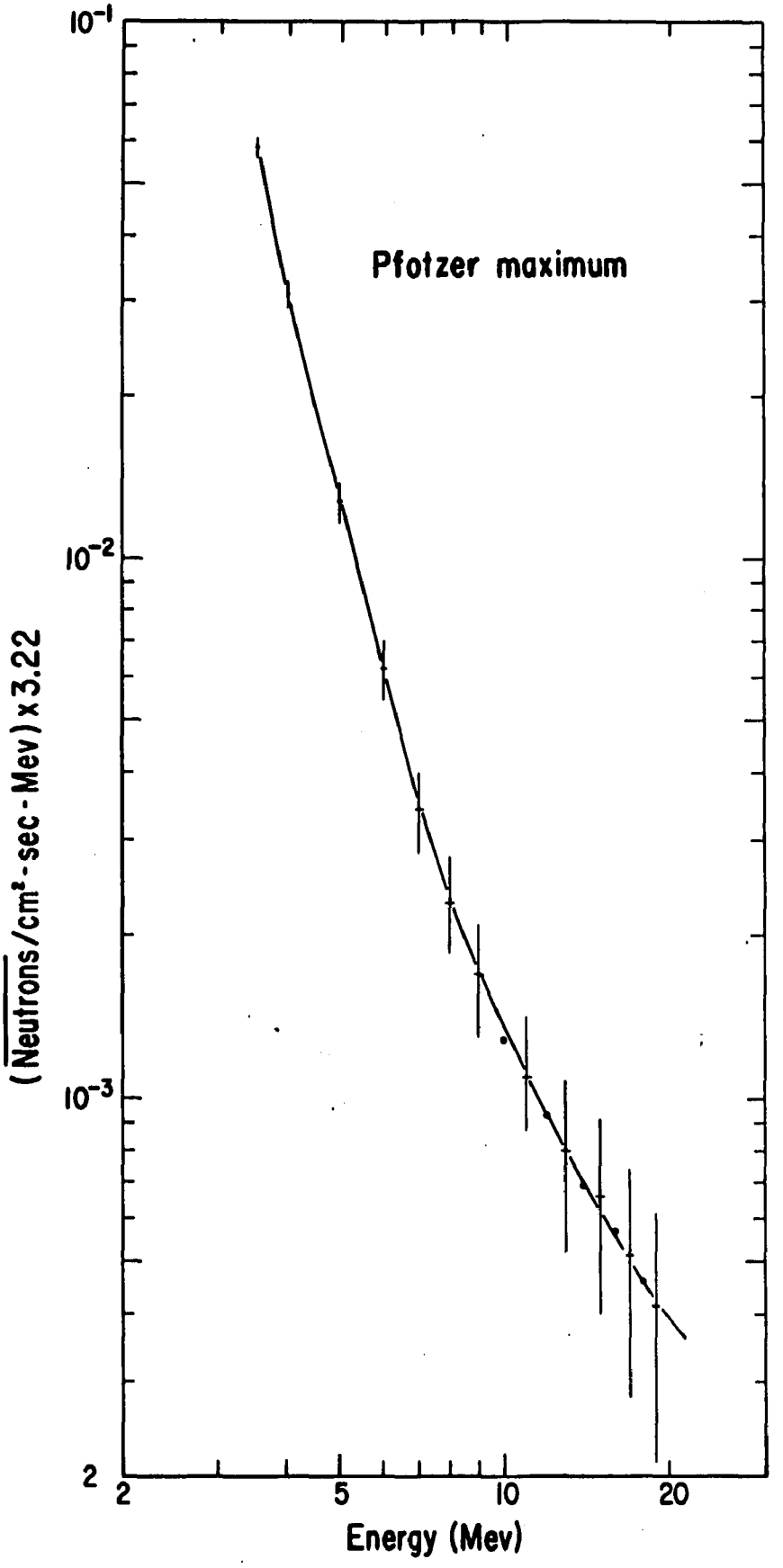
Pfotzer maximum
10^{-1}
10^{-2}
10^{-3}
2
2
5
10
20
Energy (Mev)
$(\overline{\text{Neutrons}}/\text{cm}^2\text{-sec-Mev}) \times 3.22$

Figure 29

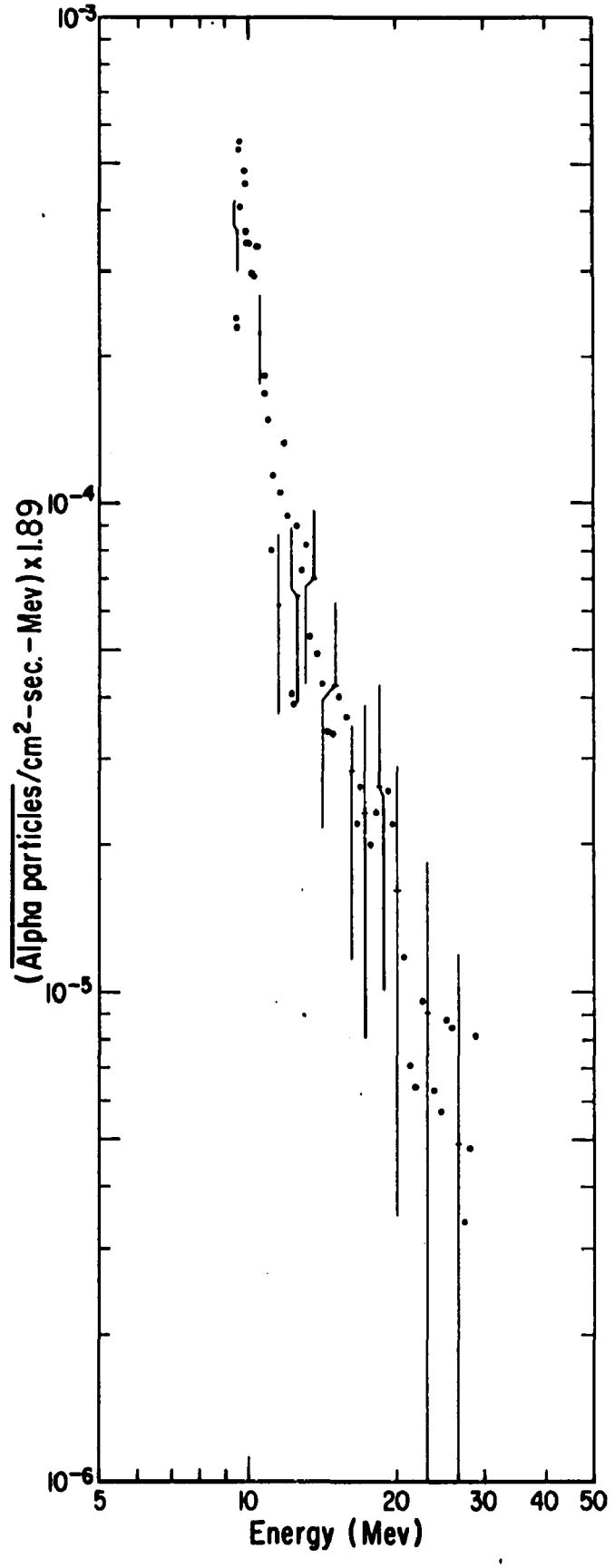
10^{-3}
10^{-4}
10^{-5}
10^{-6}
$\overline{(\text{Alpha particles}/\text{cm}^2\text{-sec.-Mev})} \times 1.89$
5
10
20
30
40
50
Energy (Mev)

Figure 30

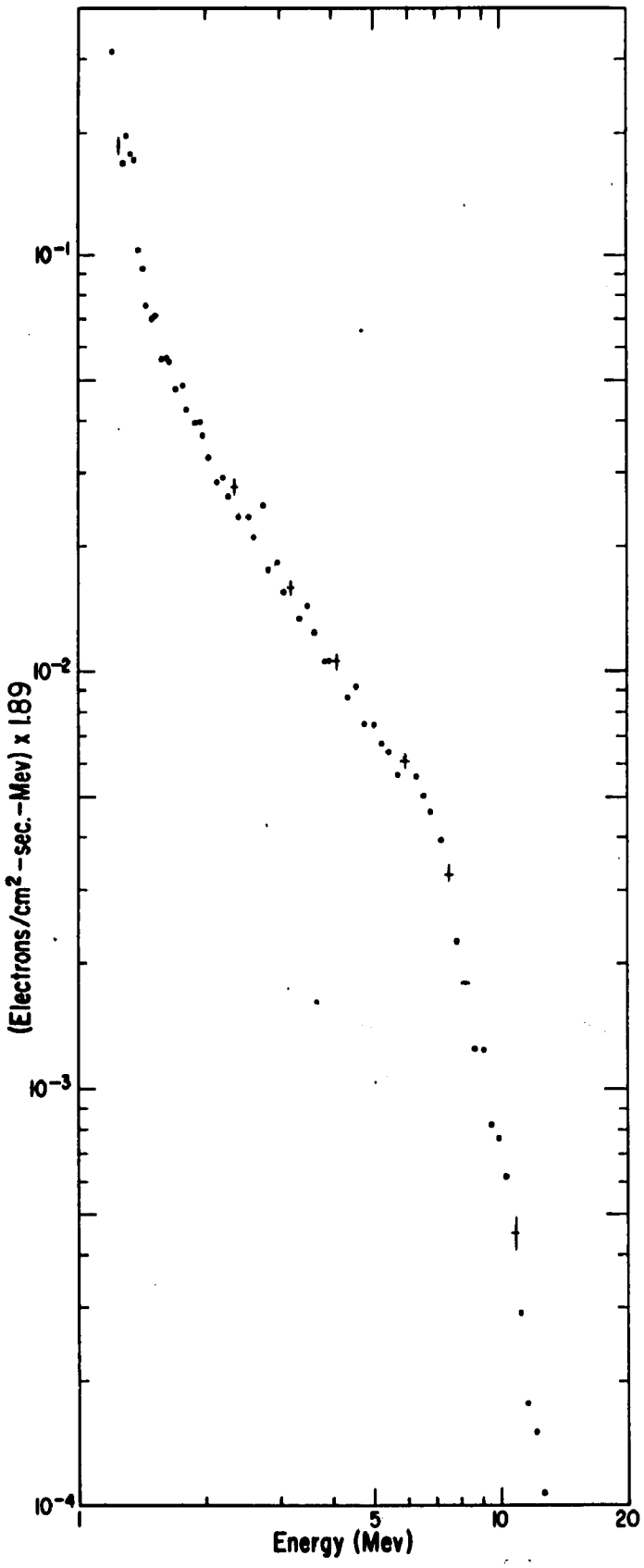

Figure 31a

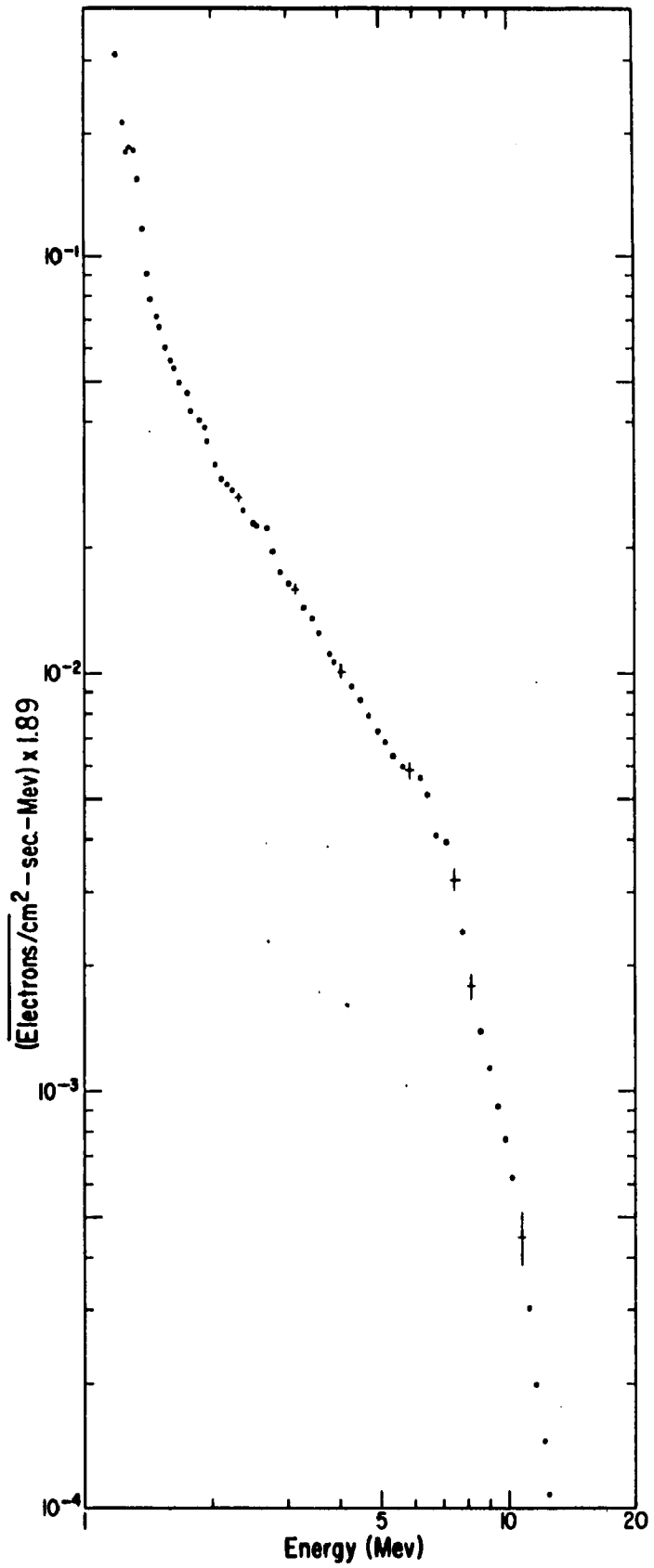
10^{-1}
10^{-2}
10^{-3}
10^{-4}
$\overline{(\text{Electrons/cm}^2\text{-sec-Mev})} \times 1.89$
1
5
10
20
Energy (Mev)

Figure 31b

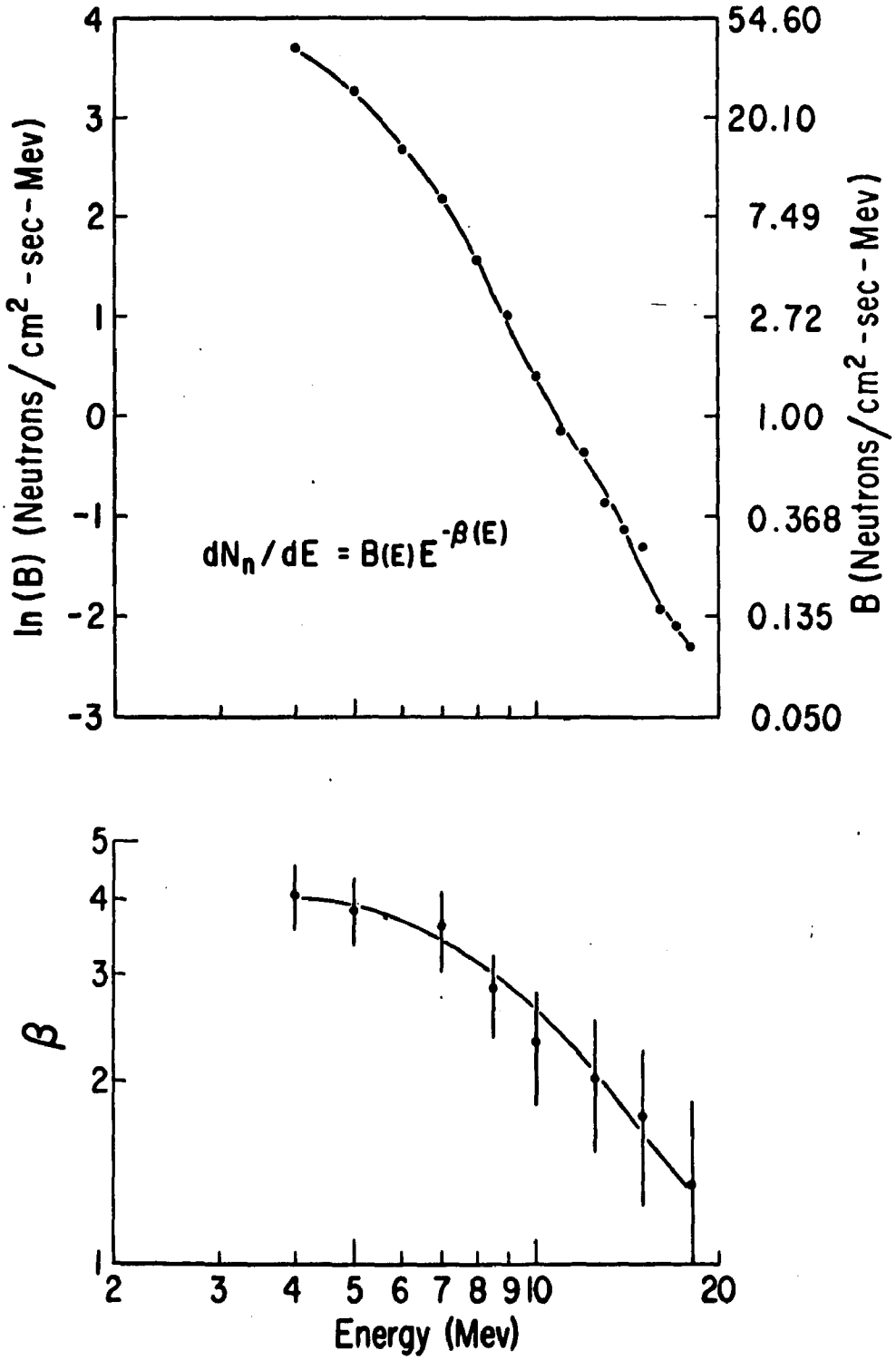
4
3
2
1
0
-1
-2
-3
54.60
20.10
7.49
2.72
1.00
0.368
0.135
0.050
ln (B) (Neutrons/cm² - sec - Mev)
B (Neutrons/cm² - sec - Mev)
dN_n / dE = B(E) E^-β(E)
β
5
4
3
2
1
2
3
4
5
6
7
8
9
10
20
Energy (Mev)

Figure 32

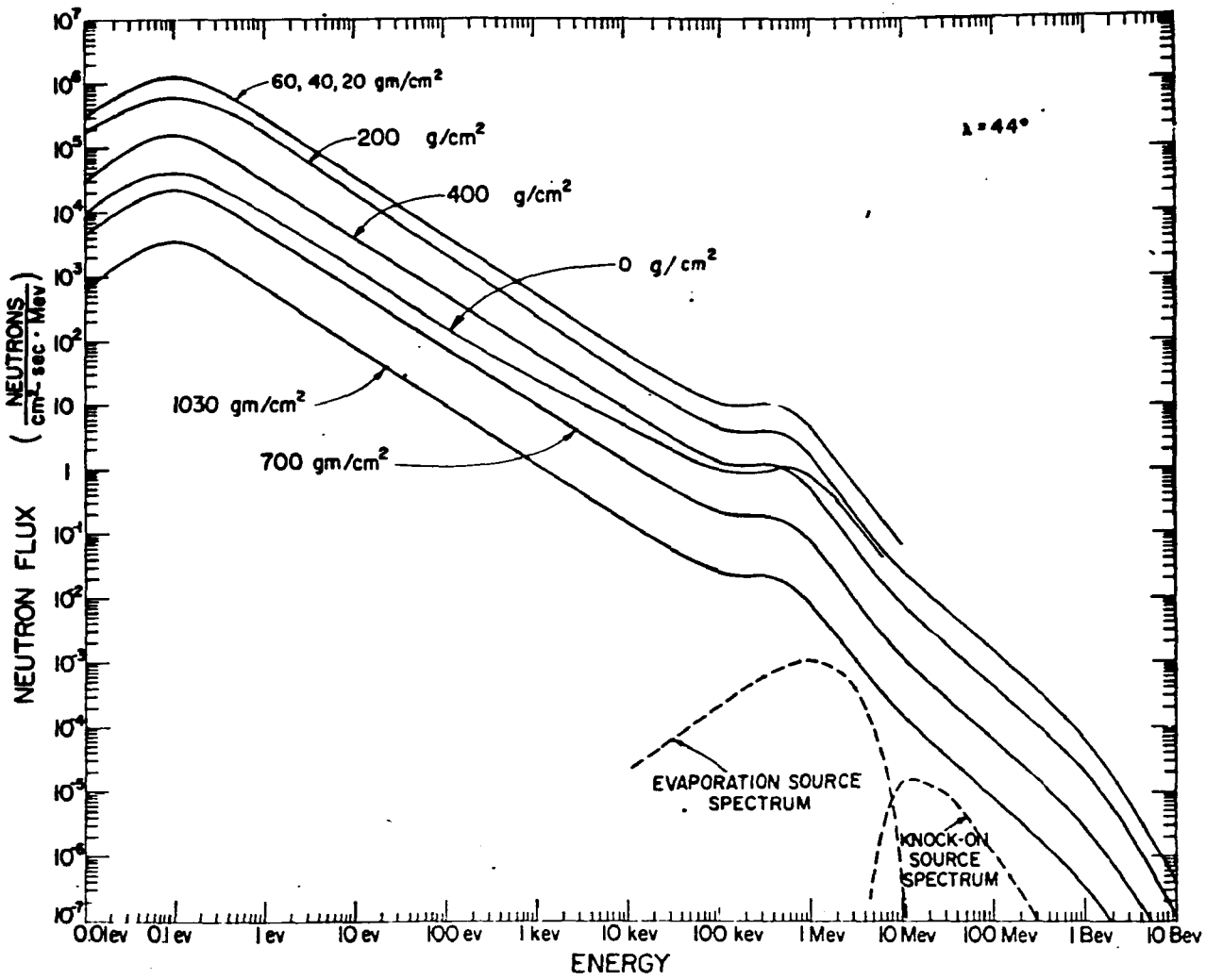
NEUTRON FLUX (NEUTRONS / cm² · sec · Mev)
ENERGY
60, 40, 20 gm/cm²
200 g/cm²
400 g/cm²
0 g/cm²
1030 gm/cm²
700 gm/cm²
λ = 44°
EVAPORATION SOURCE SPECTRUM
KNOCK-ON SOURCE SPECTRUM
0.01ev
0.1 ev
1 ev
10 ev
100 ev
1 kev
10 kev
100 kev
1 Mev
10 Mev
100 Mev
1 Bev
10 Bev

Figure 33

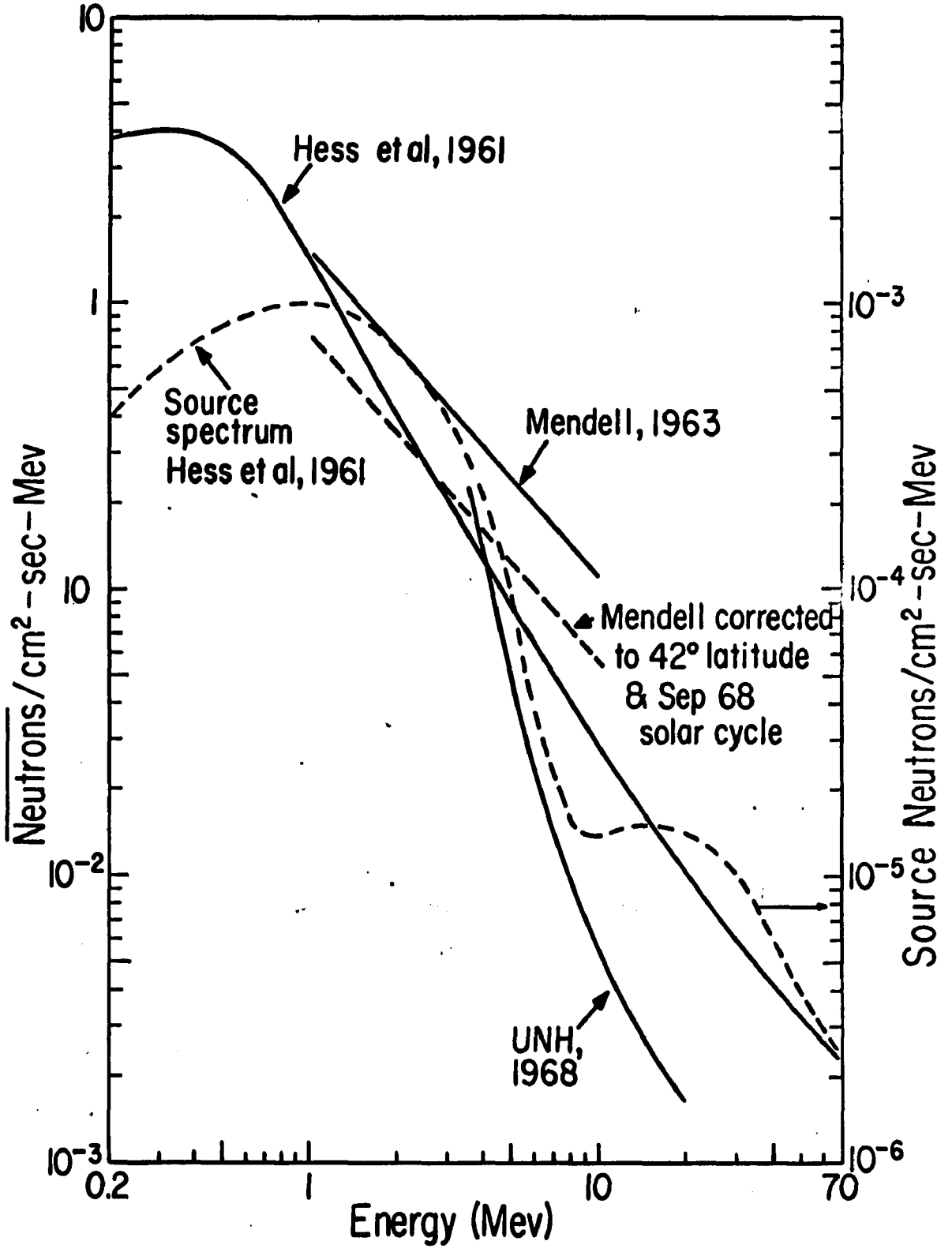
Hess et al, 1961
Source spectrum Hess et al, 1961
Mendell, 1963
Mendell corrected to 42° latitude & Sep 68 solar cycle
UNH, 1968
Neutrons/cm²-sec-Mev
Source Neutrons/cm²-sec-Mev
Energy (Mev)
10
1
10⁻²
10⁻³
10⁻³
10⁻⁴
10⁻⁵
10⁻⁶
0.2
1
10
70

Figure 34

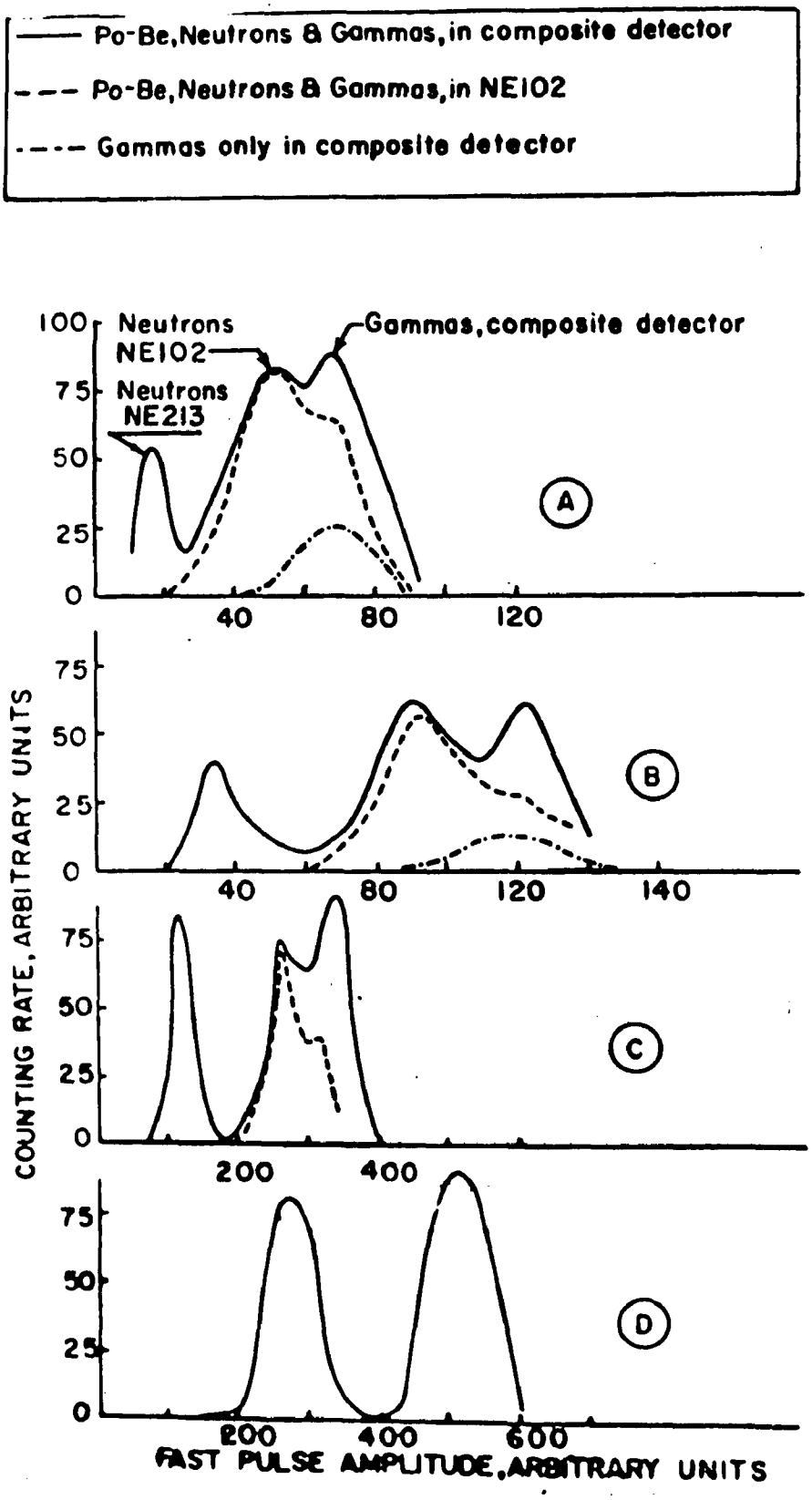
Po-Be, Neutrons & Gammas, in composite detector
Po-Be, Neutrons & Gammas, in NE102
Gammas only in composite detector
Neutrons NE102
Neutrons NE213
Gammas, composite detector
A
B
C
D
COUNTING RATE, ARBITRARY UNITS
FAST PULSE AMPLITUDE, ARBITRARY UNITS

Figure 35

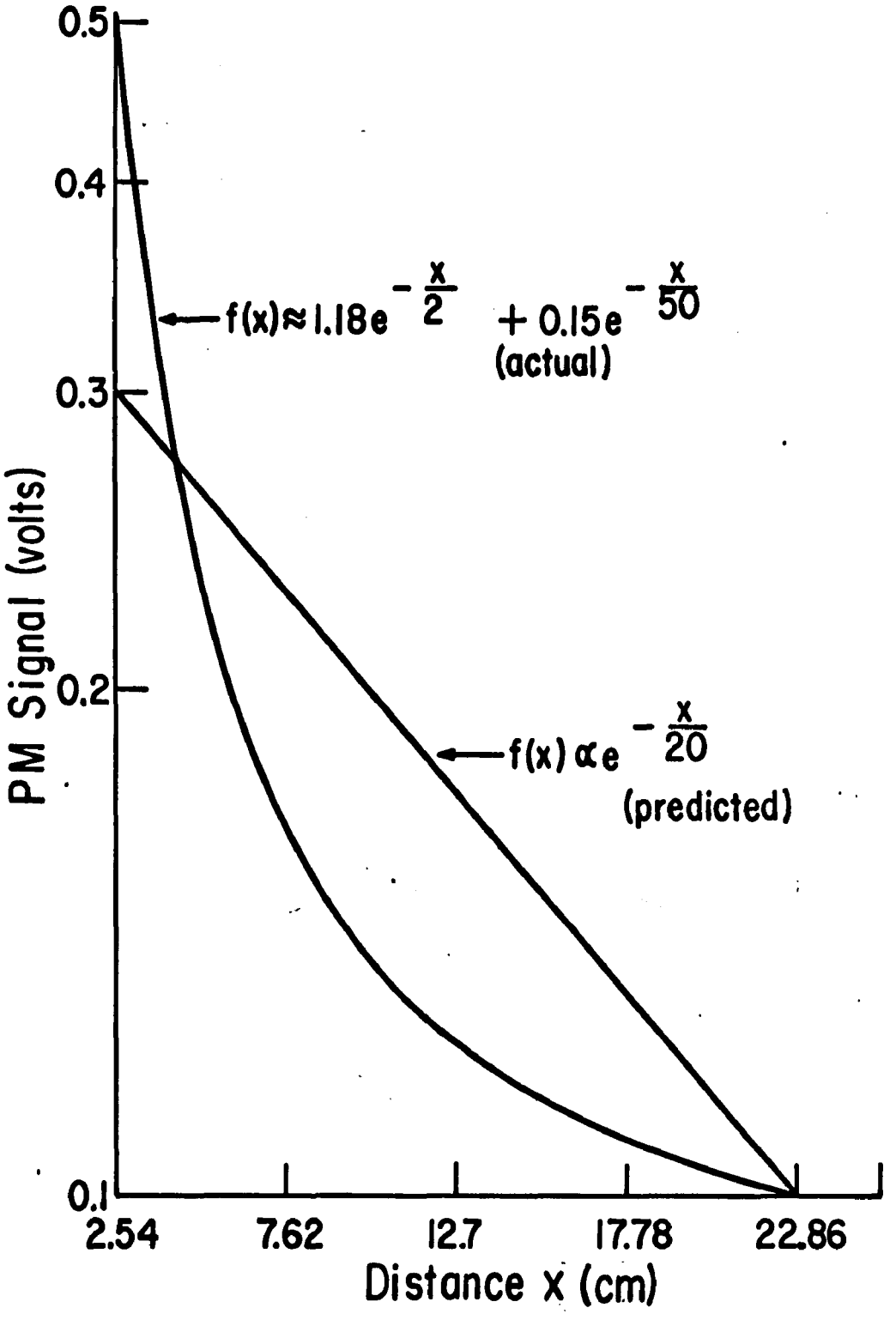
0.5
0.4
0.3
0.2
0.1
PM Signal (volts)
$f(x) \approx 1.18e^{-\frac{x}{2}} + 0.15e^{-\frac{x}{50}}$
(actual)
$f(x) \propto e^{-\frac{x}{20}}$
(predicted)
2.54
7.62
12.7
17.78
22.86
Distance X (cm)

Figure A-1

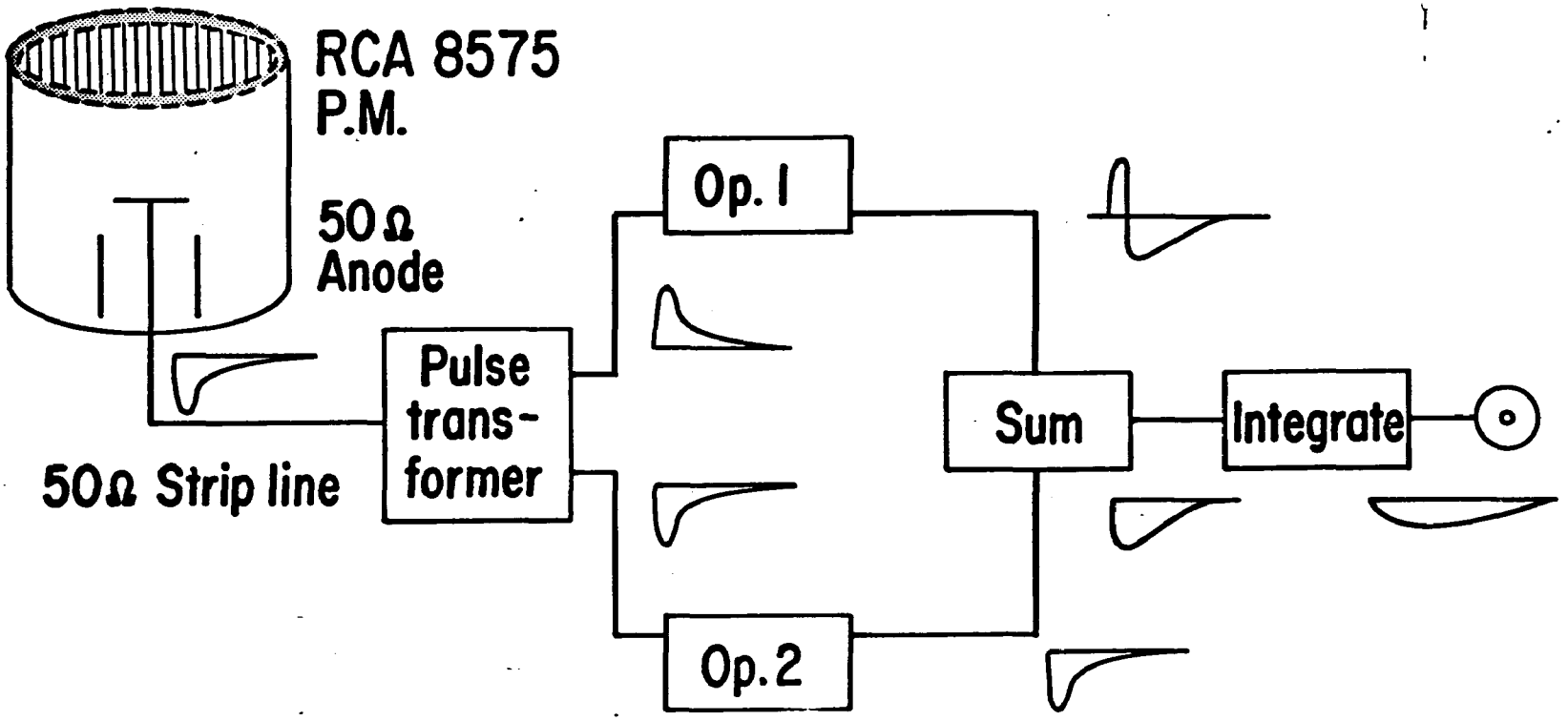
RCA 8575
P.M.
50 Ω
Anode
50Ω Strip line
Pulse
trans-
former
Op. 1
Op. 2
Sum
Integrate

Figure A-2

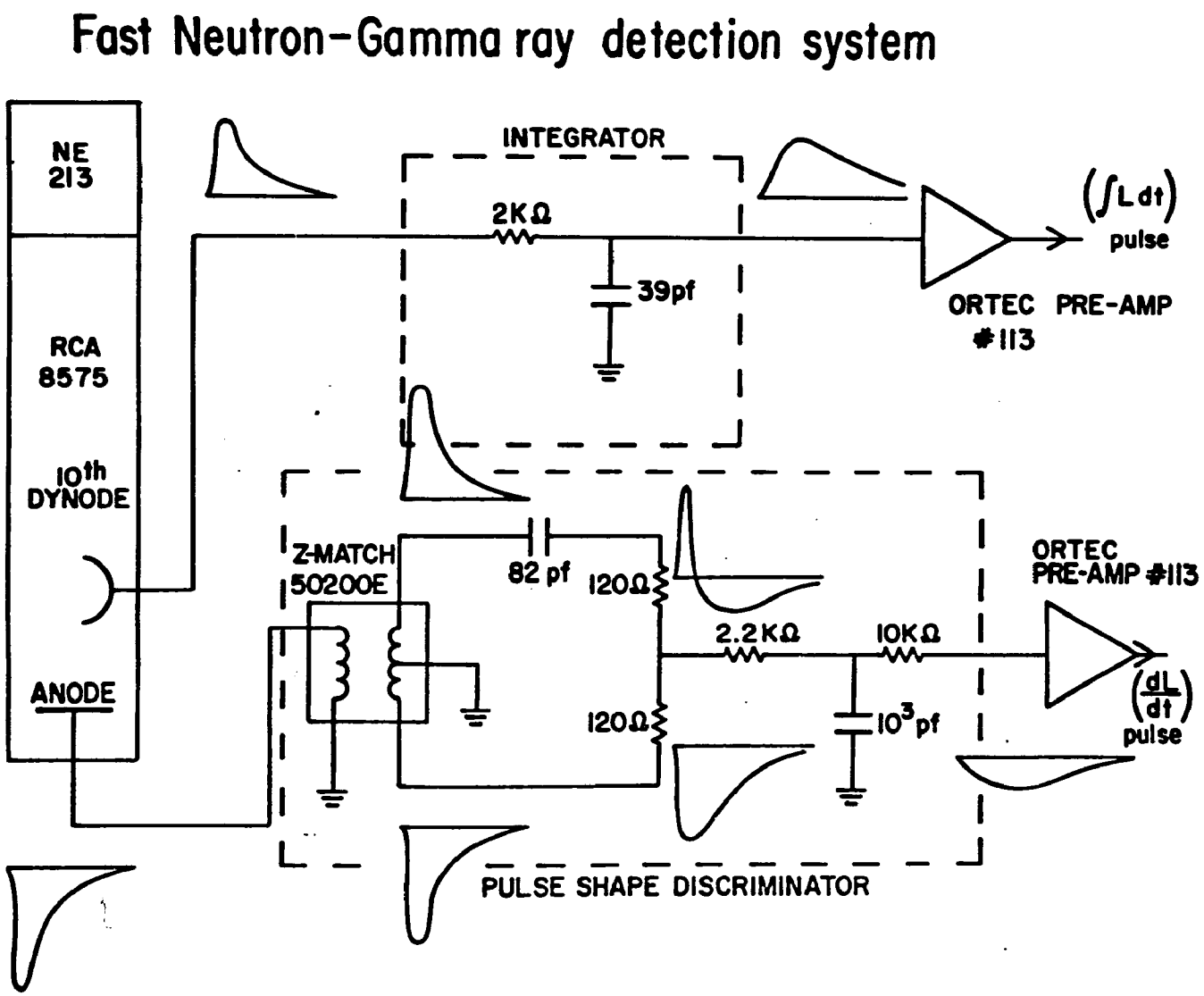
Fast Neutron-Gamma ray detection system
NE 213
RCA 8575
10th DYNODE
ANODE
INTEGRATOR
2KΩ
39pf
(∫L dt) pulse
ORTEC PRE-AMP #113
Z-MATCH 50200E
82 pf
120Ω
120Ω
2.2KΩ
10KΩ
10³pf
ORTEC PRE-AMP #113
(dL/dt) pulse
PULSE SHAPE DISCRIMINATOR

Figure A-3

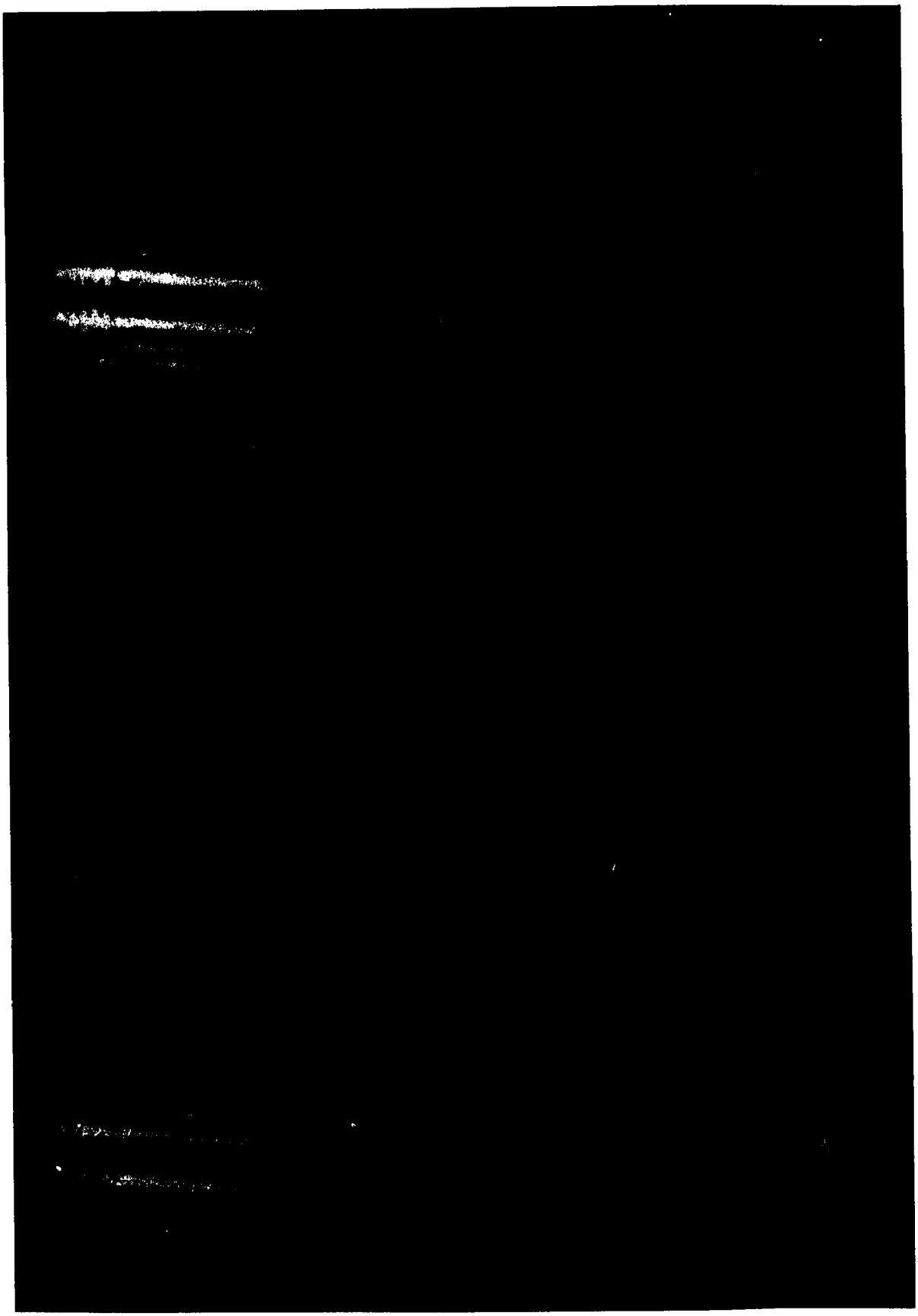

Figure A-4

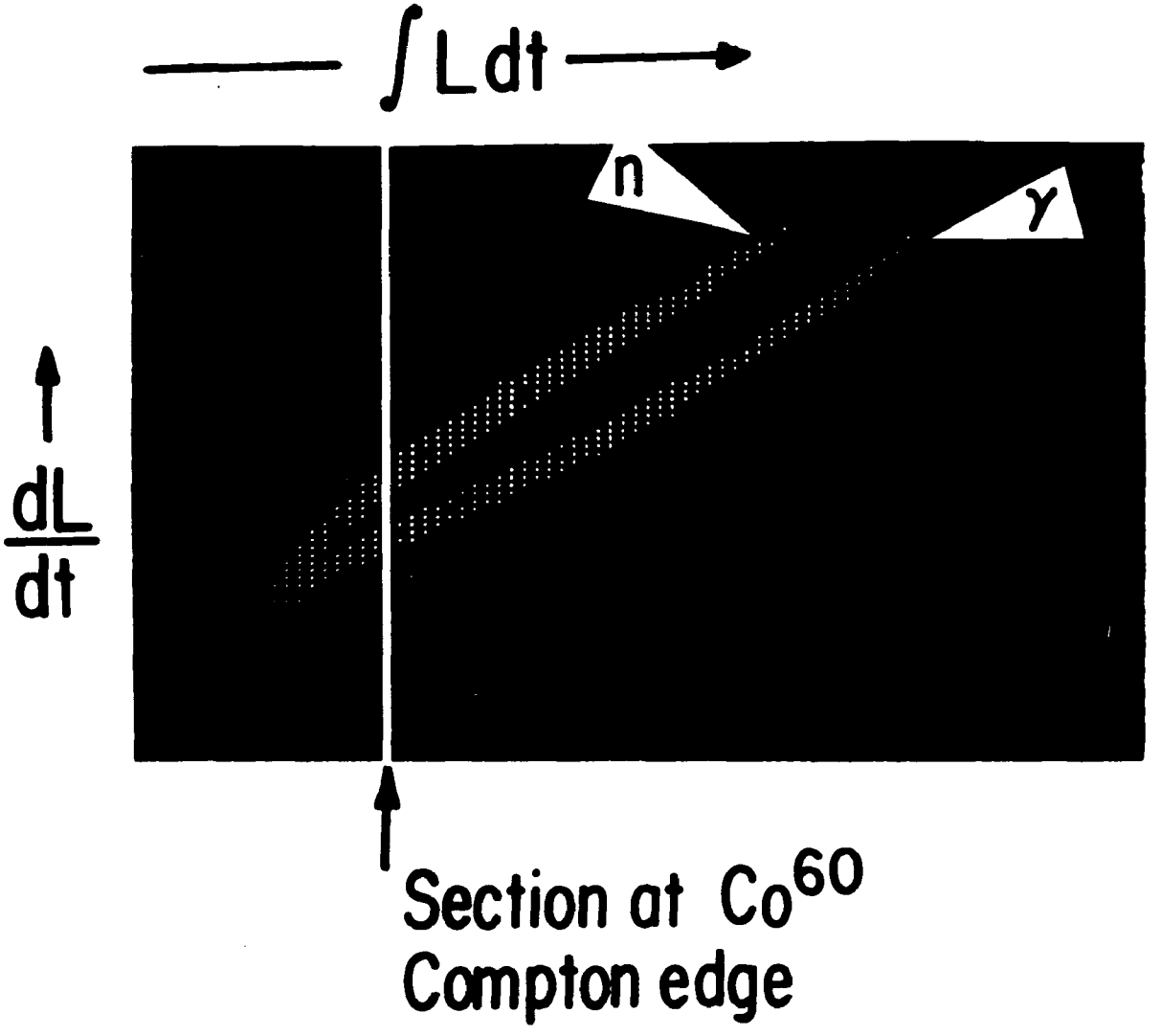

Figure A-5

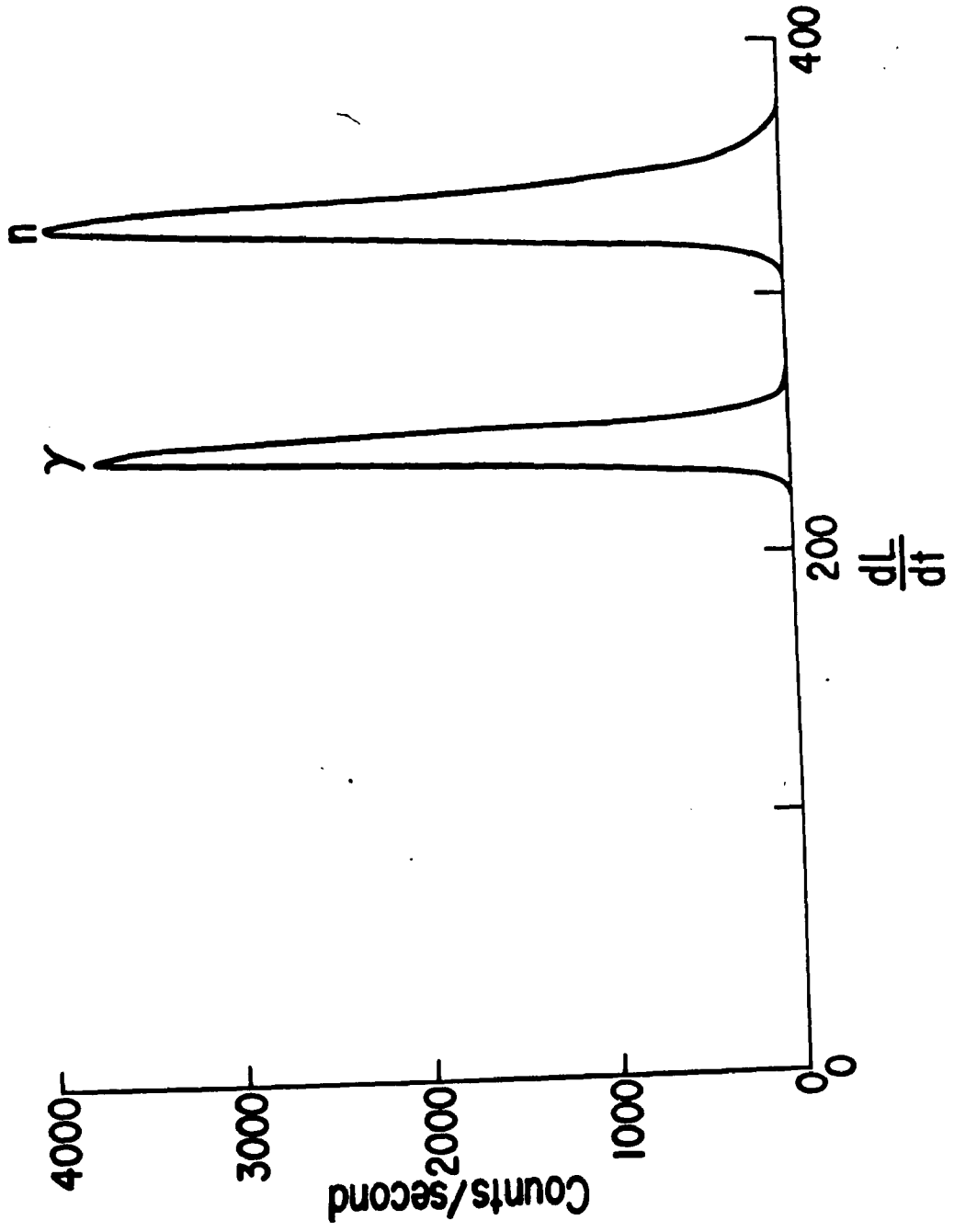

Figure A-6

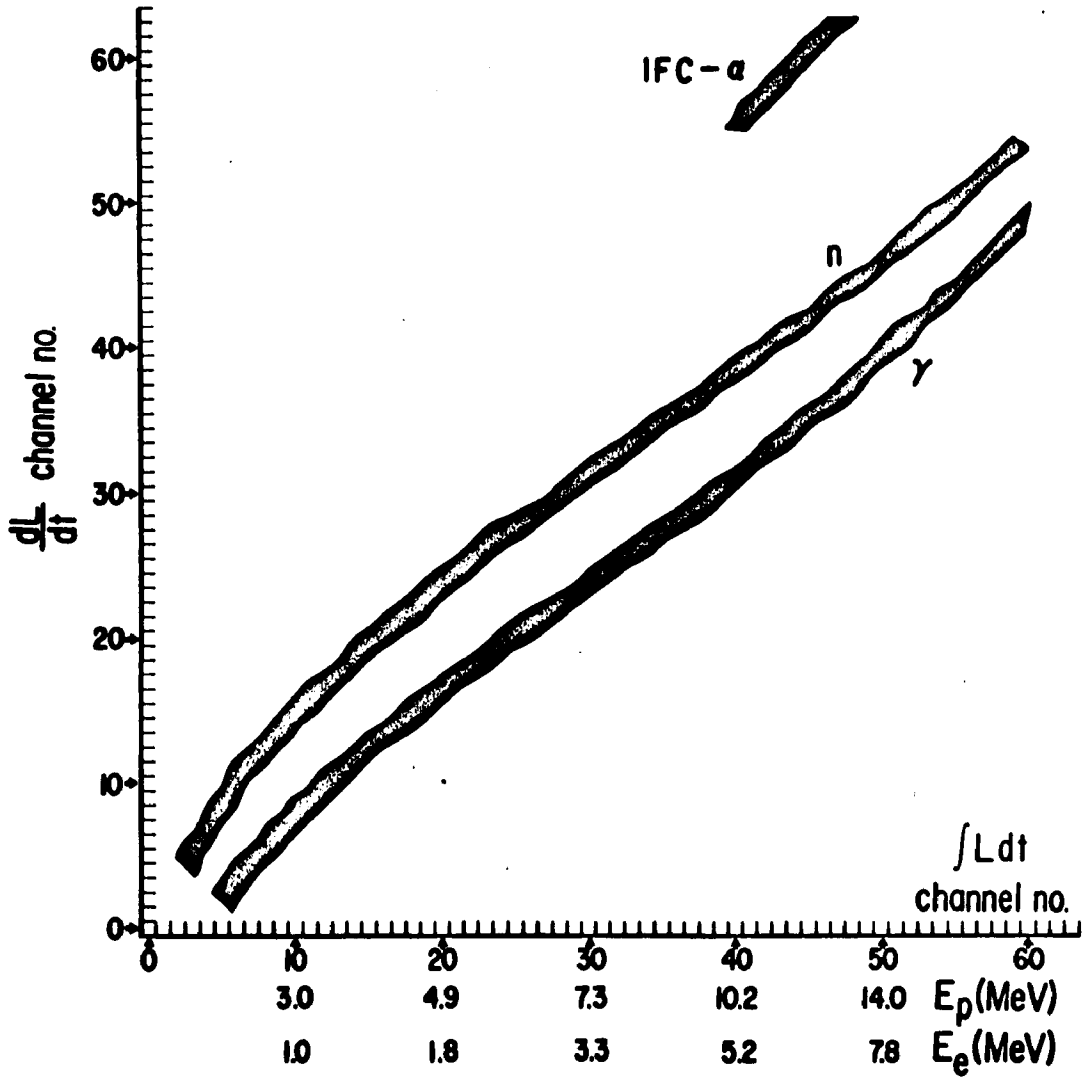
IFC-α
n
γ
dL/dt channel no.
∫Ldt channel no.
0
10
20
30
40
50
60
3.0
4.9
7.3
10.2
14.0
Ep(MeV)
1.0
1.8
3.3
5.2
7.8
Ee(MeV)

Figure A-7

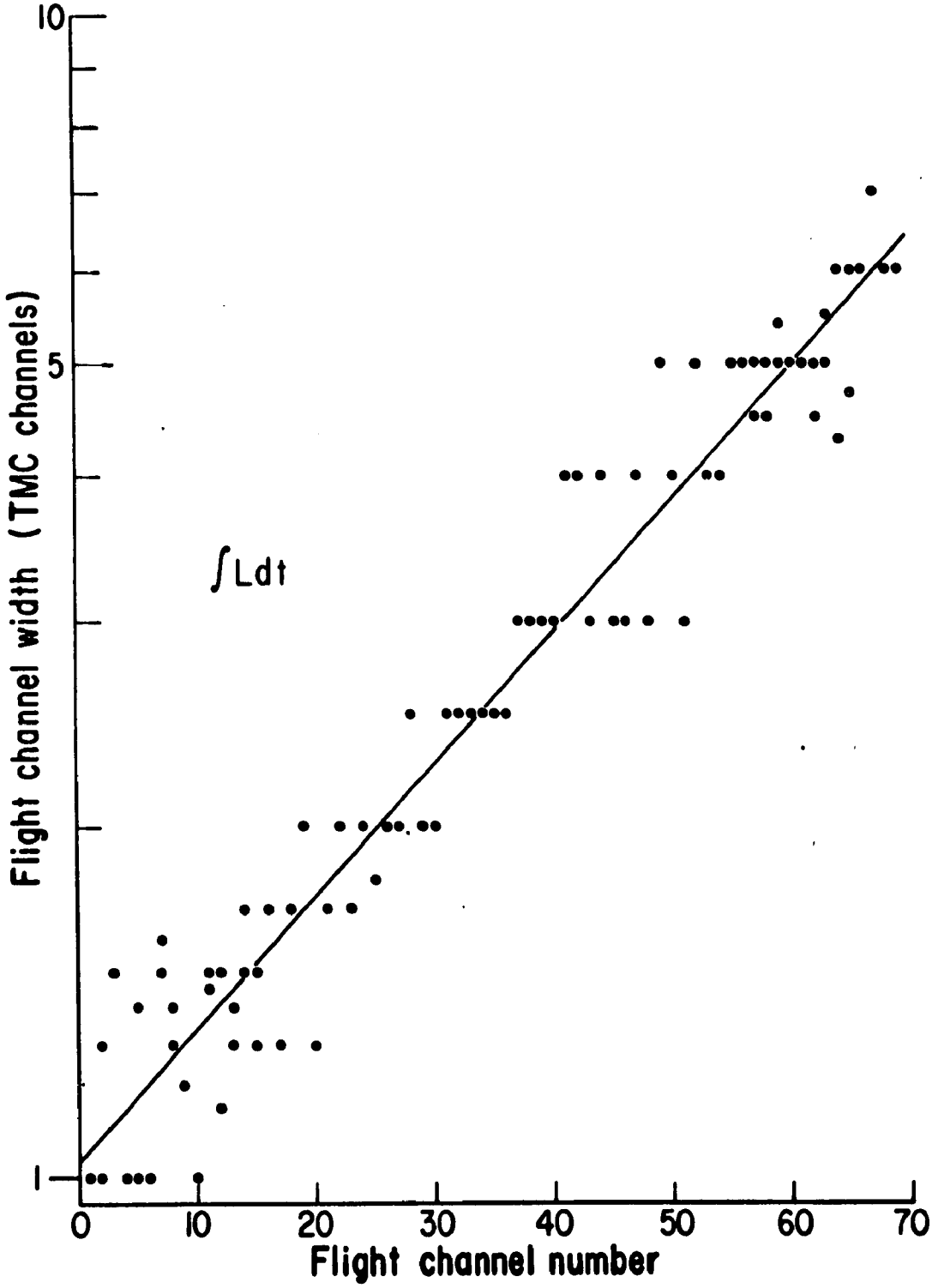
10
5
1
Flight channel width (TMC channels)
∫Ldt
0
10
20
30
40
50
60
70
Flight channel number

Figure A-8

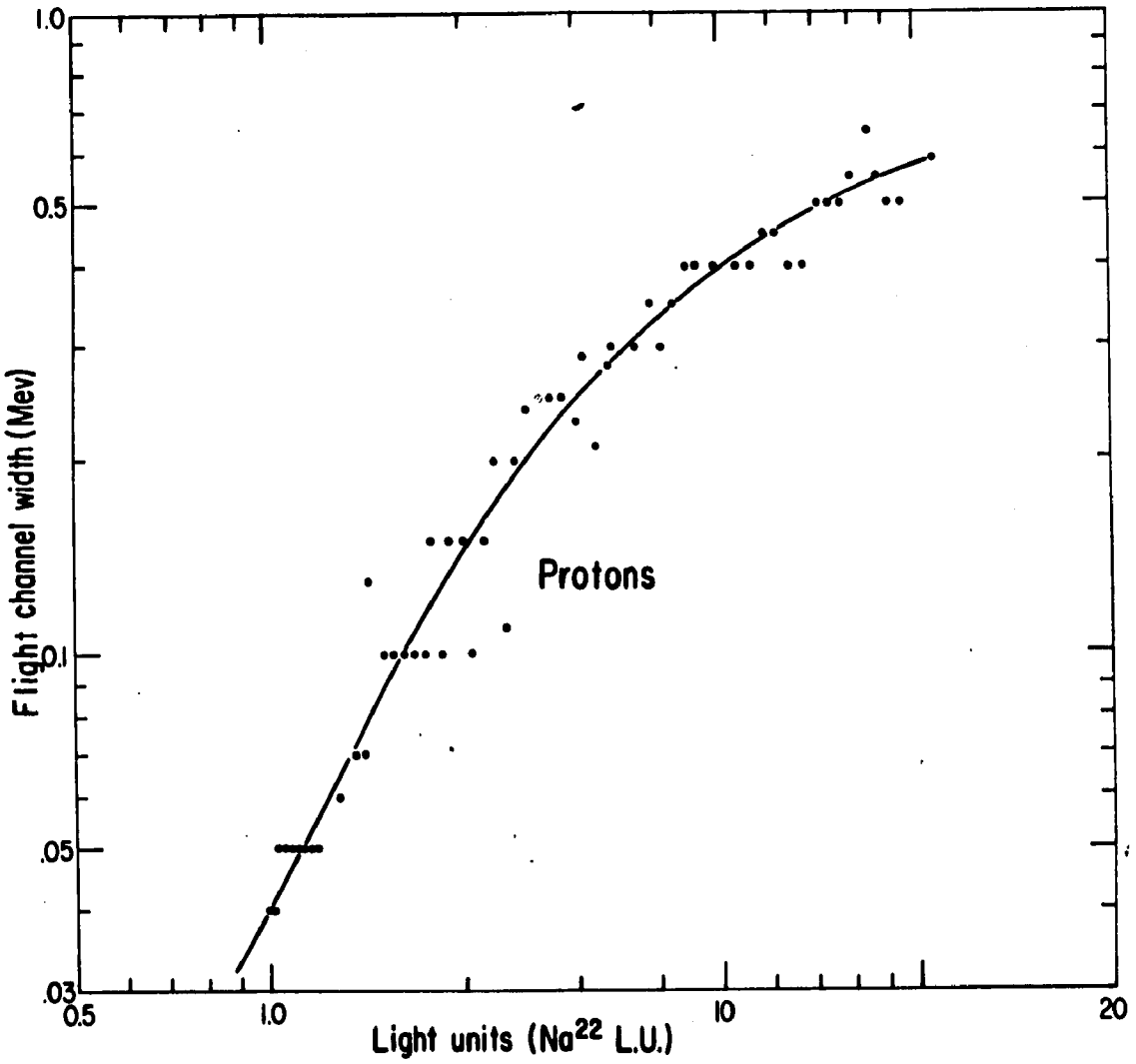
1.0
0.5
0.1
.05
.03
Flight channel width (Mev)
Protons
0.5
1.0
10
20
Light units (Na22 L.U.)

Figure A-9

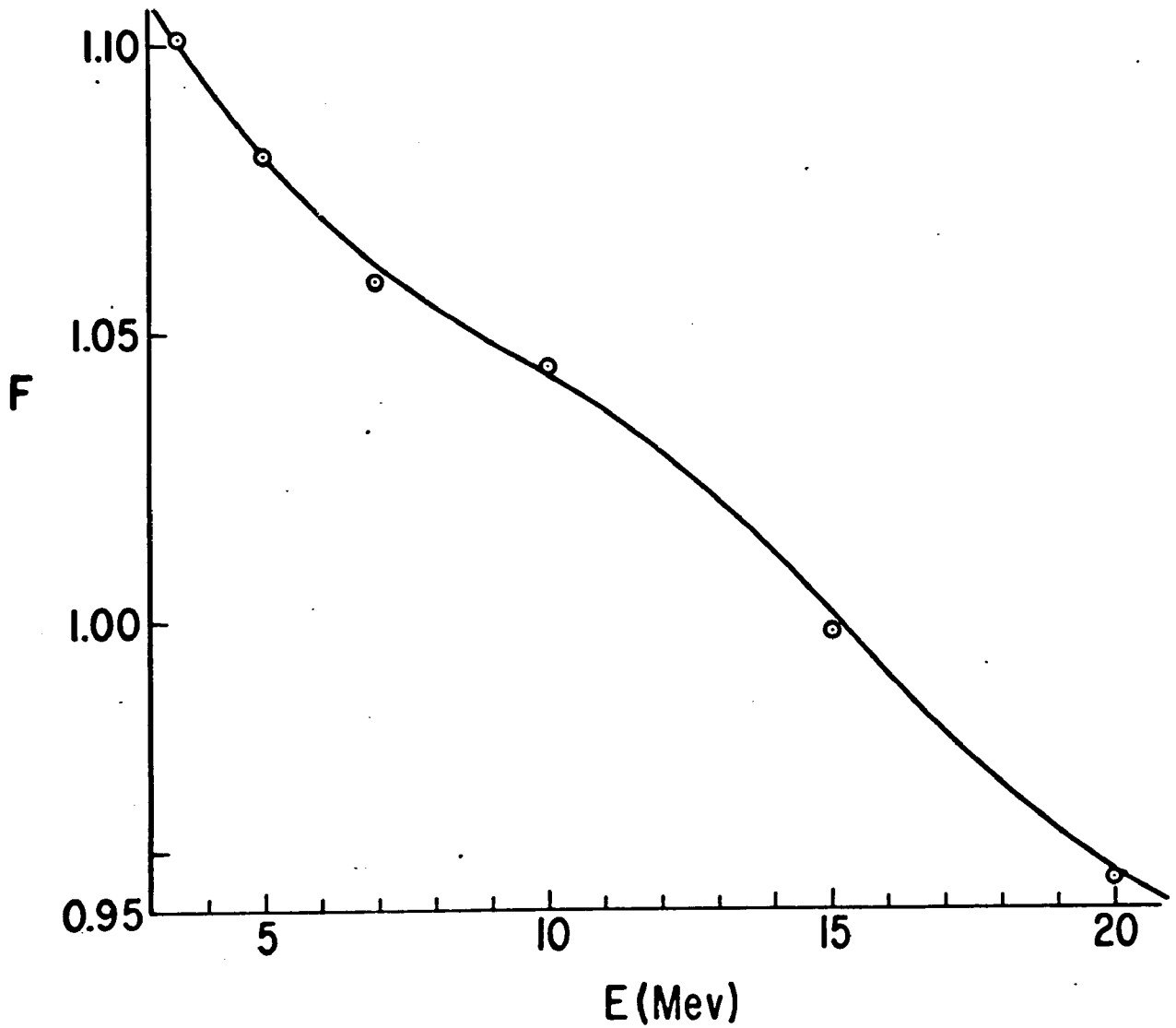

Figure A-10

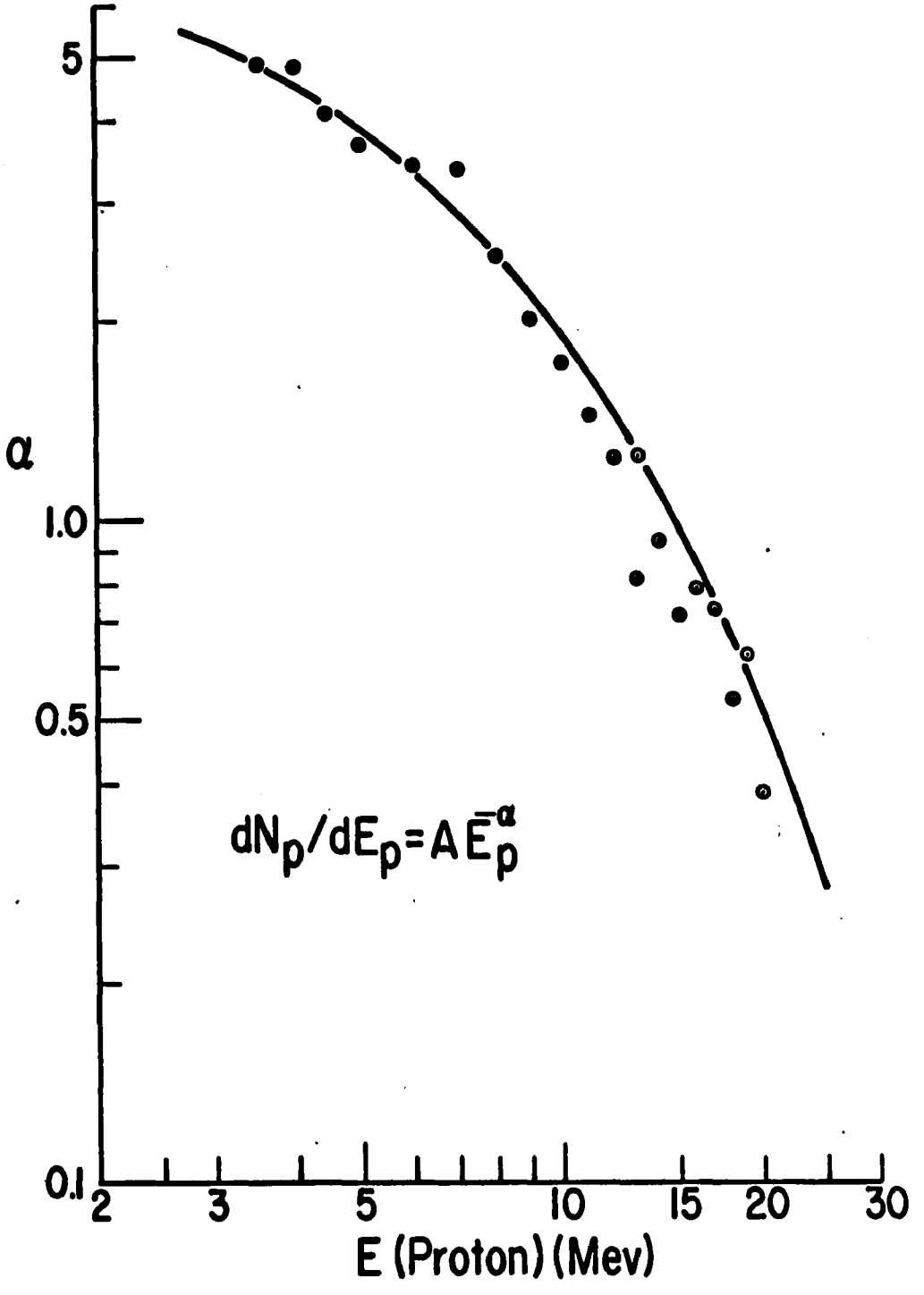

Figure A-11